Evidence of IR-Induced Chemistry in Neat Solid: Tautomerization of Thiotropolone by Thermal, Electronic and Vibrational Excitations

Journal:	*The Journal of Physical Chemistry*
Manuscript ID	jp-2021-04081f.R1
Manuscript Type:	Article
Date Submitted by the Author:	n/a
Complete List of Authors:	Pereira, Nelson; Universidade de Coimbra Faculdade de Ciencias e Tecnologia, Department of Chemistry Nunes, Cláudio; Universidade de Coimbra, Department of Chemistry Reva, Igor; Universidade de Coimbra, Department of Chemistry Fausto, Rui; Universidade de Coimbra, Chemistry

Evidence of IR-Induced Chemistry in Neat Solid: Tautomerization of Thiotropolone by Thermal, Electronic and Vibrational Excitations

Nelson A. M. Pereira, [1] Cláudio M. Nunes,[1]* Igor Reva,[1,2] and Rui Fausto[1]

[1]University of Coimbra, CQC, Department of Chemistry, 3004-535 Coimbra, Portugal

[2] University of Coimbra, CIEPQPF, Department of Chemical Engineering, 3030-790 Coimbra, Portugal

TOC Graphic

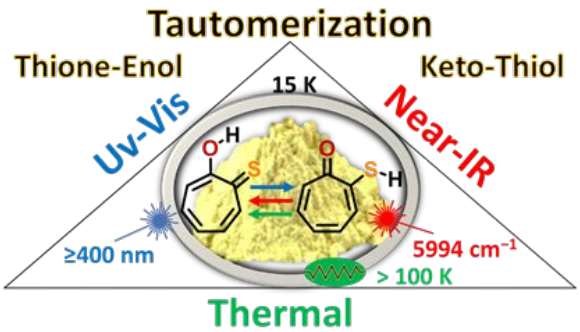

ABSTRACT: Thiotropolone isolated in argon and xenon matrices (as monomers) or in neat solid (as crystalline or amorphous state) at low temperature was found to exist only in the thione-enol form. Visible light irradiation ($\lambda \geq 400$ nm) leads to thione-enol→ thiol-keto tautomerization in matrices as well as in neat solid conditions at 15 K. The assignment of the IR spectra of the two thiotropolone tautomers (thione-enol and thiol-keto) was carried out with the support of B3LYP/6-311+G(2d,p) computations. The thiol-keto form generated in situ in neat solid was found to tautomerize back to the thione-enol upon annealing up to 100 K. Gaussian-4 (G4) computations estimate that such tautomerization process has an energy barrier of ~25 kJ mol^{-1}, which is consistent with the observations. Moreover, it was found that narrowband IR irradiation of the thiol-keto form in neat solid, at the frequency of its CH stretching overtones/combination modes, also induces tautomerization to the thione-enol form. Such result constitutes an important demonstration of vibrationally induced chemistry in neat solid conditions.

1. INTRODUCTION

Tautomerism has been a subject of intense research due to the key role it can play in advanced materials and in biochemical processes, such as enzymatic catalysis, nucleic acid chemistry and drug activity.[1–7] Tautomers are often designated as *chameleons* because of their ability to interconvert due to small changes in the chemical environment (*e.g.*, pH, solvent and temperature).[4–7] It is well-known that, in solution, tautomeric equilibria are affected by the polarity of the solvent as well as by specific solute-solvent interactions. In contrast to what happens for the liquid (either neat liquid or solution) and gaseous phases, where different tautomers can coexist, in solid phase usually only one tautomer is present, although exceptions are known.[8–10] Because the nature of the tautomer present in a given solid phase strongly affects its properties (both physical and chemical), considerable effort has been put in the proper identification and characterization of the tautomers which form the solid phases of a given compound, in particular in the case of pharmaceutically relevant materials.[10–13]

Low-temperature matrix isolation, associated with infrared spectroscopy, has been successfully used to identify tautomers and to elucidate tautomeric processes. Typically, a gas-phase equilibrium tautomeric population is frozen in a solidified noble gas cryogenic matrix, keeping the concentration of the solute low enough to guarantee that individual molecules are well-isolated. Intramolecular tautomerization processes can then be promoted (*e.g.*, by photoexcitation) and used to obtain detailed information about the tautomeric structures and properties, as well as about the tautomerization mechanisms. For example, the intramolecular amino-imino tautomerism in compounds such as 7-azaindole[14], adenine,[15,16] and cytosines[17,18] has been elucidated in detail using this approach. Also, many examples of keto-enol tautomerism, such as in isocytosine,[19] hypoxanthine,[20] and 2-pyridinones[21,22] have been investigated under matrix isolation conditions. This type of studies has also been expanded to sulfur-containing molecules, as the 2-pyridinethione,[23] as well as to many other molecules exhibiting thione-thiol tautomerism, *e.g.*, 6-thiopurine,[24] 2-thioquinoline,[25] 2-thioimidazoles,[26,27] thioacetamide[28,29] and thiourea.[30]

The tautomerization processes taking place under matrix isolation conditions have been triggered by electronic excitation. In a recent breakthrough, we have reported on a tautomerization process induced by vibrational excitation.[31] In that pioneer work, the thione-enol (**s-OH**) ↔ thiol-keto (**a-SH**) bidirectional tautomerization of thiotropolone (Scheme 1) was

achieved by selective near-IR irradiation at the frequencies of CH stretching overtones or combinations modes of the reactant tautomeric form involved in each of the tautomerization reactions (direct and reverse).

Scheme 1. Structures of the most relevant isomers of thiotropolone (TT)

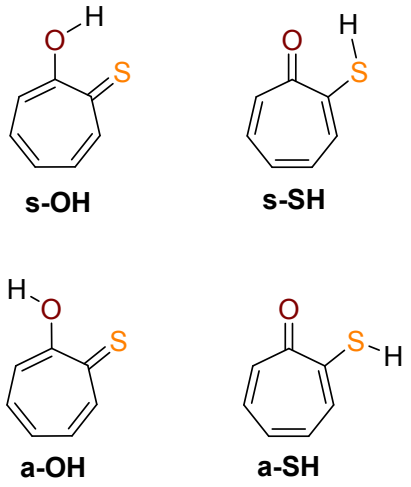

Since its renaissance in the beginning of the XXIth century, in result of the use of narrowband IR-light for photoexcitation instead of broadband IR-light, infrared vibrational excitation has emerged as an elegant, powerful tool to achieve exquisite control of molecular structure.[32] This experimental approach was first applied to the study of formic acid conformers,[33] but vibrational excitation has since then been applied to many different types of molecules.[34] The technique has in fact the unique advantage of being selective in relation to several features: it is selective regarding the excited chemical species (*e.g.*, a given conformer of a compound, even when various compounds with multiple conformers are simultaneously present in the sample), regarding the vibrational mode excited, and also in relation to a specific matrix trapping-site (among several possible) occupied by the molecules of the species to be excited (*e.g.*, a given conformer; meaning that a chosen fractional population of this conformer can be selectively excited).

Nevertheless, in contrast to conformational changes, the application of this research strategy to induce bond-breaking/bond-forming reactions such as that involving the tautomerization of thiotropolone mentioned above still remains scarcely explored.[31] In fact, only a few studies have been reported on the use of vibrational excitation to promote a bond-breaking

or bond-breaking/bond-forming reactions in gas-phase at low-pressure[35–43] and in solution[44–47] conditions. On the other hand, to the best of our knowledge, such type of vibrationally-induced chemistry has never been described for a neat solid compound. This fact prompted us to extend our investigations on the infrared-induced tautomerization of thiotropolone to the neat solid state.

Thiotropolone has not been investigated in much detail hitherto. Besides our study,[31] only a few additional investigations have been reported, most of them using theoretical approaches. Those studies have predicted the thione-enol tautomeric form of thiotropolone as being predominant in the gas-phase,[48] as well as in aqueous solution[48] and solid-state.[49] However, there is still a lack of experimental data. The most relevant previously reported experimental results refer to the compound in solution and in solid state, where Machiguchi *et al.* claimed that thiotropolone exists as two rapidly-equilibrating tautomeric (thione-enol and thiol-keto) structures.[50] On the other hand, in our matrix isolation study,[31] monomeric thiotropolone was found to exist in a cryogenic argon matrix only in its most stable thione-enol **s-OH** form, a result that is in agreement with the study of Fernandez-Ramos *et al.*,[51] where the possibility of existence of H-atom tunneling in the thione-enol **s-OH** tautomer to yield the thiol-keto **s-SH** form at low-temperature was ruled out.

In view of the existing data, it is clear that there is still a lot to learn about the tautomerism in thiotropolone. In this context, we decided to revisit thiotropolone monomeric forms isolated in an argon matrix (used in our previous study) but also in a less inert xenon matrix, as a first approach towards the study of the tautomerism of thiotropolone in the neat condensed phases (both crystalline and amorphous). As will be shown, we demonstrate the occurrence of visible-light induced thione-enol → thiol-keto tautomerization of thiotropolone in noble gas matrices and also in neat solid at low temperature (15 K). Moreover, we reveal the possibility of a thermally induced and, noteworthy, also vibrationally induced thiol-keto → thione-enol tautomerization for the neat solid compound at low temperature.

2. EXPERIMENTAL METHODS

2.1 Sample preparation and FTIR measurements

Thiotropolone (**TT**) was synthesized as described in our previous work.[31] A cryogenic system was used for the deposition and subsequent handling of the **TT** samples. This system

comprehends a CsI window used as optical substrate, which is maintained at low temperatures using a closed-cycle helium refrigerator (APD Cryogenics, with a DE-202A expander). The temperature is measured directly at the sample holder, by a silicon diode sensor connected to a digital controller (Scientific Instruments, Model 9650-1), and stabilized with accuracy of 0.1 K. **TT** placed in a glass tube connected *via* a stainless-steel needle valve (SS4 BMRG valve, NUPRO) to the vacuum chamber of the cryostat (~10^{-6} mbar) was sublimated at room temperature and deposited as a neat amorphous solid onto the CsI window (~15 K). Crystallization of the neat solid **TT** was carried out by heating the sample up to 200 K. The annealing process was monitored by recording infrared spectra at different temperatures. After the polycrystalline form was obtained, the sample was cooled back to 15 K and the experiments were performed with the polycrystalline solid. Monomeric matrices of **TT** were obtained by co-deposition of the sample with a large excess of argon (N60, Air Liquide) or xenon (N48, Air Liquide) onto the CsI window (15 or 20 K). Infrared spectra were recorded using a Thermo Nicolet 6700 Fourier-transform infrared (FTIR) spectrometer, purged through the optical path with dry, CO_2-filtered air to avoid interference of atmospheric H_2O and CO_2. A deuterated triglycine sulfate (DTGS) detector and a KBr beam splitter were used to collect the spectra with 0.5 cm^{-1} resolution in the mid-IR region (4000–400 cm^{-1}). An indium gallium arsenide (InGaAs) detector and a CaF_2 beam splitter were used to collect the spectra with 2.0 cm^{-1} resolution in the near-IR region (7500–4000 cm^{-1}).

A KBr pellet of **TT** was prepared by standard procedures. A mixture of solids of **TT** and KBr was ground into a fine powder with an agate mortar and pestle, and then an appropriate portion was compressed in a hydraulic press (Specac, 15 TON) to obtain the pellets. The corresponding mid-IR spectrum was collected at room temperature using the above-described FTIR spectrometer, with 2 cm^{-1} spectral resolution.

2.2 Irradiation experiments

Irradiation experiments in the visible region were carried out using broadband UV-Vis light (200 W) produced by a Hg(Xe) lamp (Newport, Oriel Instruments) in conjugation with a UV cut-off filter which is not transparent for wavelengths below 400 nm. For **TT** isolated in an argon matrix, irradiation experiments in the visible region were also performed (with similar results) using narrowband light at 420 nm (20 mW) generated by the signal beam of an optical

parametric oscillator (OPO, Spectra Physics Quanta-Ray MOPO-SL) pumped by a pulsed Nd:YAG laser (duration: 10 ns; repetition rate: 10 Hz). Irradiation experiments in the near-IR region were performed using frequency-tunable narrowband light (~0.2 cm^{-1} spectral width; 100 mW) generated by the idler beam of the same OPO-laser system.

2.3 Theoretical computations

The quantum chemical calculations were performed with the Gaussian 16 software package.[52] Geometry optimizations were carried at the DFT level of theory using the B3LYP[53–55] functional in conjugation with the 6-311+G(2d,p)[56] basis set. The harmonic vibrational frequencies were calculated at the same level of theory. All calculations were carried out using the very tight optimization criteria and the superfine integration grid. The nature of the stationary points on the potential energy surfaces was confirmed through the analysis of the corresponding Hessian matrices. The computed harmonic frequencies were scaled by a factor of 0.979.[57] The resulting scaled frequencies and respective infrared intensities were used to simulate the IR spectra by convoluting each peak with a Lorentzian function having a full width at half-maximum (FWHM) equal to 2 cm^{-1}. The integral band intensities correspond to the calculated infrared absolute intensities and are presented in the arbitrary units of "Relative Intensity". The molecular vibrations of **TT**, computed at the B3LYP/6-311+G(2d,p) level within the harmonic approximation, were subjected to the VMARD (Vibrational Mode Automatic Relevance Determination) analysis, using Bayesian regression.[58] Anharmonic vibrational wavenumbers and IR intensities for transitions up to two quanta, including the fundamental modes, first overtones and combination modes, were also computed.[34] The fully automated second-order vibrational perturbative approach (GVPT2) of Barone and coworkers was used for this purpose.[59,60] Vertical excitation energies of **TT** were calculated at the B3LYP/6-311+G(2d,p) level using the time-dependent density functional theory.[61–63] For the simulation of the UV-Vis spectra, the calculated peaks were convoluted with a Lorentzian function having a half-width at half-maximum (HWHM) equal to 0.124 eV (1000 cm^{-1}). The Gaussian-4 composite method (G4),[64] known to calculate thermodynamic quantities with high accuracy, was employed to compute the energies of the most relevant isomers of **TT**, as well as the energies of the corresponding rotamerization and tautomerization transition states.

2.4 Tunneling and Arrhenius activation energy computations

Tunneling computations were performed on the theoretical B3LYP/6-311+G(2d,p) computed potential energy profiles, along the intrinsic reaction coordinate (IRC) and calculated in non-mass-weighted Cartesian coordinates, expressed in units of Bohr.[65] The transmission coefficients of the H-atom tunneling through a parabolic barrier were calculated using the Wentzel−Kramers−Brillouin (WKB) approximation.[66–68] Accordingly, the probability *P(E)* of tunneling is given by equation (1):[69]

$$P(E) = e^{-\pi^2 w\sqrt{2m(V_0 - E)}/h} \qquad (1)$$

where a particle with mass m tunnels through a barrier with height V_0 and width w, (V_0–E) is the energy deficiency of the particle with respect to the top of the barrier, and h is the Planck's constant. For the SH-rotamerization reaction of **a-SH** to **s-SH**, the probability of tunneling (transmission coefficient) equal to 4.0×10^{-25} was estimated, using a calculated barrier height of 31.7 kJ mol^{-1} and width at the ZPE level of 5.39 Bohr (equivalent of 2.85 Å, see Figure S9). The tunneling rate is the product of the transmission coefficient and the frequency of attempts. If the light H-atom of the thiol group of **a-SH** is vibrating at a τ(SH) torsional frequency of about 405 cm^{-1} (B3LYP/6-311+G(2d,p) computed value), this results in a tunneling rate of 4.9×10^{-12} s^{-1}, *i.e.* a half-life time of 1.4×10^{11} s (approx. 4500 years). For the H-shift tautomerization reaction of **s-SH** to **s-OH**, a tunneling rate of 1.2×10^{10} s^{-1}, *i.e.* a half-life time of ~1×10^{-11} s was estimated in ref. [31].

The Barnes empirical correlation between the barrier height for conformational isomerization and the temperature at which that transformation is observed upon annealing,[70] can be computed using the Arrhenius equation (2)

$$k = Ae^{\frac{-E_a}{RT}} \qquad (2)$$

where k is the rate constant, A is the pre-exponential factor, R is the universal gas constant and T is the absolute temperature. It is assumed that a pre-exponential factor A is equal to $10^{11.2}$ and a first-order reaction rate constant k is between an upper (too slow) and lower (too fast) limit half-life time of 10^4 and 10^2 s (corresponding to $k = 6.93 \times 10^{-5}$ and 6.93×10^{-3} s^{-1}, respectively).[70,71] Since, upon annealing at 60 K no tautomerization of **a-SH** to **s-OH** was observed (which is dictated by the SH-rotamerization step, as discussed in the text), it can be assume that $k < 6.93 \times 10^{-5}$. In this way, an $E_a > 17.6$ kJ mol^{-1} is obtained.

3. RESULTS AND DISCUSSION

3.1 Vibrational characterization of thiotropolone and tautomerization induced by electronic excitation

Thiotropolone (**TT**) monomers isolated in an argon matrix (15 K), upon sublimation of the sample at room temperature, were found to exist only in the thione-enol **s-OH** form.[31] The corresponding experimental IR spectrum compares well with the B3LYP/6-311+G(2d,p) computed spectrum of the **s-OH** form (Figure 1a,b). **TT** isolated in a xenon (20 K) matrix was also found to exist only in the **s-OH** form (Figure S1). The results are consistent with the gas-phase equilibrium population estimated for **TT** at room temperature (>96% of **s-OH**),[31] and the expected trapping of that population after the deposition of the sample mixed with noble gas onto the cold CsI window.[72]

TT was subsequently investigated in neat solid conditions. The IR spectrum of the sample deposited in the absence of matrix gas, onto the CsI optical substrate at 15 K, indicates the formation of an amorphous solid (Figure 1c). The observed broad and rounded IR bands are characteristic features typically exhibited by the amorphous materials.[73–76] The amorphous solid **TT** was then annealed until a polycrystalline solid was formed. The crystallization process was observed to take place in the temperature range between 170 and 190 K. At this stage, considerable changes in the profile of the IR bands took place, as they became significantly sharp and narrow (Figure S2). Upon subsequent cooling down to 15 K, the IR spectrum maintains the same features of that collected at 190 K, indicating that the same crystalline arrangement is preserved during the cooling process (Figure 1d). An identical IR spectrum of **TT** is obtained when the sample is deposited directly onto the CsI window at 190 K or from a solid sample at room temperature (Figure S3).

As mentioned before, Machiguchi *et al.* claimed that neat solid **TT** (crystalline) is constituted by two tautomers co-existing in a fast equilibrium (thione-enol **OH** ↔ thiol-keto **SH**), independently of the temperature (studies were carried out between 79 and 333 K).[50] However, the data presented here for **TT** in the neat solid state under different conditions and temperatures do not confirm the presence in the samples of the higher energy thiol-keto **SH** tautomer. Apart from the differences observed in the width of the IR bands, the samples of **TT** as a crystalline solid, as an amorphous solid, or isolated in noble gas matrices as monomers, exhibit

similar spectral patterns, which are doubtlessly ascribable to the thione-enol **s-OH** form existing in these three different experimental conditions (Figure 1). Bellow, the detailed analysis of the IR spectrum of the **s-OH** form will be addressed. Moreover, it will be demonstrated that a thiol-keto **SH** tautomer is produced upon visible-light irradiation of the neat solid **TT** (or the matrix-isolated **TT**) under low-temperature conditions (Scheme 2). This thiol-keto **SH** tautomer does not exist in any of the pristine samples of neat solid **TT** (or of matrix-isolated **TT**) and does not persist above 100 K (*i.e.*, the temperatures at which most of the experiments reported by Machiguchi *et al.* were conducted).

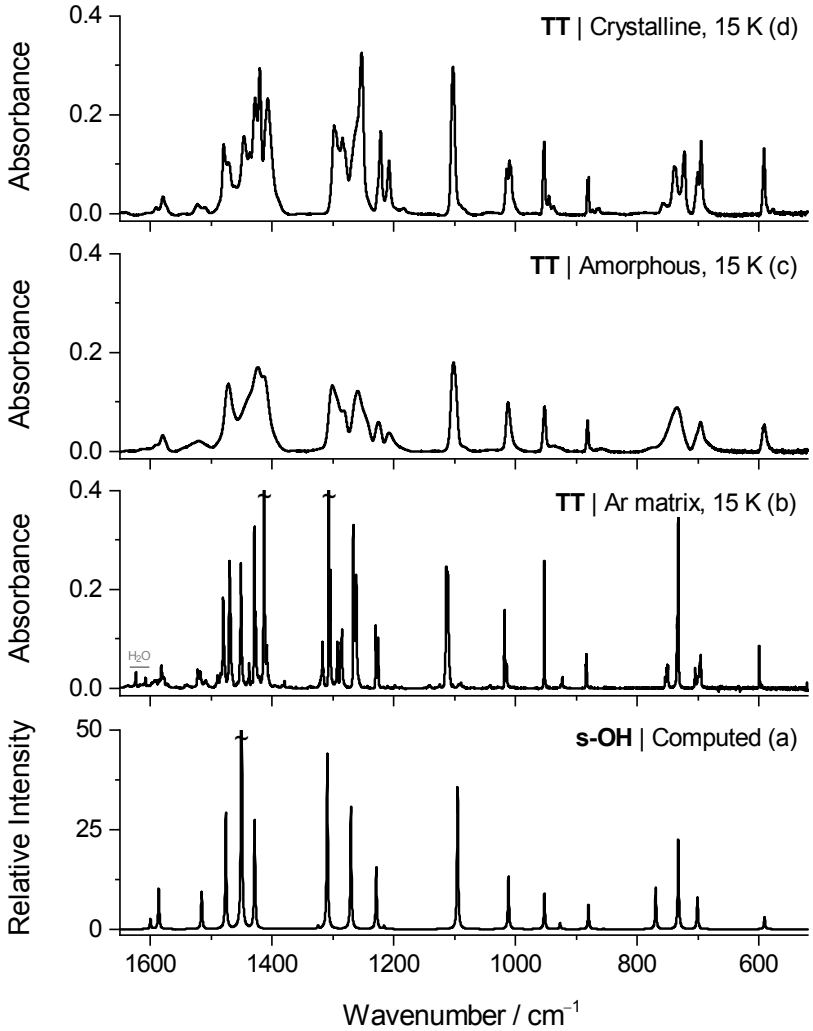

Figure 1. (a) B3LYP/6-311+G(2d,p) computed IR spectrum of the **s-OH** form of thiotropolone (**TT**). (b-d) Experimental IR spectra of **TT**: (b) monomeric compound deposited in an argon matrix at 15 K; (c) neat compound deposited at 15 K (amorphous solid); (d) neat compound deposited at 15 K, annealed up to 190 K, and cooled again to 15 K (crystalline solid). Bands designated with tilde (~) are truncated.

Scheme 2. Transformation of matrix isolated or neat solid s-OH into a-SH induced by electronic excitation with visible light[a]

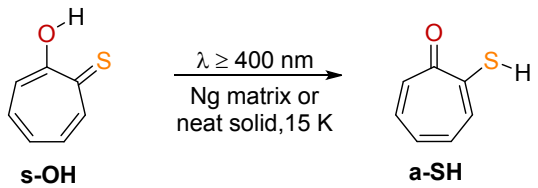

[a]"Ng" stands for noble gas.

The electronic excitation of **TT** in noble gas matrices and in neat solid (amorphous and crystalline) was performed using visible light with λ ≥ 400 nm. The excitation wavelengths in the visible domain were chosen based on the simulated electronic spectra computed at B3LYP level of theory, which indicate that the thione-enol **OH** tautomer does absorb above 400 nm but the thiol-keto **SH** tautomer does not (Figure S4 and Table S1).

As mentioned above, the irradiation in the visible range (λ ≥ 400 nm) of the **s-OH** form of thiotropolone deposited in an argon matrix at 15 K was found to produce a new tautomer, identified as the thiol-keto **a-SH** (Figures 2a,b and S5-S7). Although the computed IR spectra of **a-SH** and **s-SH** are very similar, a detailed analysis points to the exclusive formation of **a-SH**. This is also supported by the fact that **s-SH** is predicted to be a fleeting species not isolable even under cryogenic conditions (its half-life time is estimated to be on the picoseconds scale; see also ref. 31).[77] The detailed vibrational assignments of the two tautomers (initial and final forms) in argon matrix are described in detail in the Supporting Information (SI) and provided in Tables S2-S7. Three spectral regions are particularly suitable for spectral identification and discrimination of the thione-enol **s-OH** and thiol-keto **a-SH** tautomers: (i) immediately below and above 1550 cm^{-1}; (ii) between 800 and 720 cm^{-1}; and (iii) between 600 and 550 cm^{-1}:

(i) The most intense IR absorption of the **s-OH** form corresponds to a group of bands in the 1550–1400 cm^{-1} range (1522, 1480, 1470, 1451, 1429 and 1413 cm^{-1}). These bands are ascribed to four fundamental modes (ν_9, ν_{10}, ν_{11}, ν_{12}), which correspond to the ν(C=C) stretching, δ(CH) in-plane bending and the δ(COH) bending vibrations coupled in different fashions, and also to combination modes (as analyzed in detail in the SI; Table S3). On the other hand, two relatively weak IR absorptions appear above 1550 cm^{-1} (~1600 and 1582 cm^{-1}), which are ascribed to two fundamental ν(C=C) stretching modes (ν_7, ν_8) that are not

coupled with the δ(COH) coordinate. Upon thione-enol → thiol-keto tautomerization, there is a dramatic redistribution of spectral intensity around 1550 cm^{-1} (both above and below), which results from the fact that **TT** acquires a carbonyl C=O group, which is a dipole strongly absorbing in infrared. Indeed, the most intense IR absorptions of the **a-SH** form appear as a multiplet band between 1605 and 1585 cm^{-1}, ascribed to the fundamental mode (ν_8) that has a major contribution from the ν(C=O) stretching (Table S6). A higher frequency absorption appearing at 1628 cm^{-1} is ascribed to a vibrational mode (ν_7) with major ν(C=C) stretching contribution, coupled to the ν(C=O) stretching.

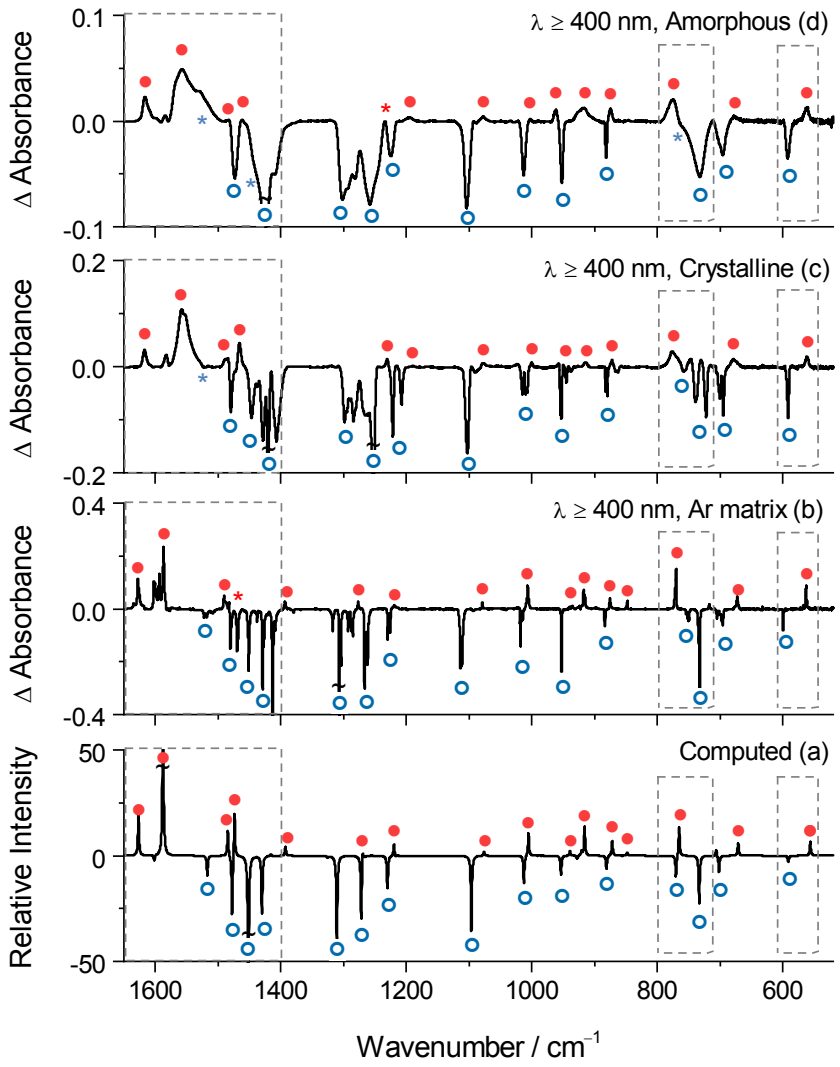

Figure 2. (a) Computed IR difference spectrum based on B3LYP/6-311+G(2d,p) vibrational data considering the transformation of **s-OH** into **a-SH** (ratio 1:1). Experimental IR difference spectra after irradiation of **TT** at 15 K: (b) in an argon matrix (λ = 420 nm, 20 mW, 2 min); (c) as

crystalline solid (λ ≥ 400 nm, 250 W, 1 h); (d) as amorphous solid (λ ≥ 400 nm, 250 W, 1 h). Bands marked with empty (○) and filled (●) circles are assigned to consumed **s-OH** and produced **a-SH**, respectively. The asterisks (∗) and tilde (~) indicate overlapped and truncated bands, respectively.

(ii) The most intense infrared band due to γ(CH) out-of-plane vibration appears at 735/733 cm^{-1}, for **s-OH** (ν_{33}), and at 770 cm^{-1}, for **a-SH** (ν_{32}), *i.e.* the bands due to the two forms are separated by 35–37 cm^{-1}. The frequencies and couplings of the γ(CH) vibrations reflect the difference in the geometry of their nearest groups, which correspond to the OCCS fragment with an H atom located on the oxygen atom for **s-OH** and on the sulphur atom for **a-SH**. One additional band at 751 cm^{-1} also appears for the **s-OH** form, which is due to the τ(OH) mode (ν_{32}).

(iii) An IR absorption with significant contribution from the ν(C–S) mode is observed as a narrow band at 563.5 cm^{-1} for **a-SH** (ν_{23}), whereas an IR absorption corresponding essentially to a ring deformation mode is observed at 599.8 cm^{-1} for **s-OH** (ν_{23}). Noteworthy, for **s-OH** a characteristic strong IR band appears at 1114 cm^{-1} due to the ν(C=S) mode coupled with vibrations of the ring (ν_{18}). Thiones are known to have a characteristic ν(C=S) stretching in this region, *e.g.* as reported for the thione cyclic molecules 2-thiouracil (1148 cm^{-1}), 2(1*H*)-pyrimidinethione (1144 cm^{-1}), and cyclohexa-2,4-diene-1-thione (1136 cm^{-1}).[23,78,79]

The irradiation (λ ≥ 400 nm) of thiotropolone in neat solid phases (amorphous and crystalline) at 15 K was also found to produce a new tautomeric form. The IR spectrum of the new tautomeric form **a-SH** produced by irradiation of the crystalline **s-OH** shows narrower bands than produced by irradiation of the amorphous **s-OH**. This suggests that the formation of **a-SH** occurs maintaining the crystalline or the amorphous state of the precursor **s-OH**. Several examples are known of photochemical reactions, including tautomerizations and conformational changes, which occur preserving the crystalline solid state.[9,80–83] The experimental difference IR spectra obtained (Figure 2c,d) have good correspondence with the spectral changes observed for the **s-OH** → **a-SH** tautomerization in similar experiments carried out in argon matrix (Figure 2b) or resulting from the B3LYP/6-311+(2d,p) computations (Figure 2a). The three IR spectral regions described above remain particularly discriminative for such identification (additional data are also provided in Tables S3 and S6):

(i) A group of bands in the 1550–1400 cm^{-1} range is observed for the neat solid **s-OH** (1522, 1479, 1471, 1447, 1428/1421 and 1408 cm^{-1}, for the crystalline solid; 1521, 1471, 1423, and 1413 cm^{-1}, for the amorphous solid), which correlates well with the monomer bands previously ascribed to ν(C=C) stretching, δ(CH) in-plane bending, δ(COH) bending vibrations, and some combination modes. The most intense IR absorptions of the neat solid **a-SH** appear at 1617 and 1558 cm^{-1} (for both crystalline and amorphous solids), in agreement with monomer bands ascribed to ν(C=O) and ν(C=C) stretching modes.

(ii) An absorption is observed for crystalline and amorphous solids, respectively at 738/723 and 734 cm^{-1}, for **s-OH**, and at 776 and 775 cm^{-1}, for **a-SH**, in good correlation with the corresponding monomer absorption ascribed to the strongest γ(CH) out-of-plane vibration.

(iii) One IR band is observed at 562 cm^{-1}, for **a-SH**, and at 592 cm^{-1}, for **s-OH**, for the crystalline and amorphous solids, which compares well with the corresponding monomer absorption having a significant contribution of the ν(C–S) and ring deformation mode, respectively. Moreover, for the neat solid **s-OH**, a characteristic strong band appears at ~1102 cm^{-1}, which compares also well with the monomer absorption due to the ν(C=S) mode coupled with vibrations of the ring.

3.2 Tautomerization of neat solid thiotropolone induced by thermal and vibrational excitation

Upon generation of the thiol-keto **a-SH** tautomer in the neat solid phases by visible light irradiation (λ ≥ 400 nm) of the thione-enol **s-OH** tautomer at 15 K, the sample was warmed to investigate the occurrence of thermal transformations. The initial temperature was increased to 20 K and then increased in steps of 10 K, and changes were monitored by recording IR spectra. The neat solid sample containing **a-SH** was found to be thermally stable until 60 K (at least on the 5−10 min time scale of spectra acquisition). Similarly, monomeric **a-SH** generated in a xenon matrix was also found to be stable in the course of annealing up to 60 K (Figure S8). At temperatures above 60 K, xenon starts to evaporate, and aggregation of **TT** occurs, which precludes further investigations on the monomeric sample. Because the reaction barrier for the transformation of **a-SH** was shown not to be surpassed at temperatures up to 60 K, either in the neat solid phases or in the matrices containing the monomeric **TT**, one can conclude that it shall be higher than ~18 kJ mol^{-1} (see section 2.4 for details). However, significant transformation of

a-SH back to **s-OH** was observed to start at 70 K in neat solid, with complete conversion achieved when the temperature reached 100 K (Figure 3). The difference IR spectrum obtained upon annealing up to 100 K nicely mirrors the difference spectrum corresponding to the **s-OH** → **a-SH** transformation resulting from irradiation of **s-OH** with visible light, described in Section 3.1 (Figure 2c). For instance, the characteristic IR bands at 1617, 1558, 776 and 562 cm^{-1} of neat solid **a-SH**, previously identified to be produced upon **s-OH** → **a-SH** photo-tautomerization, are now observed to be consumed. Concomitantly, the characteristic IR bands at 1550–1400, 1102, 738/723, and 592 cm^{-1} of neat solid **s-OH**, previously identified to be consumed upon **s-OH** → **a-SH** photo-tautomerization, are now observed to grow in the spectrum of the annealed sample.

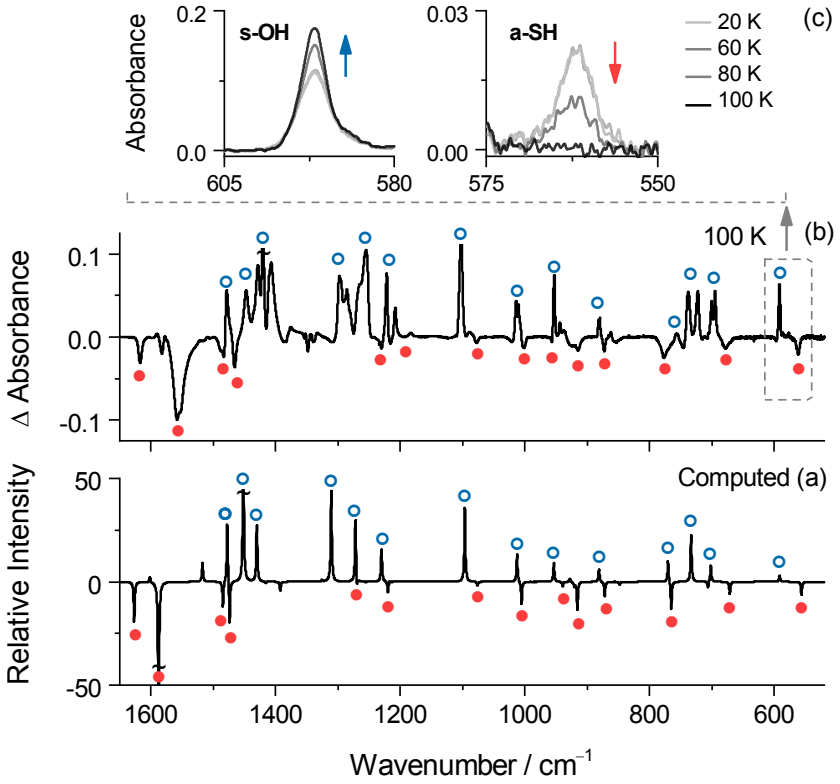

Figure 3. (a) Computed IR difference spectrum based on B3LYP/6-311+G(2d,p) vibrational data considering the transformation of **a-SH** into **s-OH** (ratio 1:1). (b) Experimental difference IR spectrum (spectrum after annealing at 100 K "minus" spectrum of the same sample at 15 K before annealing) displaying the thermal transformation induced by annealing from 15 to 100 K. Bands marked with filled (●) and empty (○) circles are assigned to consumed **a-SH** and produced **s-OH**, respectively. (c) Expanded region of the IR spectrum (600−550 cm^{-1}) showing the evolution of a pair of bands assigned to **s-OH** (left panel) and **a-SH** (right panel) during the annealing from 20 to 100 K, subsequently to irradiation ($\lambda \geq 400$ nm) of the neat solid of **TT** shown in Figure 2. Bands designated with tilde (~) are truncated.

Noteworthy, when **a-SH**, first photo-generated in the neat solid, was warmed in a single step from 60 to 100 K, only traces of this tautomer were detected in the first IR spectrum collected (in approx. 5 min), and no signals were detected in the second spectrum registered (*i.e.*, after ~10 min). This result indicates that 100 K is approximately the upper temperature limit for detection of **a-SH** using steady state spectroscopy, and that above this temperature only the **s-OH** form exists.[84] The observed thermal transformation of **a-SH** shall take place *via* SH-rotamerization to **s-SH** followed by tautomerization to **s-OH** *via* H-shift (Figure 4). Because of a low and thin barrier associated with the tautomerization step [~9 kJ mol^{-1} and ~0.63 Å, estimated at the B3LYP/6-311+G(2d,p) level], spontaneous quantum tunneling makes **s-SH** a fleeting species even under cryogenic conditions [estimated tunneling half-life time ~1×10^{-11} s WKB model].[31] Therefore, it is the SH-rotamerization step that dictates the reactivity of **a-SH** towards **s-OH**. Note that no spontaneous SH-rotamerization tunneling of **a-SH** to **s-SH** takes place at very low temperatures because of a relatively high and wide barrier associated with this transformation [the computed **a-SH** tunneling half-life time is ~1.4×10^{11} s (approx. 4500 years) using the WKB model (Section 2.4)].[85]

At our best available composite G4 model, the SH-rotamerization barrier for the **a-SH** → **s-SH** process is ~25.3 kJ mol^{-1} (Figure 4). Based on a compilation of results regarding conformational isomerism of molecules isolated in cryogenic matrices, Barnes proposed a rough empirical correlation between the barrier height for conformational isomerization and the temperature at which that transformation is observed upon annealing.[70] That correlation resorts essentially to the application of the Arrhenius equation, by assuming a pre-exponential factor A = $10^{11.2}$ and considering a first order reaction rate constant between an upper (too slow) and lower (too fast) limit half-life time of 10^4 and 10^2 s, respectively.[70,71] Considering our experimental results, which indicate that at ~100 K the **a-SH** → **s-SH** reaction rate is on the lower limit half-life time for its observation (*i.e.* ~10^2 s), by applying the above-mentioned correlation one estimates a reaction barrier of roughly ~26 kJ mol^{-1} (see also Section 2.4). The fair agreement between the predicted barrier based on empirical correlation[70,71] and the G4 computed SH-rotamerization barrier further supports our experimental analysis regarding the thermal **a-SH** → **s-OH** transformation in the neat solid conditions. It also suggests that the intermolecular interactions in neat solid **TT** should be relatively weak and should not significantly affect the reaction energy barriers compared to those in gas-phase (computed for monomers).

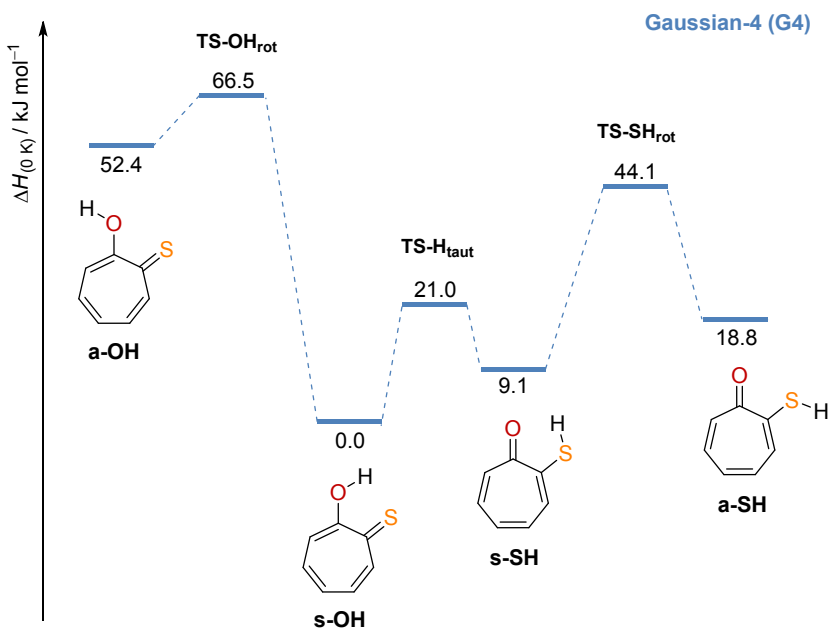

Figure 4. Gaussian-4 (G4) computed reaction pathways for tautomerization (H-shift) and rotamerizations (OH and SH torsion) involving the most relevant isomers of thiotropolone (**TT**). Horizontal bars represent the ZPE corrected relative energies (including also the numeric values) at each stationary point ($\Delta H_{(0\,K)}$ in kJ mol^{-1}).

We have previously demonstrated that bidirectional thione-enol **s-OH** ↔ thiol-keto **a-SH** tautomerization of monomeric **TT** in an argon matrix can be achieved by excitation of CH stretching overtone/combination modes of the corresponding reactant species.[31] In the present study, we investigated if vibrationally-induced tautomerization of **TT** can also be triggered in neat solid conditions. The near-IR spectrum of monomeric **s-OH** in an argon matrix was reported to have two bands at 5980 and 5940 cm^{-1}, assigned to overtones and combinations of ν(CH) modes.[31] In the near-IR spectrum of neat solid **s-OH** (crystalline and amorphous forms) no bands were observed. Assuming that no significant differences should occur in the frequencies of such vibrational modes when the cryogenic sample goes from monomeric to neat solid,[86] the neat solid **s-OH** at 15 K was irradiated using near-IR light tuned at 5980 and 5940 cm^{-1}. No traces of any transformation were detected, which was not surprising because the infrared-induced **s-OH** → **a-SH** tautomerization was already reported to occur in low yields for the monomeric species isolated in an argon matrix. Moreover, the IR absorbance cross sections of CH stretching overtones/combination modes of **s-OH** in neat solid seem to be weaker or broader (because these were not observed) than for the monomer in an argon matrix, which makes the energy deposition upon vibrational excitation more unfavorable under neat solid conditions.

Subsequently, the vibrational excitation of neat solid **a-SH** (produced by means of **s-OH** visible-light irradiation, with λ ≥ 400 nm) was investigated. Note that in an argon matrix, the **a-SH** → **s-OH** tautomerization was observed to be much more efficient than the **s-OH** → **a-SH** one. Although, in the near-IR spectrum of neat solid **a-SH** no bands were observed, it was assumed that the overtones/combinations of the ν(CH) modes should absorb close to 5994 and 5947 cm^{-1}, the frequencies identified for monomeric **a-SH** species in an argon matrix.[31] Remarkably, upon near-IR light irradiation at these frequencies, the thiol-keto **a-SH** → thione-enol **s-OH** tautomerization was observed in neat solid conditions at 15 K. As shown in Figure 5, the observed intensity changes of the bands in the spectrum are identical to those corresponding to the thermal **a-SH** → **s-OH** tautomerization in neat solid upon annealing described before (Figure 3b). As expected, near-IR irradiations tuned at a frequency outside the range of the CH stretching overtones/combination modes (e.g. at 7000 cm^{-1} where no vibrational transitions are expected) did not lead to any transformation. It is therefore demonstrated here that the **a-SH** transformation into **s-OH** can be induced both by a thermal process and by vibrational excitation (Scheme 3).

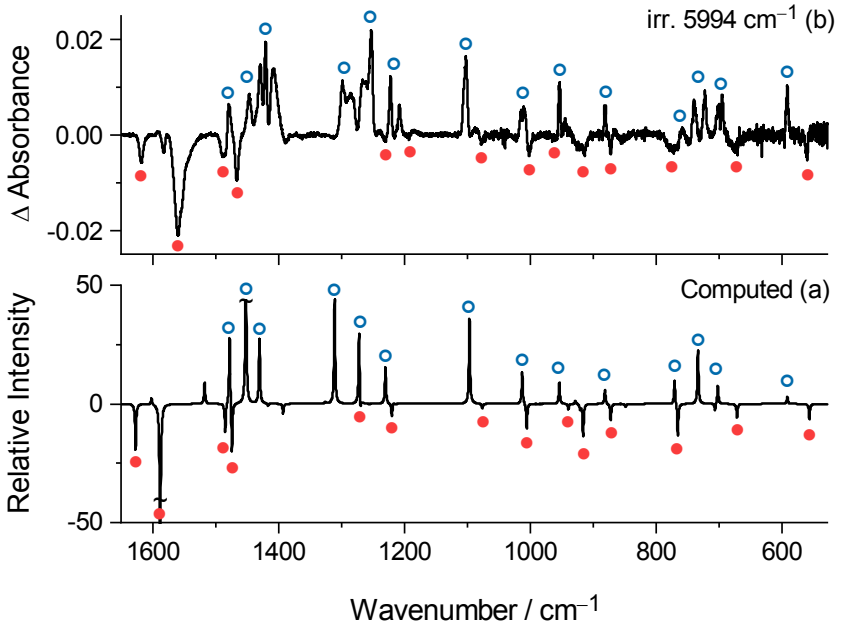

Figure 5. (a) Computed IR difference spectrum based on B3LYP/6-311+G(2d,p) vibrational data considering the transformation of **a-SH** into **s-OH** (ratio 1:1). (b) Experimental difference IR spectrum (spectrum after irradiation at 5994 cm^{-1} "minus" spectrum of the same sample before irradiation) displaying the vibrationally induced tautomerization of **a-SH** neat solid at 15 K. Bands marked with filled (●) and empty (○) circles are assigned to consumed **a-SH** and produced **s-OH**, respectively. Bands designated with tilde (~) are truncated.

Scheme 3. Transformation of neat solid a-SH into s-OH induced by a thermal process and by vibrational excitation

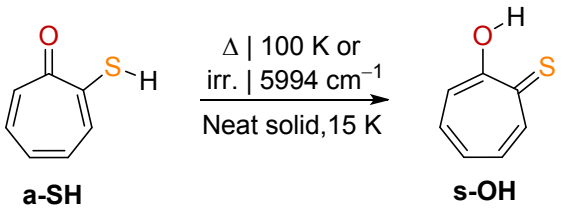

4. CONCLUSIONS

Our results provide valuable new insights into understanding the structural chemistry of thiotropolone (**TT**) and its tautomerism in the solid state. The presented vibrational spectroscopic results clearly demonstrate that monomeric **TT**, isolated in inert matrices (argon and xenon) at low temperatures, and **TT** molecules, isolated in neat solid amorphous and crystalline conditions at temperatures ranging from 15 to 200 K, exist in the same and unique tautomeric structure, the thione-enol **s-OH** form. Subsequent visible light irradiation with $\lambda \geq 400$ nm was found to induce thione-enol → thiol-keto (**s-OH** → **a-SH**) tautomerization in matrices as well as in neat solid conditions at 15 K. The detailed vibrational assignment in the mid-IR range of the two **TT** tautomers was carried out with the support of harmonic and anharmonic B3LYP/6-311+G(2d,p) computations. Upon the phototautomerization, it was found that annealing of the neat solid samples to 100 K leads to the conversion of **a-SH** back to **s-OH**. Because of such thermally-induced tautomerization decay, only the most stable **s-OH** tautomer exists above 100 K. Mechanistically, the observed thermal transformation of **a-SH** should be dictated by SH-rotamerization to **s-SH**, because the subsequent tautomerization step of **s-SH** to **s-OH** should occur instantaneously by fast H-tunneling. Gaussian-4 (G4) computations estimate an energy barrier for the SH-rotamerization of **a-SH** to be about ~25 kJ mol^{-1}, which is consistent with the observation of the thermal tautomerization at around 100 K. Finally, it was also found that narrowband IR light irradiation of thiol-keto **s-OH** form in neat solid, at the frequency of its CH stretching overtones/combination modes, promotes tautomerization to the thione-enol **s-SH**. As far as we are aware, such results constitute a pioneer demonstration of chemistry induced by vibrational excitation in neat solid conditions, which opens opportunities for developing a new tool to achieve controlled manipulation of molecules in solid crystalline or amorphous state.

ASSOCIATED CONTENT

Supporting Information. The Supporting Information is available free of charge on the ACS Publications website at DOI: xxx.xxx.xxx. Detail vibrational analysis and assignments, additional experimental and computational results.

AUTHOR INFORMATION

Corresponding Author

*cmnunes@qui.uc.pt

Author Contributions

C.M.N. conceived the original working hypothesis. N.A.M.P. performed the synthesis. N.A.M.P. and C.M.N. performed the experiments, computations and analyzed the data. I.R. performed the vibrational analysis and assignments. All authors discussed the results and co-wrote the manuscript.

Notes

The authors declare no competing interests.

ACKNOWLEDGMENTS

This work was supported by Projects POCI-01-0145-FEDER-028973 and PTDC/QUI-QFI/1880/2020, funded by National Funds *via* the Portuguese Foundation for Science and Technology (FCT), the first being also funded by FEDER, *via* Portugal 2020 - POCI. The Coimbra Chemistry Centre (CQC) is supported by FCT through projects UIDB/00313/2020 and UIDP/00313/2020 co-funded by COMPETE, and the Chemical Process Engineering and Forest Products Research Centre (CIEPQPF) is supported by FCT through projects UIDB/EQU/00102/2020 and UIDP/EQU/00102/2020. C.M.N. acknowledges FCT for an Auxiliary Researcher grant. N.A.M.P. acknowledges the Project POCI-01-0145-FEDER-028973 for a Junior Researcher grant. Patrícia S. M. Amado and Maria L. S. Cristiano are acknowledged for the synthetic work on thiotropolone in our previous study.

REFERENCES

(1) Horiuchi, S.; Kobayashi, K.; Kumai, R.; Ishibashi, S. Proton Tautomerism for Strong Polarization Switching. *Nat. Commun.* **2017**, *8*, 14426.

(2) *Tautomerism: Concepts and Applications in Science and Technology*; Antonov, L., Ed.; Wiley-VCH: Weinheim, 2016.

(3) *Tautomerism: Methods and Theories*; Antonov, L., Ed.; Wiley-VCH: Weinheim, 2014.

(4) Katritzky, A. R.; Dennis Hall, C.; El-Gendy, B. E. D. M.; Draghici, B. Tautomerism in Drug Discovery. *J. Comput. Aided. Mol. Des.* **2010**, *24*, 475–484.

(5) Martin, Y. C. Let's Not Forget Tautomers. *J. Comput. Aided. Mol. Des.* **2009**, *23*, 693–704.

(6) Claramunt, R. M.; López, C.; Santa María, M. D.; Sanz, D.; Elguero, J. The Use of NMR Spectroscopy to Study Tautomerism. *Prog. Nucl. Magn. Reson. Spectrosc.* **2006**, *49*, 169–206.

(7) Raczyńska, E. D.; Kosińska, W.; Ośmiałowski, B.; Gawinecki, R. Tautomeric Equilibria in Relation to Pi-Electron Delocalization. *Chem. Rev.* **2005**, *105*, 3561–3612.

(8) Rubčić, M.; Užarević, K.; Halasz, I.; Bregović, N.; Mališ, M.; Dilović, I.; Kokan, Z.; Stein, R. S.; Dinnebier, R. E.; Tomišić, V. Desmotropy, Polymorphism, and Solid-State Proton Transfer: Four Solid Forms of an Aromatic o-Hydroxy Schiff Base. *Chem. Eur. J.* **2012**, *18*, 5620–5631.

(9) Sugawara, T.; Takasu, I. Tautomerism in the Solid State. *Adv. Phys. Org. Chem.* **1999**, *32*, 219–265.

(10) Elguero, J. Polymorphism and Desmotropy in Heterocyclic Crystal Structures. *Cryst. Growth Des.* **2011**, *11*, 4731–4738.

(11) Bhatt, P. M.; Desiraju, G. R. Tautomeric Polymorphism in Omeprazole. *Chem. Commun.* **2007**, 2057–2059.

(12) Blake, A. J.; Lin, X.; Schröder, M.; Wilson, C.; Yuan, R. X. The Imide Tautomer of Sulfasalazine. *Acta Crystallogr. Sect. C Cryst. Struct. Commun.* **2004**, *60*, 226–228.

(13) Mirmehrabi, M.; Rohani, S.; Murthy, K. S. K.; Radatus, B. Characterization of Tautomeric Forms of Ranitidine Hydrochloride: Thermal Analysis, Solid-State NMR, X-Ray. *J. Cryst. Growth* **2004**, *260*, 517–526.

(14) Nowak, M. J.; Reva, I.; Rostkowska, H.; Lapinski, L. UV-Induced Hydrogen-Atom Transfer and Hydrogen-Atom Detachment in Monomeric 7-Azaindole Isolated in Ar and n-H_2 Matrices. *Phys. Chem. Chem. Phys.* **2017**, *19*, 11447–11454.

(15) Nowak, M. J.; Lapinski, L.; Kwiatkowski, J. S.; Leszczynski, J. Infrared Matrix Isolation and Ab Initio Quantum Mechanical Studies of Purine and Adenine. *Spectrochim. Acta Part A Mol. Spectrosc.* **1991**, *47*, 87–103.

(16) Nowak, M. J.; Lapinski, L.; Kwiatkowski, J. S.; Leszczyński, J. Molecular Structure and Infrared Spectra of Adenine. Experimental Matrix Isolation and Density Functional Theory Study of Adenine ^{15}N Isotopomers. *J. Phys. Chem.* **1996**, *100*, 3527–3534.

(17) Lapinski, L.; Reva, I.; Nowak, M. J.; Fausto, R. Five Isomers of Monomeric Cytosine and Their Interconversions Induced by Tunable UV Laser Light. *Phys. Chem. Chem. Phys.* **2011**, *13*, 9676–9684.

(18) Reva, I.; Nowak, M. J.; Lapinski, L.; Fausto, R. UV-Induced Amino → Imino Hydrogen-Atom Transfer in 1-Methylcytosine. *J. Phys. Chem. B* **2012**, *116*, 5703–5710.

(19) Vranken, H.; Smets, J.; Maes, G.; Lapinski, L.; Nowak, M. J.; Adamowicz, L. Infrared Spectra and Tautomerism of Isocytosine; an Ab Initio and Matrix Isolation Study. *Spectrochim. Acta Part A Mol. Spectrosc.* **1994**, *50*, 875–889.

(20) Gerega, A.; Lapinski, L.; Nowak, M. J.; Rostkowska, H. UV-Induced Oxo → Hydroxy Unimolecular Proton-Transfer Reactions in Hypoxanthine. *J. Phys. Chem. A* **2006**, *110*, 10236–10244.

(21) Nowak, M. J.; Lapinski, L.; Fulara, J.; Les, A.; Adamowicz, L. Matrix Isolation IR Spectroscopy of Tautomeric Systems and Its Theoretical Interpretation: 2-Hydroxypyridine/2(1*H*)-Pyridinone. *J. Phys. Chem.* **1992**, *96*, 1562–1569.

(22) Gerega, A.; Lapinski, L.; Nowak, M. J.; Furmanchuk, A.; Leszczynski, J. Systematic Effect of Benzo-Annelation on Oxo-Hydroxy Tautomerism of Heterocyclic Compounds. Experimental Matrix-Isolation and Theoretical Study. *J. Phys. Chem. A* **2007**, *111*, 4934–4943.

(23) Nowak, M. J.; Lapinski, L.; Rostkowska, H.; Leś, A.; Adamowicz, L. Theoretical and Matrix-Isolation Experimental Study on 2(1*H*)-Pyridinethione/2-Pyridinethiol. *J. Phys. Chem.* **1990**, *94*, 7406–7414.

(24) Lapiński, L.; Nowak, M. J.; Kwiatkowski, J. S.; Leszczynski, J. Phototautomeric

Reaction, Tautomerism, and Infrared Spectra of 6-Thiopurine. Experimental Matrix Isolation and Quantum-Mechanical (Conventional Ab Initio and Density-Functional Theory) Studies. *J. Phys. Chem. A* **1999**, *103*, 280–288.

(25) Prusinowska, D.; Lapinski, L.; Nowak, M. J.; Adamowicz, L. Tautomerism, Phototautomerism and Infrared Spectra Of Matrix-Isolated 2-Quinolinethione. *Spectrochim. Acta - Part A Mol. Spectrosc.* **1995**, *51*, 1809–1826.

(26) Brás, E. M.; Fausto, R. Controlled Light-Driven Switching in 2-Thiobenzimidazole. *J. Photochem. Photobiol. A Chem.* **2018**, *357*, 185–192.

(27) Brás, E. M.; Fausto, R. An Insight into Methimazole Phototautomerism: Central Role of the Thiyl Radical and Effect of Benzo Substitution. *J. Mol. Struct.* **2018**, *1172*, 42–54.

(28) Góbi, S.; Nunes, C. M.; Reva, I.; Tarczay, G.; Fausto, R. S-H Rotamerization *via* Tunneling in a Thiol Form of Thioacetamide. *Phys. Chem. Chem. Phys.* **2019**, *21*, 17063–17071.

(29) Góbi, S.; Reva, I.; Csonka, I. P.; M. Nunes, C.; Tarczay, G.; Fausto, R. Selective Conformational Control by Excitation of NH Imino Vibrational Antennas. *Phys. Chem. Chem. Phys.* **2019**, *21*, 24935–24949.

(30) Rostkowska, H.; Lapinski, L.; Nowak, M. J. Hydrogen-Atom Tunneling through a Very High Barrier; Spontaneous Thiol → Thione Conversion in Thiourea Isolated in Low-Temperature Ar, Ne, H_2 and D_2 Matrices. *Phys. Chem. Chem. Phys.* **2018**, *20*, 13994–14002.

(31) Nunes, C. M.; Pereira, N. A. M.; Reva, I.; Amado, P. S. M.; Cristiano, M. L. S.; Fausto, R. Bond-Breaking/Bond-Forming Reactions by Vibrational Excitation: Infrared-Induced Bidirectional Tautomerization of Matrix-Isolated Thiotropolone. *J. Phys. Chem. Lett.* **2020**, *11*, 8034–8039.

(32) Fausto, R.; Khriachtchev, L.; Hamm, P. Conformational Changes in Cryogenic Matrices. In *Physics and Chemistry at Low Temperatures*; Khriachtchev, L., Ed.; Pan Stanford Publishing: United States, 2011; pp 51–84.

(33) Pettersson, M.; Lundell, J.; Khriachtchev, L.; Räsänen, M. IR Spectrum of the Other Rotamer of Formic Acid, Cis-HCOOH. *J. Am. Chem. Soc.* **1997**, *119*, 11715–11716.

(34) Nunes, C. M.; Reva, I.; Fausto, R. Conformational Isomerizations Triggered by Vibrational Excitation of Second Stretching Overtones. *Phys. Chem. Chem. Phys.* **2019**,

21, 24993–25001.

(35) Dzugan, L. C.; Matthews, J.; Sinha, A.; McCoy, A. B. Role of Torsion-Vibration Coupling in the Overtone Spectrum and Vibrationally Mediated Photochemistry of CH_3OOH and HOOH. *J. Phys. Chem. A* **2017**, *121*, 9262–9274.

(36) Liu, F.; Beames, J. M.; Petit, A. S.; McCoy, A. B.; Lester, M. I. Infrared-Driven Unimolecular Reaction of CH_3CHOO Criegee Intermediates to OH Radical Products. *Science.* **2014**, *345*, 1596–1598.

(37) Matthews, J.; Fry, J. L.; Roehl, C. M.; Wennberg, P. O.; Sinha, A. Vibrational Overtone Initiated Unimolecular Dissociation of $HOCH_2OOH$ and $HOCD_2OOH$: Evidence for Mode Selective Behavior. *J. Chem. Phys.* **2008**, *128*, 1–13.

(38) Leytner, S.; Snavely, D. L.; Grinevich, O. Reversible Isomerization of Methylcyclopentadienes Directed by Selective Excitation of the Methyl Out-of-Plane Fourth Overtone Transition. *Chem. Phys. Lett.* **1997**, *277*, 443–449.

(39) Snavely, D. L.; Grinevich, O.; Hassoon, S.; Snavely, G. Vibrational Overtone Activation of Methylcyclopropene. *J. Chem. Phys.* **1996**, *104*, 5845–5851.

(40) Hassoon, S.; Rajapakse, N.; Snavely, D. L. Vibrational Overtone Activation of the Isomerization of Methyl Isocyanide. *J. Phys. Chem.* **1992**, *96*, 2576–2581.

(41) Lishan, D. G.; Reddy, K. V.; Hammond, G. S.; Leonard, J. E. Overtone Vibrational Photochemistry of Quadricyclane. *J. Phys. Chem.* **1988**, *92*, 656–660.

(42) Jasinski, J. M.; Frisoli, J. K.; Moore, C. B. High Vibrational Overtone Photochemistry of 1-Cyclopropylcyclobutene. *J. Chem. Phys.* **1983**, *79*, 3826–3829.

(43) Several examples have been reported regarding the vibrational control of bimolecular reactions (mode and bond selectivity) with CH_4 (and isotopically substituted analogs) + atoms (H, O, F, Cl, etc.) and with H_2O (and isotopically substituted analogs) + atoms (H, O, F, Cl, etc.). See for instance: Liu, K. Vibrational Control of Bimolecular Reactions with Methane by Mode, Bond, and Stereo Selectivity. *Annu. Rev. Phys. Chem.* **2016**, *67*, 91–111 and references cited therein.

(44) Stensitzki, T.; Yang, Y.; Kozich, V.; Ahmed, A. A.; Kössl, F.; Kühn, O.; Heyne, K. Acceleration of a Ground-State Reaction by Selective Femtosecond-Infrared-Laser-Pulse Excitation. *Nat. Chem.* **2018**, *10*, 126–131.

(45) Shin, J. Y.; Shaloski, M. A.; Crim, F. F.; Case, A. S. First Evidence of Vibrationally

Driven Bimolecular Reactions in Solution: Reactions of Br Atoms with Dimethylsulfoxide and Methanol. *J. Phys. Chem. B* **2017**, *121*, 2486–2494.

(46) Gutow, J. H.; Klenerman, D.; Zare, R. N. Comparison of Overtone-Induced and Electronic Photochemistry of Liquid Tert-Butyl Hydroperoxide: Supporting Evidence for Vibrational Mode Selectivity. *J. Phys. Chem.* **1988**, *92*, 172–177.

(47) Schwebel, A.; Brestel, M.; Yogev, A. Site-Selective Liquid-Prase Vibrational Overtone Photochemistry of Hydroxyhexadiene. *Chem. Phys. Lett.* **1984**, *107*, 579–584.

(48) Paine, S. W.; Salam, A. Computational Study of Tautomerism and Aromaticity in Mono- and Dithio-Substituted Tropolone. *Int. J. Quantum Chem.* **2013**, *113*, 1245–1252.

(49) Durlak, P.; Latajka, Z. Investigations of the Hydrogen Bond in the Crystals of Tropolone and Thiotropolone via Car-Parrinello and Path Integral Molecular Dynamics. *J. Comput. Chem.* **2019**, *40*, 671–687.

(50) Machiguchi, T.; Hasegawa, T.; Saitoh, H.; Yamabe, S.; Yamazaki, S. Solid-State Thiotropolone: An Extremely Rapid Intramolecular Proton Transfer. *J. Org. Chem.* **2011**, *76*, 5457–5460.

(51) Fernández-Ramos, A. Correct Interpretation of How Tunneling Proceeds at Low Temperatures in the Proton Transfer Reactions Involving Thiotropolone: A Comment. *Angew. Chem. Int. Ed.* **2013**, *52*, 8204–8205.

(52) Frisch, M. J.; Trucks, G. W.; Schlegel, H. B.; Scuseria, G. E.; Robb, M. A.; Cheeseman, J. R.; Scalmani, G.; Barone, V.; Petersson, G. A.; Nakatsuji, H., et al. *Gaussian 16*, Revision B.01; Gaussian, Inc.: Wallingford, CT, 2016.

(53) Becke, A. D. Density-Functional Thermochemistry. III. The Role of Exact Exchange. *J. Chem. Phys.* **1993**, *98*, 5648–5652.

(54) Lee, C.; Yang, W.; Parr, R. G. Development of the Colle-Salvetti Correlation-Energy into a Functional of the Electron Density. *Phys. Rev. B Condens. Matter* **1988**, *37*, 785–789.

(55) Vosko, S. H.; Wilk, L.; Nusair, M. Accurate Spin-Dependent Electron Liquid Correlation Energies for Local Spin Density Calculations: A Critical Analysis. *Can. J. Phys.* **1980**, *58*, 1200–1211.

(56) Ditchfield, R.; Hehre, W. J.; Pople, J. A. Self-Consistent Molecular-Orbital Methods. IX. An Extended Gaussian-Type Basis for Molecular-Orbital Studies of Organic Molecules. *J. Chem. Phys.* **1971**, *54*, 724–728.

(57) Nunes, C. M.; Eckhardt, A. K.; Reva, I.; Fausto, R.; Schreiner, P. R. Competitive Nitrogen versus Carbon Tunneling. *J. Am. Chem. Soc.* **2019**, *141*, 14340–14348.

(58) Teixeira, F.; Cordeiro, M. N. D. S. Improving Vibrational Mode Interpretation Using Bayesian Regression. *J. Chem. Theory Comput.* **2019**, *15*, 456–470.

(59) Barone, V. Anharmonic Vibrational Properties by a Fully Automated Second-Order Perturbative Approach. *J. Chem. Phys.* **2005**, *122*, 014108.

(60) Bloino, J.; Barone, V. A Second-Order Perturbation Theory Route to Vibrational Averages and Transition Properties of Molecules: General Formulation and Application to Infrared and Vibrational Circular Dichroism Spectroscopies. *J. Chem. Phys.* **2012**, *136*, 124108.

(61) Runge, E.; Gross, E. K. U. Density-Functional Theory for Time-Dependent Systems. *Phys. Rev. Lett.* **1984**, *52*, 997–1000.

(62) Bauernschmitt, R.; Ahlrichs, R. Treatment of Electronic Excitations within the Adiabatic Approximation of Time Dependent Density Functional Theory. *Chem. Phys. Lett.* **1996**, *256*, 454–464.

(63) Stratmann, R. E.; Scuseria, G. E.; Frisch, M. J. An Efficient Implementation of Time-Dependent Density-Functional Theory for the Calculation of Excitation Energies of Large Molecules. *J. Chem. Phys.* **1998**, *109*, 8218–8224.

(64) Curtiss, L. A.; Redfern, P. C.; Raghavachari, K. Gaussian-4 Theory. *J. Chem. Phys.* **2007**, *126*, 084108.

(65) Nunes, C. M.; Reva, I.; Fausto, R. Direct Observation of Tunnelling Reactions by Matrix Isolation Spectroscopy. In *Tunnelling in Molecules: Nuclear Quantum Effects from Bio to Physical Chemistry*; Kozuch, S., Kästner, J., Eds.; Royal Society of Chemistry, 2021; pp 1–60.

(66) Wentzel, G. Eine Verallgemeinerung der Quantenbedingungen für die Zwecke der Wellenmechanik. *Zeitschrift für Phys.* **1926**, *38*, 518–529.

(67) Kramers, H. A. Wellenmechanik und Halbzahlige Quantisierung. *Zeitschrift für Phys.* **1926**, *39*, 828–840.

(68) Brillouin, L. La Mécanique Ondulatoire de Schrödinger; Une Méthode Générale de Resolution Par Approximations Successives. *Compt. Rend. Hebd. Seances Acad. Sci.* **1926**, *183*, 24–26.

(69) Borden, W. T. Reactions That Involve Tunneling by Carbon and the Role That Calculations Have Played in Their Study. *WIREs Comput. Mol. Sci.* **2016**, *6*, 20–46.

(70) Barnes, A. J. Matrix Isolation Vibrational Spectroscopy as a Tool for Studying Conformational Isomerism. *J. Mol. Struct.* **1984**, *113*, 161–174.

(71) Pong, R.; Goldfarb, T. D.; Krantz, A. Kinetic Studies in Various Matrices - Probing the Host-Guest Interaction. *Ber. Bunsenges. Phys. Chem.* **1978**, *82*, 9–10.

(72) Klaeboe, P. Conformational Studies by Vibrational Spectroscopy: A Review of Various Methods. *Vib. Spectrosc.* **1995**, *9*, 3–17.

(73) Nowak, M. J.; Rostkowska, H.; Lapinski, L.; Leszczynski, J.; Kwiatkowski, J. S. Infrared Experimental and Ab Initio Quantum Mechanical Studies of 2-Mercaptopyrimidine Tautomers. *Spectrochim. Acta Part A Mol. Spectrosc.* **1991**, *47*, 339–353.

(74) Rostkowska, H.; Nowak, M. J.; Lapinski, L.; Bretner, M.; Kulikowski, T.; Les, A.; Adamowicz, L. Theoretical and Matrix-Isolation Experimental Studies on 2-Thiocytosine and 5-Fluoro-2-Thiocytosine. *Biochim. Biophys. Acta* **1993**, *1172*, 239–246.

(75) Czermiínski, R.; Kuczera, K.; Rostkowska, H.; Nowak, M. J.; Szczepaniak, K. Autoassociates and Tautomerism of 2-Oxo-5-Halogenopyrimidines: Theoretical and Experimental Investigations. *J. Mol. Struct.* **1986**, *140*, 235–251.

(76) Nowak, M. J.; Fulara, J.; Łapiński, L. IR Spectra and Phototautomerism of Matrix Isolated 4-Oxopyrimidine. *J. Mol. Struct.* **1988**, *175*, 91–96.

(77) As it will be presented in the section 3.2, another argument suporting the identification of **a-SH** and the exclusion of **s-SH** is the observed thermal stability of the new tautomer in xenon matrix in the course of annealing up to 60 K (before the matrix starts to evaporate) and its thermal transformation under neat-solid conditions upon anneling to 80-100 K, which correlates well with the computed **a-SH** to **s-OH** energy barrier of ~25 kJ mol^{-1} but are clearly incompatible with the formation of **s-SH** because (even neglecting the occurrence of H-tunneling) its computed tautomerization barrier to **s-OH** is ~10 kJ mol^{-1}.

(78) Rostkowska, H.; Szczepaniak, K.; Nowak, M. J.; Leszczynski, J.; KuBulat, K.; Person, W. B. Tautomerism and Infrared Spectra of Thiouracils. Matrix Isolation and Ab Initio Studies. *J. Am. Chem. Soc.* **1990**, *112*, 2147–2160.

(79) Reva, I.; Nowak, M. J.; Lapinski, L.; Fausto, R. Hydrogen Atom Transfer Reactions in Thiophenol: Photogeneration of Two New Thione Isomers. *Phys. Chem. Chem. Phys.*

2015, *17*, 4888–4898.

(80) Nogueira, B. A.; Castiglioni, C.; Fausto, R. Color Polymorphism in Organic Crystals. *Commun. Chem.* **2020**, *3*, 34.

(81) Gonzalez, A.; Kengmana, E. S.; Fonseca, M. V.; Han, G. G. D. Solid-State Photoswitching Molecules: Structural Design for Isomerization in Condensed Phase. *Mater. Today Adv.* **2020**, *6*, 100058.

(82) Hadjoudis, E.; Mavridis, I. M. Photochromism and Thermochromism of Schiff Bases in the Solid State: Structural Aspects. *Chem. Soc. Rev.* **2004**, *33*, 579–588.

(83) Keating, A. E.; Garcia-Garibay, M. A. Photochemical Solid-to-Solid Reactions In *Organic and Inorganic Photochemistry*; Ramamurthy, V., Schanze, K., Eds.; Marcel Dekker: New York, 1998; Vol. 2; pp 195-248.

(84) Accordingly, when neat solid **s-OH** at 190 K was irradiated with $\lambda \geq 400$ nm the formation of **a-SH** was not detected (*i.e.* no changes were observed in IR spectrum of the **s-OH** sample).

(85) To the best of our knowledge there are only two examples of SH-rotamerization tunneling directly observed by matrix isolation spectroscopy: (i) In a thiol form of thioacetamide, in which the tunneling reaction takes place in argon matrix at 10 K with a half-life time of 80 min [barrier height of 17.0 kJ mol^{-1} and width of ~2.47 Å, estimated at B3LYP/6-311++G(3df,3pd) level] (see ref. 28); (ii) In a thiol form of thioformamide, in which the tunneling reaction takes place in argon matrix at 3 K with a half-life time of 35 min [barrier height of ~15 kJ mol^{-1} estimated at AE-CCSD(T)/aug-cc-pVTZ level] (see: Bernhardt, B.; Dressler, F.; Eckhardt, A. K.; Becker, J.; Schreiner, P. R. Characterization of the Simplest Thiolimine: The Higher Energy Tautomer of Thioformamide. *Chem. Eur. J.* **2021**, *27*, 6732–6739.

(86) Indeed, the C-H stretching fundamentals of **s-OH** seem to have similar absorption frequencies when the compound is isolated in noble gas matrices or when it is studied under neat solid conditions (see Figure S10), a feature that was also observed for other molecules (see for instance ref. 23). Note also that, although the X-ray data reported for **TT** and the corresponding interpretation can still be subject to dispute, especially regarding the position of the H-atom in the vicinity of O and S atoms, it seems clear that the solid **TT** does not have any significant H-bond network (refs. 49,50).

Supporting Information

Evidence of IR-Induced Chemistry in Neat Solid: Tautomerization of Thiotropolone by Thermal, Electronic and Vibrational Excitations

Nelson A. M. Pereira,[1] Cláudio M. Nunes,[1]* Igor Reva,[1,2] and Rui Fausto[1]

[1]University of Coimbra, CQC, Department of Chemistry, 3004-535 Coimbra, Portugal
[2] University of Coimbra, CIEPQPF, Department of Chemical Engineering, 3030-790 Coimbra, Portugal

Email: npereira@qui.uc.pt, cmnunes@qui.uc.pt, reva@eq.uc.pt, rfausto@ci.uc.pt

Table of contents

1. Vibrational assignment of s-OH and a-SH in argon matrix:

The irradiation ($\lambda \geq 400$ nm) of the thione-enol **s-OH** form deposited in an argon matrix at 15 K was found to produce a new tautomer ascribed as the thiol-keto **a-SH** form. Thus, the IR spectra of the sample before and after irradiation contain signatures of two isomeric forms of **TT**: exclusively the **s-OH** tautomer before any irradiation (Figure S5a), and essentially the **a-SH** tautomer after irradiation (Figure S5b). This permits to extract the individual spectrum of the **a-SH** tautomer (Figure S5c) and carry out the vibrational assignment of the two isomers, which is presented in Figure S6. The first striking difference between the experimental spectra of the **s-OH** and **a-SH** tautomers, is a much higher total absorption intensity of the **s-OH** form, as compared to the **a-SH** form. Note that experimental spectra in frames (b) and (c) are shown in the same scale, and they were obtained from the same sample and represent equimolar amounts. The total measured experimental intensity of all bands in the fingerprint (1700-450 cm^{-1}) range for (**s-OH**) is 1.547 times higher than that for (**a-SH**). In order to verify this experimental observation, the (**s-OH**)/(**a-SH**) ratio of the total computed IR intensities in the same range was assessed. This computed ratio equals to 1.569, being in excellent match with the experimental value. Besides a very good overall correspondence between the computed and experimental spectra of each individual **TT** isomer, it appears instructive to distinguish several particular bands / spectral ranges that can be used as discriminative features in the subsequent analysis.

The vibrational assignment of the **s-OH** form is presented in Tables S2 and S3. The most intense IR absorption of the **s-OH** form corresponds to the group of bands in the 1500-1350 cm^{-1} range (Figure S6a and S6b). These bands correspond to the ν_{10}, ν_{11}, ν_{12}, fundamental modes with computed IR intensities from 85 to 232 km mol^{-1}, whose sum corresponds to 30% of intensity in the overall IR spectrum of the **s-OH** isomer. The ν_{10}–ν_{12} fundamental modes correspond to ν(C=C) stretching and δ(CH) in-plane bending vibrations coupled in different fashions with the δCOH mode (Table S2). The experimental spectrum in this range exhibits five strong absorptions, more than the number of predicted fundamentals, and the additional bands must be caused by combination modes which include $\nu_{21}+\nu_{23}$, $\nu_{31}+\nu_{35}$, $\nu_{32}+\nu_{33}$, $\nu_{32}+\nu_{34}$, $2\times\nu_{32}$ pairs, all with IR intensities between 12 and 54 km mol^{-1}, as predicted by anharmonic vibrational computations (Table S3). Fermi-resonance interactions between the ν_{10} –ν_{12} fundamentals and the above combinations, resulting in exchange of IR intensities cannot be excluded either. The important message is that the **s-OH** form exhibits several intense IR absorptions in the 1500-1350 cm^{-1} range, and a comparatively weak

absorption in the 1700-1500 cm^{-1} range. In the latter range, above 1500 cm^{-1}, the ν_7 and ν_8 fundamental ν(C=C) stretching modes are predicted, which however do not couple with the δCOH coordinate (Table S4), and have relatively weak IR absorptions, both computed and observed (Figure S6a and S6b).

Upon the thione-enol → thiol-keto tautomerization in **TT**, there is a dramatic redistribution of spectral intensity above and below 1500 cm^{-1} (see vertical dotted line in Figure S6 between panels S6b and S6c). The fundamental mode ν_8 of **a-SH**, a multiplet band between 1605 and 1585 cm^{-1} (Figure S6c), with predicted intensity of 249 km mol^{-1} (Figure S6d), is alone responsible for 30% of the overall IR intensity of this form, and when summed up with ν_7 and ν_9 this share increases over 42%. Indeed, in the experimental spectrum of **a-SH**, the integrated intensity over the 1700-1500 cm^{-1} range corresponds to 50% (Figure S6c). The reason behind these dramatic changes is that the thiol form of **TT** acquires the carbonyl C=O group, a dipole strongly absorbing in infrared. Indeed, the vibrational analysis of **a-SH** shows that the ν_8 fundamental mode is mainly due to the ν(C=O) stretching (Table S4), and the ν_7 mode due to ν(C=C) is also coupled with ν(C=O). The ν_{10}–ν_{12} fundamental modes of **a-SH**, due to the ν(C=C) stretching and δ(CH) in-plane bending vibrations, appearing below 1500 cm^{-1}, are not coupled anymore with the δCOH coordinate (because the COH group is absent in **a-SH**), nor with ν(C=O), and, hence, these modes become weak in infrared, as evidenced by both the experimental and computed spectra (Figure S6c and S6d). The multiplet character of the experimental absorption of **a-SH** above 1500 cm^{-1} must be caused by combination modes which include $\nu_{21}+\nu_{22}$, $\nu_{17}+\nu_{24}$, $\nu_{14}+\nu_{26}$, $\nu_{30}+\nu_{33}$ pairs, all with IR intensities above 10 km mol^{-1}, as predicted by anharmonic vibrational computations. All these combination bands have predicted frequencies in the vicinity of ν_7 – ν_9 fundamentals (Table S5).

Both **TT** isomers contain five ring CH groups. These CH groups give rise to five γ(CH) out-of-plane vibrations, where typically all CH groups contribute in different phases (modes from γ_a(CH) to γ_e(CH) in Tables S3 and S5). Depending on the phase of each CH group, the resulting change of the dipole moment is either cancelled or enhanced. When displacements of all of these CH groups are coupled in the same phase, this typically gives rise to a very strong infrared band. For example, in the structurally similar phenol monomer, one of five γ(CH) modes originates one of the strongest IR bands observed at 752 cm^{-1}, with computed IR intensity of 84.9 km mol^{-1}.[S1] In the **s-OH** form of **TT**, it is the γ_e(CH) mode (ν_{33}, see Figure S6b), which is predicted to have an IR intensity of 71.8 km mol^{-1}, and is observed as a

strong band at 734.8/732.6 cm^{-1}. The frequencies and couplings of the γ(CH) vibrations sensitively depend on the geometry of the nearest groups, which in **TT** correspond to the OCCS fragment, with an H atom located on either oxygen (in **s-OH**) or sulphur (in **a-SH**). Indeed, upon thione-enol → thiol-keto tautomerization of **TT**, the strongest IR active γ_e(CH) mode of **a-SH** (ν_{32}, see Figure S6c) is observed at 770.2 cm^{-1}, *i.e.* 35-37 cm^{-1} higher in frequency than the similar mode of **s-OH**.

Another important structural change in the **TT** molecule related with the tautomerization, is the change of the CS bond length. In the optimized geometry of **s-OH**, the CS bond is 169.4 pm, while for **a-SH** it elongates to 176.4 pm. This geometric change should be reflected in the value of the ν(CS) stretching frequency. A characteristic strong IR band due to the ν(C=S) mode of **s-OH** (ν_{18}) appears at 1114 cm^{-1} coupled with vibrations of the ring. In both isomers of **TT**, also the ν_{23} mode has some contributions of ν(CS). For the **a-SH** band observed at 563.5 cm^{-1} (Figure S6c), the ν(C−S) stretching mode has a dominant contribution, while the **s-OH** band observed at 599.8 cm^{-1} (Figure S6b) has a minor contribution of ν(C=S), corresponding essentially to a ring deformation mode.

The computed spectrum suggests also that the ν_6 mode, due to the ν(OH) stretching in the **s-OH** form (Figure S6a), might be used for the spectral identification of this form. However, the syn-OH group is involved in a very strong intramolecular H-bond. As it is typical of such cases,[S2,S3] the corresponding experimental absorption is very difficult to observe: this mode gives rise to a very broad absorption extended over several hundreds of wavenumbers, in the case of **TT**, approximately from 2900 to 2300 cm^{-1} (Figure S7a). This very broad feature disappears upon **s-OH** → **a-SH** tautomerization. However, its peak intensity is two orders of magnitude lower than the bands in the fingerprint range (see Figure S6b and Figure S7a) and this mode cannot be used for reliable spectral differentiation between **s-OH** and **a-SH**. As it is clear from Figure S7, the ν(CH) stretching modes ($\nu_1 - \nu_5$) in both isomers are also very weak, appearing at nearly the same frequencies (3200 to 2900 cm^{-1}), and have similar band shapes; like the band due to ν(OH), they cannot be used to easily distinguish between the thione-enol and thiol-keto tautomers of **TT**.

2. Figures

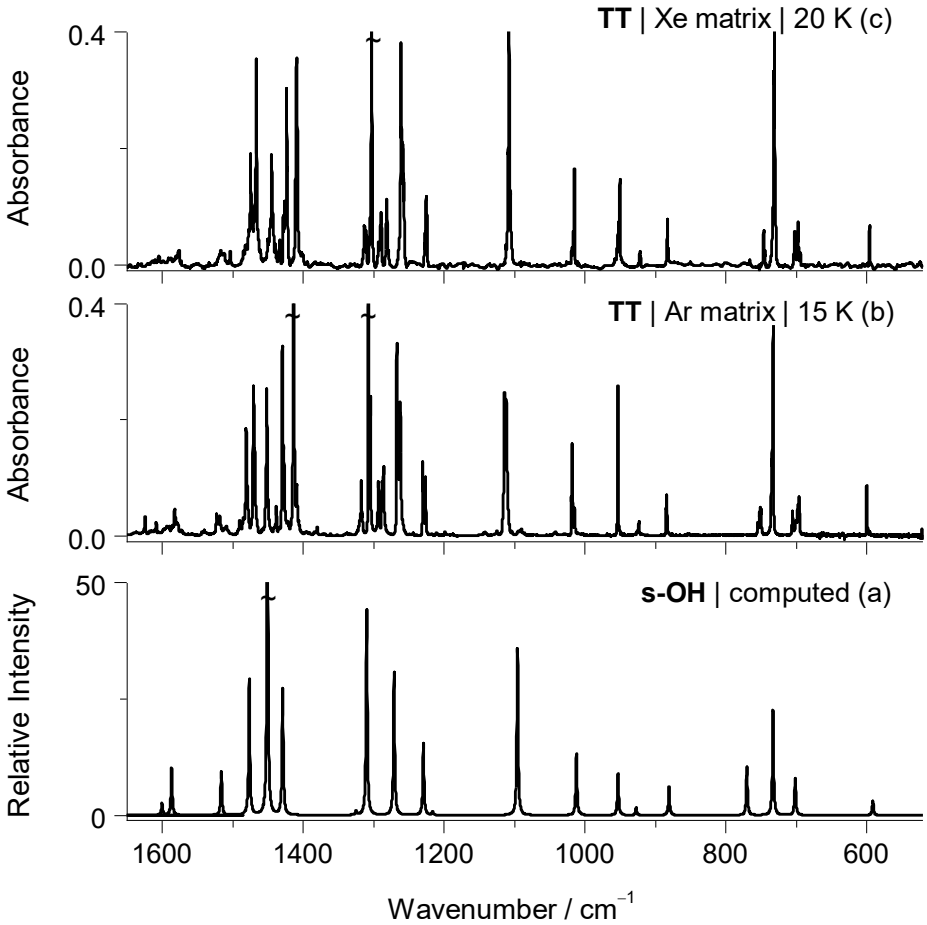

Figure S1. (a) B3LYP/6-311+G(2d,p) computed IR spectrum of the **s-OH** form of thiotropolone (**TT**). Experimental mid-IR spectra of **TT**: (b) monomers in argon matrix deposited at 15 K; (c) monomers in xenon matrix deposited at 20 K.

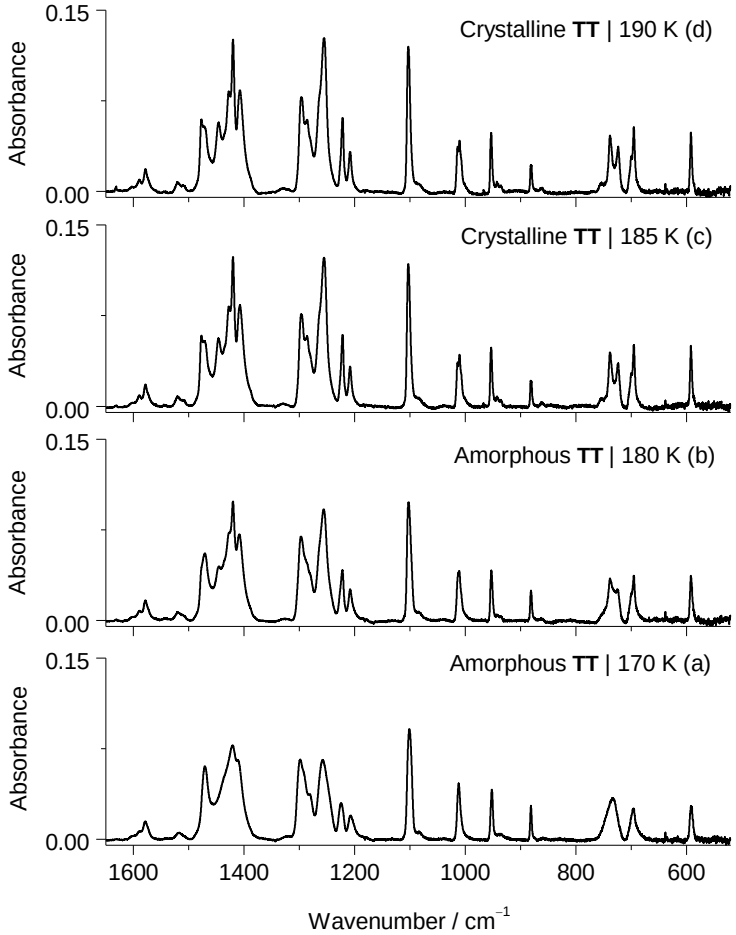

Figure S2. Experimental IR spectra of neat solid thiotropolone (**TT**) deposited at 15 K and annealed up to: (a) 170 K; (b) 180 K; (c) 185 K; (d) 190 K. The spectra were selected to display the temperature range where the thermally induced crystallization of **TT** occurred.

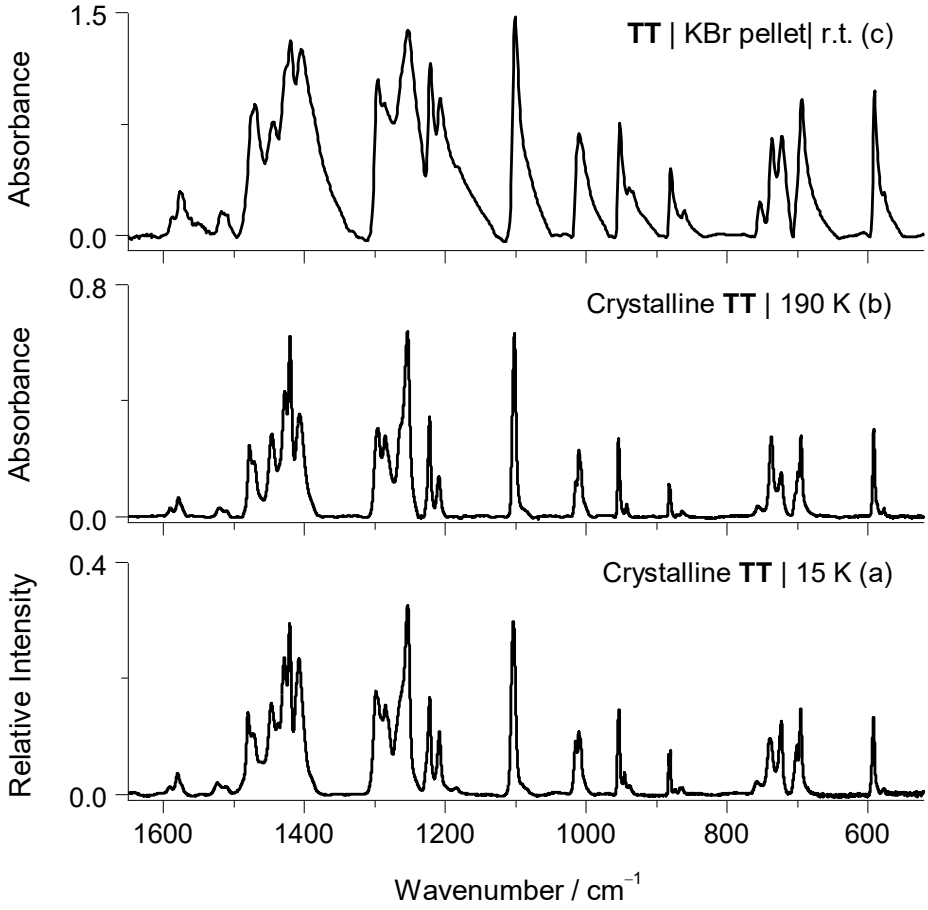

Figure S3. Experimental IR spectra of the neat solid of thiotropolone (**TT**) acquired from: (a) crystalline solid obtained after the sample has been deposited at 15 K, annealed up to 190 K, and cooled again to 15 K; (b) crystalline solid of **TT** after the sample has been deposited at 190 K; (c) solid sample of **TT** in a KBr pellet at room temperature (r.t.).

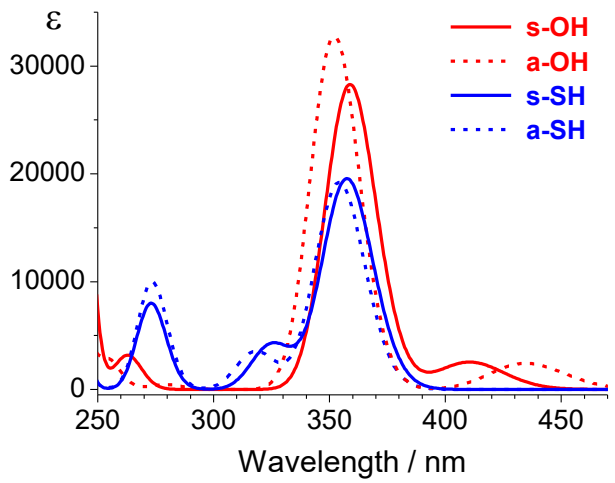

Figure S4. Simulated UV-Vis absorption spectra of both tautomers of thiotropolone, thione-enol (red) and thiol-keto (blue), based on the TD-DFT computations at the B3LYP/6-311+G(2d,p) level (see also Table S1). Solid lines correspond to the two *syn* forms (**s-OH** and **s-SH**) of each tautomeric stututure and dashed lines correspond to the two *anti* forms (**a-OH** and **a-SH**).

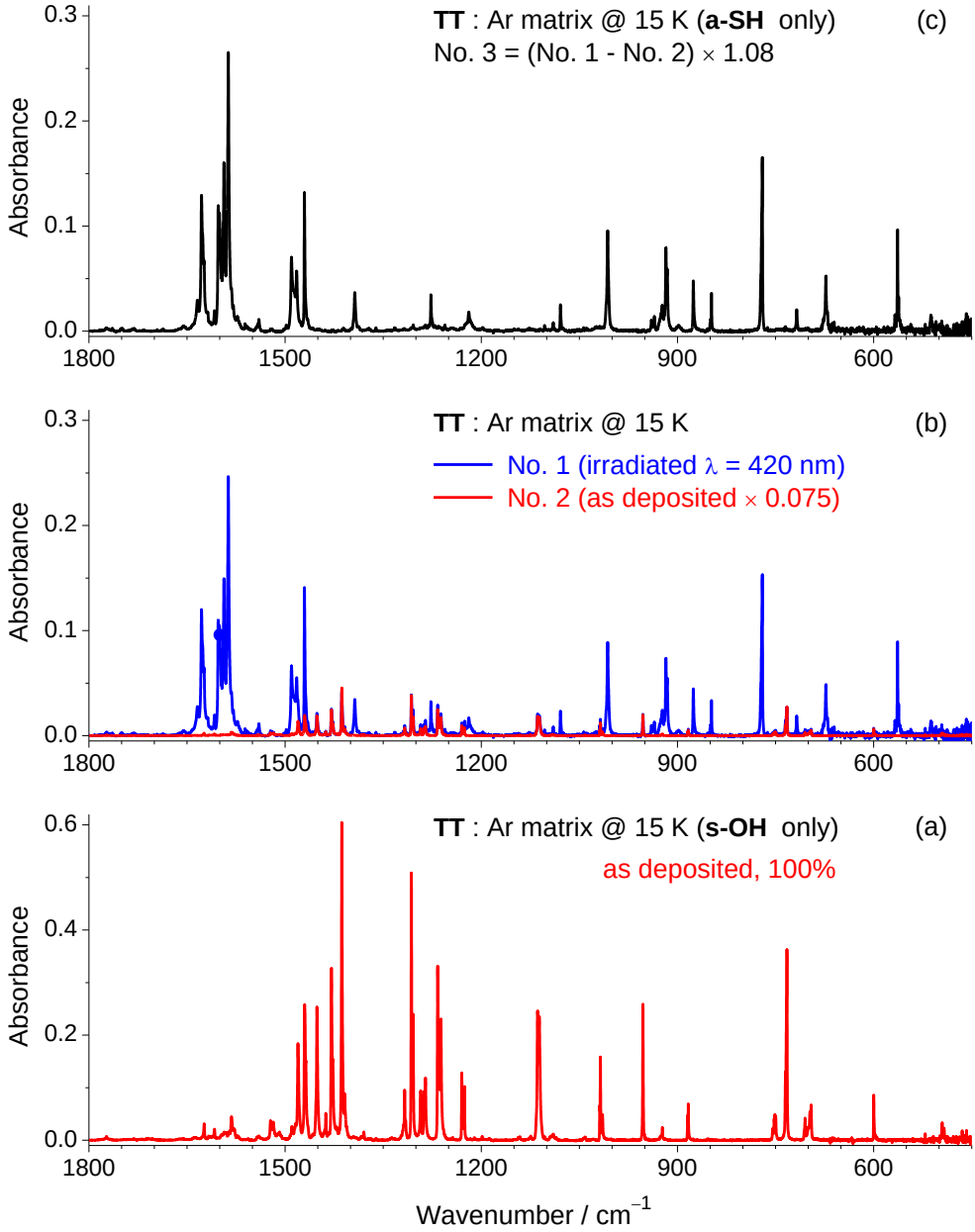

Figure S5. Experimental IR spectra of thiotropolone (**TT**) monomers isolated in an argon matrix at 15 K: (a) as deposited (**s-OH** form only), the same as in Figure 1b; (b) spectrum No.1 (blue) – after irradiation with visible light (λ = 420 nm, 20 mW, 2 min); No.2 (red) – the same as above, in frame S5a, but with intensity scaled by 0.075, to match the bands of non-reacted **s-OH** form remaining in the sample after the irradiation; (c) spectrum No. 3 (black) where the contribution of non-reacted **s-OH** was nullified, and the resulting spectrum scaled up, to obtain the amount of photoproduct **a-SH** equimolar to the amount of reactant **s-OH** before the irradiation.

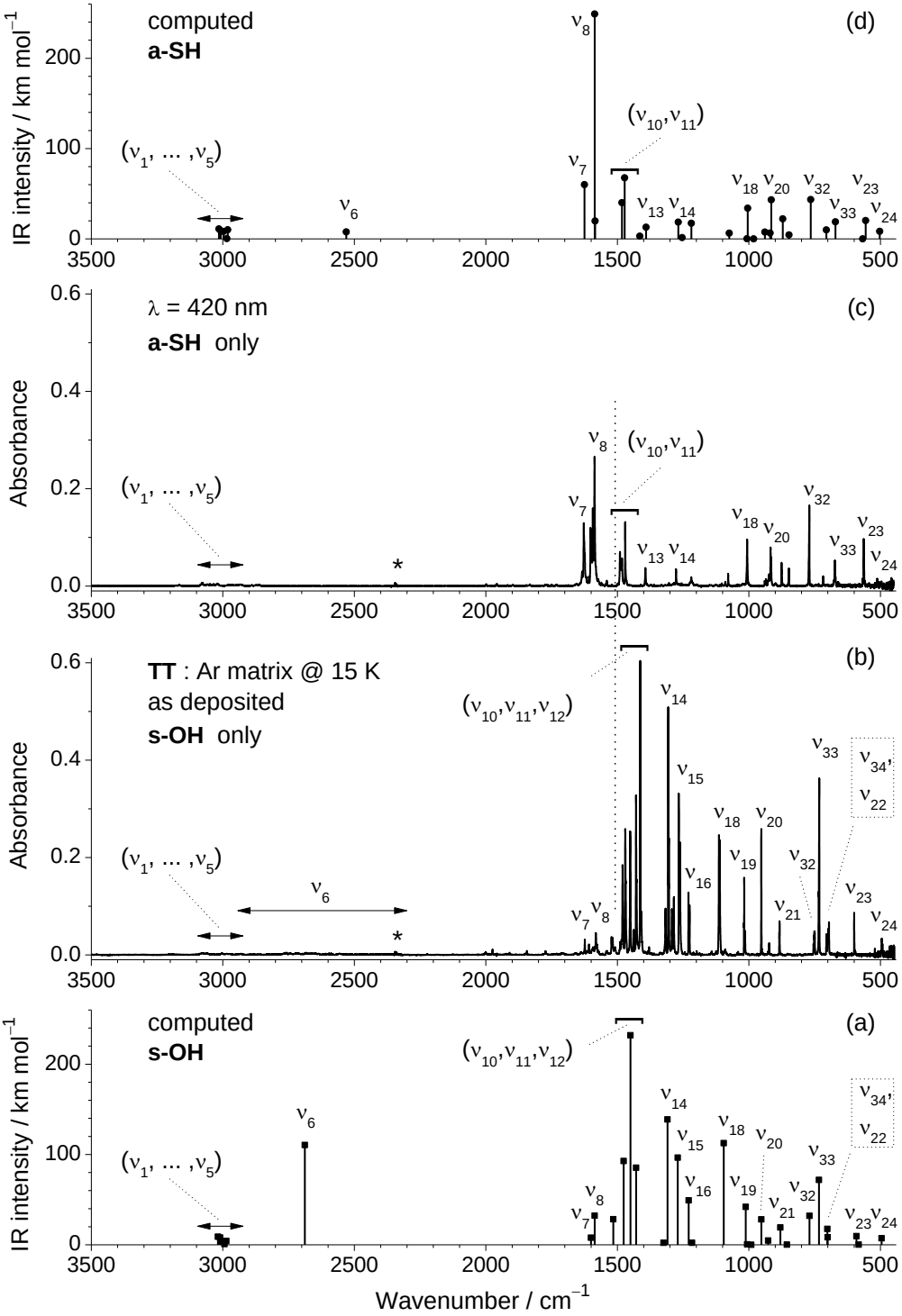

Figure S6. IR spectra of thiotropolone (**TT**) monomers computed at the B3LYP/6-311+G(2d,p) level of theory: (a) **s-OH**, and (d) **a-SH**; Experimental IR spectra of monomeric **TT** isolated in an argon matrix: (b) **s-OH** form only, and (c) **a-SH** form only (extracted as explained in Figure S5). Note that ordinate scales within pairs of frames (a,d) and (b,c) are intentionally equal. See Tables S2-S3 and S5-S6 for the mode numbering and vibrational assignment. Asterisks in frames (b,c) designate the band due to traces of atmospheric CO_2 (the same band as in Figure S7 where this range is expanded).

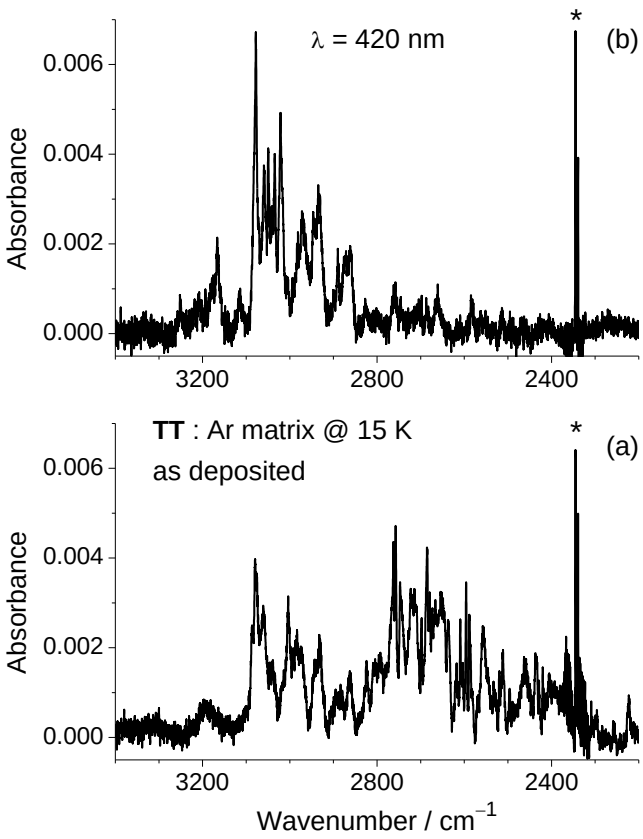

Figure S7. Experimental IR spectra of thiotropolone (**TT**) monomers isolated in an argon matrix at 15 K: (a) as deposited (**s-OH** form only), the same as in Figure S6b; (b) after irradiation with visible light (λ = 420 nm, 20 mW, 2 min). The band marked with asterisk is due to the traces of atmospheric CO_2 (same as in Figures S6b and S6c).

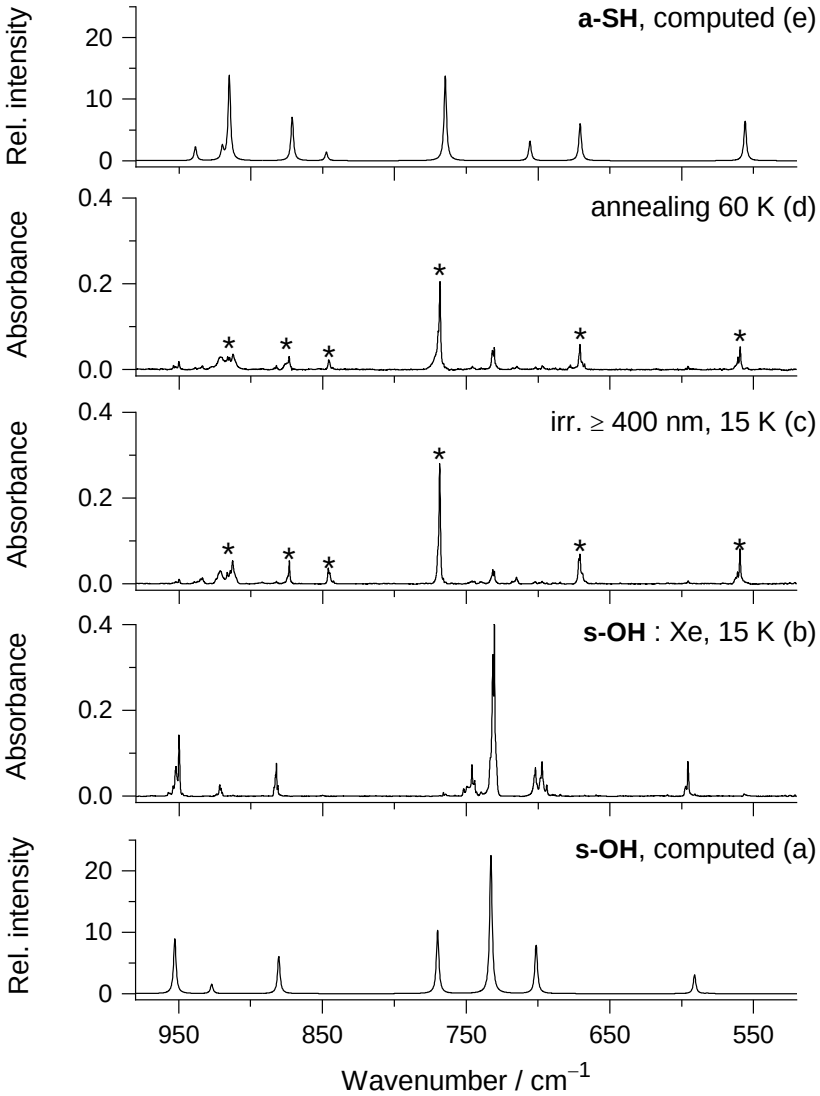

Figure S8. B3LYP/6-311+G(2d,p) computed IR spectra of (a) **s-OH** and (e) **a-SH** tautomers. Selected region of experimental mid-IR spectra of (b) thiotropolone **s-OH** freshly deposited in a Xe matrix at 15 K; (c) after subsequent irradiation with $\lambda \geq 400$ nm; and (d) after subsequent annealing to 60 K. Asterisks indicate bands of thiotropolone **a-SH**.

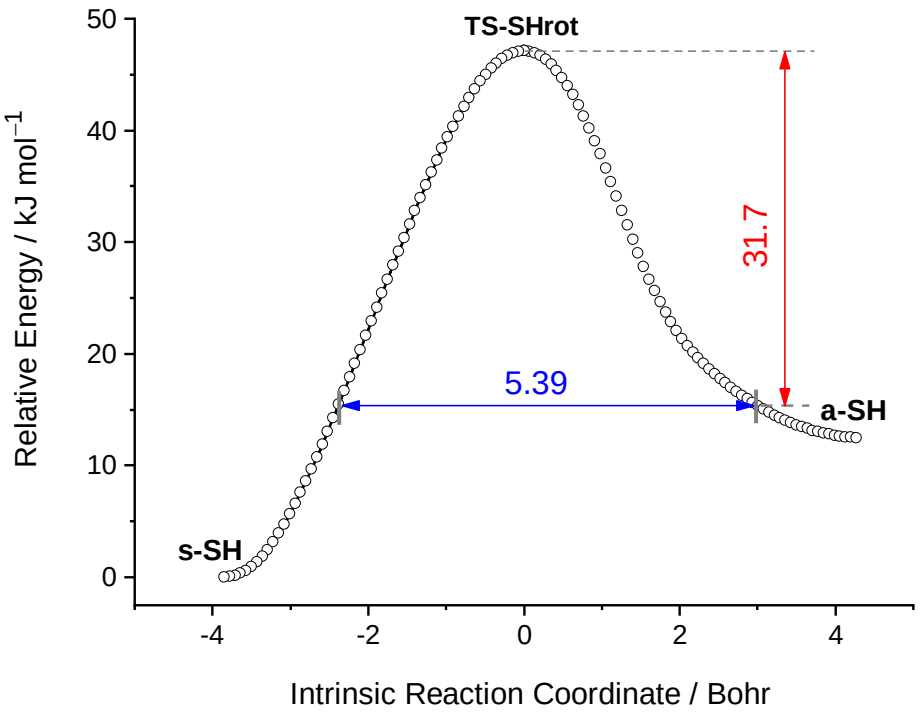

Figure S9. Relative electronic energy as a function of intrinsic reaction coordinate (IRC) for SH-rotamerization of **a-SH** to **s-SH** computed at the B3LYP/6-311+G(2d,p) level in non-mass-weighted (Cartesian) coordinates. The vertical arrow designates the calculated ZPE-corrected energy of the reactant **a-SH** relative to the transition state **TS-SHrot**. The horizontal arrow designates the barrier width considering the ZPE-corrected energy values of the stationary points superimposed with the pure electronic IRC energy profile.

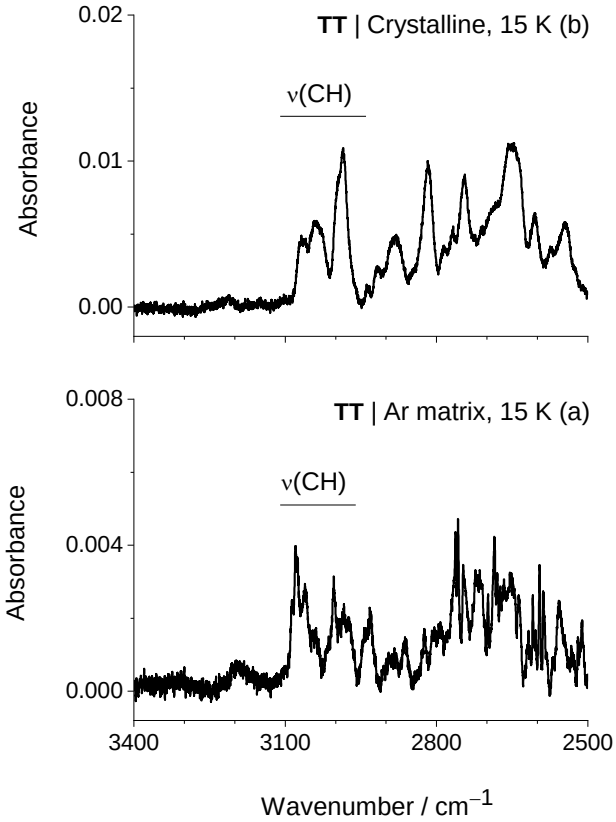

Figure S10. Selected region of the experimental IR spectra of **TT**: (a) monomeric compound deposited in an argon matrix at 15 K; (b) neat compound at 15 K (crystalline solid). As indicated in the graphical part of the figure by horizontal lines, the IR bands due to ν(CH) stretching modes should appear in the region from 3100 to 2950 cm^{-1}. The absorptions in the 2950−2500 cm^{-1} range should be due to the ν(OH) stretching mode.

3. Tables

Table S1. Wavelengths (WL / nm) and oscillator strengths (*f*) of the low-energy electronic excited singlet states computed at the B3LYP/6-311+G(2d,p) level using the time-dependent density functional theory (TD-DFT) for relevant species within the scope of this work.

a-OH		
WL	*f*	Sym.
624.94	0.0000	A"
532.57	0.0000	A"
434.95	0.0223	A'
352.03	0.3014	A'
279.69	0.0041	A'
267.15	0.0004	A"
254.48	0.0224	A'
250.99	0.0044	A'
240.87	0.0003	A"
236.32	0.3960	A'
233.63	0.0282	A'
222.63	0.0006	A"

a-SH		
WL	*f*	Sym.
354.18	0.1766	A'
345.80	0.0000	A"
323.61	0.0000	A"
318.27	0.0325	A'
273.44	0.0918	A'
249.55	0.0012	A"
235.28	0.3121	A'
222.55	0.0000	A"
216.23	0.0114	A"
209.14	0.0304	A'
203.89	0.0024	A"
202.72	0.0000	A"

s-OH		
WL	*f*	Sym.
458.94	0.0000	A"
410.56	0.0233	A'
407.71	0.0000	A"
358.89	0.2602	A'
262.91	0.0292	A'
243.35	0.0019	A"
240.09	0.4340	A'
224.80	0.0078	A'
217.39	0.0007	A"
213.35	0.0101	A"
207.93	0.0080	A"
207.18	0.0097	A'

s-SH		
WL	*f*	Sym.
357.56	0.1797	A'
328.18	0.0000	A"
325.33	0.0389	A'
310.64	0.0000	A"
273.09	0.0736	A'
243.10	0.0004	A"
235.78	0.3358	A'
221.28	0.0028	A"
211.05	0.0194	A"
209.96	0.0002	A"
205.49	0.0000	A"
199.39	0.2093	A'

Table S2. Vibrational modes of the **s-OH** form of thiotropolone computed at the B3LYP/6-311+G(2d,p) level of theory in harmonic approximation, and vibrational assignment.

Mode	Weight distribution (%) of most prominent internal coordinates [a,b]	Total (%)	Total (%)	Approximate Description
	A' symmetry	**Bond**	**Angle**	
S_1	rC3H11 (12.6) + rC4H12 (19.7) + rC5H13 (**32.1**) + rC6H14 (15.0) + rC7H15 (12.4)	97.7	2.3	ν_a(CH)
S_2	rC3H11 (21.6) + rC4H12 (15.6) − rC6H14 (16.2) − rC7H15 (**36.6**)	97.5	2.5	ν_b(CH)
S_3	rC3H11 (**38.8**) + rC4H12 (6.8) − rC5H13 (29.0) + rC7H15 (24.6)	100.0	0.0	ν_c(CH)
S_4	rC3H11 (20.8) − rC4H12 (**35.8**) + rC5H13 (9.5) + rC6H14 (17.1) − rC7H15 (9.9)	96.7	3.3	ν_d(CH)
S_5	rC3H11 (6.6) − rC4H12 (15.3) + rC5H13 (17.8) − rC6H14 (**40.6**) + rC7H15 (14.6)	98.3	1.7	ν_e(CH)
S_6	rO10H9 (**64.9**) + rC2O10 (5.7) + βC2O10H9 (9.3)	82.6	17.4	ν(OH)
S_7	rC2C3 (9.0) + rC3C4 (5.8) − rC4C5 (**21.5**) + rC6C7 (13.2) − rC7C1 (5.1) − βC3C4H12 (5.8) − βC6C5H13 (5.5)	68.1	31.9	ν_a(CC)
S_8	rC2C3 (**17.5**) − rC3C4 (14.1) + rC5C6 (13.6) − rC6C7 (**16.2**) − βC2C3H11 (5.2)	73.1	26.9	ν_b(CC)
S_9	rC7C1 (**11.9**) − rC1C2 (8.3) + rC2C3 (6.8) + rC3C4 (7.0) − rC5C6 (5.5) − rC6C7 (7.3) − βC2O10H9 (**10.3**) − βC4C5H13 (7.0)	53.6	46.4	δ(COH) −ν_b(CC)
S_{10}	− rC7C1 (5.3) − rC2C3 (9.5) + rC3C4 (**11.1**) − rC4C5 (8.5) + rC5C6 (**12.2**) − rC6C7 (8.3) + βC2C3H11 (8.4) − βC5C6H14 (6.0) − βC2O10H9 (5.2)	59.9	40.1	ν_c(CC) + δ_a(CH)
S_{11}	rC1C2 (10.1) + rC2C3 (6.8) − rC4C5 (**12.4**) − rC6C7 (11.6) + rC2O10 (5.6) + βC2O10H9 (**10.9**) − βC1C7H15 (8.5) + βC5C4H12 (8.2) + βC4C3H11 (6.1)	57.4	42.6	δ_b(CH) + δ(COH) +ν_c(CC)
S_{12}	βC5C4H12 (5.0) − βC4C5H13 (**11.5**) − βC5C6H14 (**11.4**) − βC6C7H15 (9.8) + βC1C2O10 (5.1) − rC7C1 (8.4) + rC2C3 (6.2) + rC4C5 (7.9) + rC6C7 (6.6)	35.6	64.4	δ_c(CH)
S_{13}	− rC7C1 (**12.9**) + rC1C2 (**12.9**) + rC3C4 (5.9) − rC6C7 (8.9) − rC2O10 (**11.0**) − βC2O10H9 (**10.5**) − βC1C7H15 (6.7)	58.3	41.7	ν_d(CC) − ν(CO) − δ(COH)
S_{14}	rC2O10 (**24.1**) − rC7C1 (6.0) − rC2C3 (5.0) − rC3C4 (8.1) + rC6C7 (6.0) + βC4C3H11 (5.0) − βC3C4H12 (6.4) + βC7C6H14 (5.9)	60.6	39.4	ν(CO)
S_{15}	βC2C3H11 (10.5) − βC1C7H15 (6.6) + βC2O10H9 (6.8) + βC1C2O10 (6.3) − rC7C1 (10.2) + rC2C3 (**16.6**) − rC3C4 (5.9) + rC6C7 (9.0)	48.3	51.7	δ_d(CH)
S_{16}	− rC2O10 (**16.3**) + rC7C1 (10.9) − rC2C3 (5.1) + rC3C4 (5.0) + rC4C5 (9.8) − rC5C6 (11.5) + βC4C5H13 (6.9) + βC7C6H14 (7.3)	67.4	32.6	ν(CO) + ν_d(CC)
S_{17}	rC6C7 (**13.5**) + rC7C1 (7.6) − rC1C2 (**12.2**) + rC3C4 (10.4) − rC4C5 (11.0) − rC5C6 (5.6) + βC4C3H11 (5.3) − βC5C4H12 (6.4) − βC5C6H14 (8.6)	65.6	34.4	ν_e(CC) + δ_e(CH)
S_{18}	rC6C7 (**12.8**) + rC7C1 (7.9) + rC1C2 (5.3) − rC3C4 (**12.1**) − rC4C5 (10.4) + rC5C6 (5.0) − rC1S8 (**12.1**) − βC1C2O10 (5.6) − βC4C5H13 (5.6)	73.0	27.0	ν_f(CC) − ν(CS)
S_{19}	rC1C2 (5.5) + rC2C3 (**11.4**) + rC3C4 (9.3) − rC5C6 (**10.3**) − rC6C7 (7.1) + rC2O10 (6.0) − rC1S8 (**10.7**) + βC1C7C6 (7.1) − βC2C3C4 (5.4)	65.5	34.5	ν_b(CC) − ν(CS)
S_{20}	− rC3C4 (9.2) − rC4C5 (**16.1**) − rC5C6 (**16.9**) − rC6C7 (10.0) + rC1S8 (7.1) − βC1C2C3 (5.9)	69.0	31.0	ν_g(CC)
S_{21}	− βC2C3C4 (9.8) − βC4C5C6 (**21.0**) − βC1C7C6 (7.6) + rC1C2 (14.7) + rC4C5 (5.8) + rC5C6 (7.2)	43.1	56.9	δ_a(ring)
S_{22}	− rC2O10 (**14.9**) − rC7C1 (5.9) − rC1C2 (12.1) − rC2C3 (13.7) − rC3C4 (10.0) + βC1C7C6 (6.8) − βC7C1C2 (5.1)	68.5	31.5	ν_g(CC) + δ_b(ring)
S_{23}	− rC1S8 (**20.3**) − rC7C1 (14.1) − rC1C2 (16.0) − rC2C3 (8.0) − rC4C5 (5.3) − rC6C7 (5.5) + βC2C3C4 (7.0) + βC5C6C7 (6.4)	77.3	22.7	ν(CS) − ν_g(CC)
S_{24}	− βC1C2O10 (**18.4**) + βC3C2O10 (10.1) + βC5C6C7 (7.7) + βC1C7C6 (5.9) − rC7C1 (10.1) − rC1C2 (8.5) + rC2C3 (14.3) + rC3C4 (7.5)	46.8	53.2	δ(CCO)
S_{25}	βC1C7C6 (**10.5**) − βC1C2C3 (8.0) + βC2C3C4 (5.5) + βC3C4C5 (5.9) − βC4C5C6 (7.2) + βC7C1S8 (5.1) + rC7C1 (**9.8**) − rC1C2 (7.8) + rC3C4 (8.0) + rC6C7 (8.0) + rC2O10 (8.1)	49.4	50.6	δ_c(ring)
S_{26}	rC1S8 (**15.0**) + rC1C2 (10.1) + rC2C3 (6.3) − rC4C5 (4.9) + βC2C1S8 (**13.3**) − βC3C2O10 (12.2) + βC2C3C4 (11.2) + βC5C6C7 (9.1) + βC1C7C6 (7.1)	44.0	56.0	δ_d(ring)
S_{27}	− βC7C1S8 (**20.4**) + βC2C1S8 (6.9) + βC1C7C6 (9.8) + βC1C2O10 (9.1) − βC1C2C3 (7.0) + rC1C2 (11.5) + rC2O10 (7.1) − rC1S8 (6.2) − rC6C7 (5.6)	38.8	61.2	δ(CCS)

	A'' symmetry	Tors.	Out	
S_{28}	τH14C6C7H15 (**15.7**) + τC2C3C4C5 (6.9) − τC3C4C5C6 (**28.0**) + τC4C5C6C7 (5.4) + τC6C7C1C2 (4.8) − τC7C1C2C3 (**24.7**)	94.3	5.7	γ_a(CH)
S_{29}	τC1C2C3C4 (**27.7**) − τC4C5C6C7 (6.1) + τC5C6C7C1 (19.2) − τC7C1C2C3 (17.8) − τC1C2C3H11 (8.0) − τH12C4C5H13 (9.8) − τH12C4C5C6 (5.7)	99.2	0.8	γ_b(CH)
S_{30}	− τC3C4C5C6 (8.7) + τC4C5C6C7 (8.7) − τC6C7C1C2 (**15.5**) − τH11C3C4C5 (12.4) + τC5C6C7H15 (12.1) + τS8C1C2C3 (11.4) − τC3C4C5H13 (6.0)	95.6	4.4	γ_c(CH)
S_{31}	− τC2C3C4C5 (11.8) + τC3C4C5C6 (11.8) + τC4C5C6C7 (**15.4**) − τC5C6C7C1 (6.9) − τC7C1C2C3 (8.4) − τC1C7C6H14 (11.1) − τC2C3C4H12 (8.6) − τS8C1C7C6 (5.2)	91.1	8.9	γ_d(CH)
S_{32}	γC1C2C3O10 (**20.9**) − τC1C2O10H9 (**11.9**) − τC3C2O10H9 (**11.0**) − τC7C1C2C3 (6.7) + τC1C2C3C4 (6.1) − τC2C3C4H12 (19.6) + γC3C4C5H12 (15.3)	61.1	38.9	τOH
S_{33}	γC4C5C6H13 (**19.7**) + γC5C6C7H14 (6.7) + γC3C4C5H12 (5.9) + τC1C2C3C4 (5.8) + τH13C5C6C7 (9.7) + τC2C3C4C5 (16.3) − τC6C7C1C2 (7.4) − τS8C1C7C6 (5.0) + τO10C2C3C4 (7.4)	60.4	39.6	γ_e(CH)
S_{34}	τC5C6C7C1 (**20.7**) − τC6C7C1C2 (13.1) − τC1C2C3C4 (12.1) + τC2C3C4C5 (**19.0**) − τC4C5C6C7 (6.8) + τS8C1C7C6 (5.2)	92.4	7.6	τ_a(ring)
S_{35}	τC5C6C7C1 (**14.7**) + τC1C2C3C4 (8.3) − τC2C3C4C5 (12.2) + τC3C4C5C6 (**16.6**) − τC4C5C6C7 (**17.3**) − τS8C1C7C6 (6.2)	91.1	8.9	τ_b(ring)
S_{36}	τC7C1C2C3 (9.0) − τC1C2C3C4 (14.0) − τC2C3C4H12 (**22.2**) + τH12C4C5C6 (7.7) + γC3C4C5H12 (**24.7**) + γC1C2C3O10 (5.7)	64.1	35.9	τ_c(ring)
S_{37}	γC5C6C7H14 (**27.1**) + τC1C7C6H14 (**26.6**) + τC6C7C1C2 (9.7) − τC7C1C2C3 (7.2) − τC4C5C6H14 (7.1) − τS8C1C2C3 (5.7)	66.5	33.5	τ_d(ring)
S_{38}	γC1C2C3O10 (**19.3**) − γC2C1C7S8 (**11.8**) − τC7C1C2O10 (**15.8**) +τS8C1C2C3(**12.7**) +τC5C6C7C1 (10.0) − τO10C2C3H11 (7.6) − τC3C4C5C6 (5.6) −τH11C3C4C5(5.5)	66.7	33.3	γ(CO) − γ(CS)
S_{39}	τS8C1C2O10 (**25.2**) + γC2C1C7S8 (**18.1**) − τC4C5C6C7 (17.6) + τC2C3C4C5 (8.8) − τC3C4C5C6 (7.3)	79.5	20.5	γ(CS) + γ(CO)

[a] See Scheme S1 for the atom numbering. Internal coordinates used in the analysis of vibrational modes are defined automatically, as described in ref. S4.
[b] All contributions of most prominent internal coordinates, with weights of 5% or higher, are included. The top contributions are shown in bold. Abbreviations: ν = stretching, δ = in-plane bending, γ = out-of-plane bending, τ = torsion; $r_{i,j}$ is the distance between atoms A_i and A_j; $\beta_{i,j,k}$ is the angle between vectors A_kA_i and A_kA_j; $\tau_{i,j,k,l}$ is the dihedral angle between the plane defined by A_i, A_j, A_k and the plane defined by A_j, A_k and A_l atoms; $\gamma_{i,j,k,l}$ is the angle between the vector A_kA_i and the plane defined by atoms A_j, A_k, A_l. The symbols (+) and (−) denote in-phase and in-opposite-phase couplings between coordinates of different types.

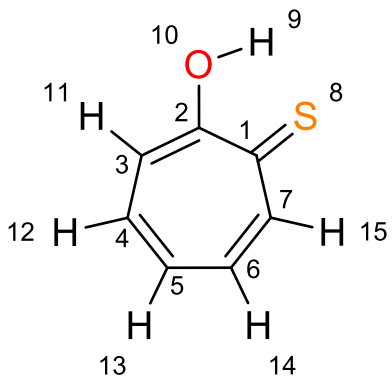

Scheme S1. Structure and the atom numbering of the **s-OH** form of thiotropolone.

Table S3. Experimental IR spectra of s-**OH** form of **TT** isolated in an Ar matrix at 15 K, and in neat **TT** crystals at 15 K, compared with harmonic and anharmonic wavenumbers ($\tilde{\nu}$ / cm^{-1}) and infrared intensities (I / km mol^{-1}) computed at the B3LYP/6-311+G(2d,p) level of theory, and vibrational assignment.

Mode	Ar matrix [a]		Crystal[a]	Calc.[b]				Sym.	Approximate
Nº.	$\tilde{\nu}_{exp}$	I_{exp}	$\tilde{\nu}_{exp}$	$\tilde{\nu}_{harm}$	I_{harm}	$\tilde{\nu}_{anhar}$	I_{anhar}		Description[c]
	A' symmetry								
$\nu_8+\nu_{10}$						3091.9	6.4	A'	
$\nu_7+\nu_{10}$						3075.8	5.6	A'	
ν_1	-	-		3018.4	8.9	3050.7	18.0	A'	ν_a(CH)
ν_2	-	-		3010.7	8.1	2991.9	15.7	A'	ν_b(CH)
ν_3	-	-		3007.4	3.8	3047.1	12.4	A'	ν_c(CH)
ν_4	-	-		2994.0	0.7	3037.8	2.4	A'	ν_d(CH)
ν_5	-	-		2986.9	4.3	3001.8	38.6	A'	ν_e(CH)
$\nu_8+\nu_{12}$						2995.6	5.4	A'	
$\nu_7+\nu_{12}$						2987.5	10.5	A'	
$\nu_9+\nu_{10}$						2983.2	13.7	A'	
ν_6				2961.8	200.3	2688.1	110.5	A'	ν(OH)
$\nu_{31}+\nu_{33}$						1613.8	5.4	A'	
$\nu_{19}+\nu_{23}$						1613.5	11.9	A'	
$\nu_{18}+\nu_{24}$						1603.8	11.2	A'	
ν_7	~1600 ov. [d]		1590	1602.0	7.9	1595.9	2.2	A'	ν_a(C=C)
$\nu_{21}+\nu_{22}$						1588.2	8.6	A'	
ν_8	1581.9	24.1	1579	1588.0	32.3	1582.5	0.4	A'	ν_b(C=C)
$2\times\nu_{32}$						1571.6	54.3	A'	$2\times\tau$OH
$\nu_{32}+\nu_{34}$						1551.7	51.6	A'	
$\nu_{32}+\nu_{33}$						1528.4	19.0	A'	
$\nu_{19}+\nu_{24}$						1520.0	7.4	A'	
ν_9	**1522.4**, 1518.2	20.5	**1523**, 1511	1517.4	28.3	1504.5	26.1	A'	δ(COH) $-\nu_b$(C=C)
$\nu_{31}+\nu_{35}$						1488.9	21.0	A'	
ν_{10}	1480.3	56.9	1479	1477.5	92.7	1477.1	40.7	A'	ν_c(C=C) + δ_a(CH)
$\nu_{21}+\nu_{23}$	1470.1	78.7	1471			1478.9	12.2	A'	
ν_{11}	1451.3	64.5	1447	1451.8	232.1	1425.5	132.3	A'	δ_b(CH) + δ(COH)
	1437.7	11.7	1436						
ν_{12}	1429.1	93.3	1428, **1421**	1430.3	85.3	1426.3	121.5	A'	δ_c(CH)
	1413.3	126.7	1408						
$\nu_{34}+\nu_{35}$						1388.8	9.8	A'	
$\nu_{30}+\nu_{36}$	1317.1	23.4				1332.9	28.0	A'	
ν_{13}				1325.6	2.2	1307.0	4.8	A'	ν_d(CC) $-\nu$(CO) $-\delta$(COH)
ν_{14}	**1306.8**, 1285.4	154.6	**1298**, 1285	1310.7	138.7	1314.6	91.3	A'	ν(C–O)
ν_{15}	**1266.7**, 1261.8	113.3	1253	1271.6	96.5	1272.6	98.7	A'	δ_d(CH)
$\nu_{20}+\nu_{27}$						1266.5	6.8	A'	
ν_{16}	**1229.8**, 1225.7	30.2	1222	1230.3	49.2	1234.2	42.3	A'	ν(CO) + ν_d(CC)
ν_{17}	-	-	1208	1217.1	2.2	1218.4	10.5	A'	ν_e(CC) + δ_e(CH)
$\nu_{30}+\nu_{38}$						1104.3	5.5	A'	
ν_{18}	**1113.9**, 1111.3	105.9	1103	1097.0	112.6	1101.2	88.4	A'	ν_f(CC) $-\nu$(CS)
$\nu_{23}+\nu_{24}$						1093.7	8.1	A'	
ν_{19}	**1017.9**, 1014.7	27.5	1014, **1010**	1013.0	42.0	1017.0	24.0	A'	ν_b(CC) $-\nu$(CS)
$\nu_{23}+\nu_{25}$						1014.1	11.2	A'	
ν_{20}	952.8	27.0	**953**, 945	953.8	28.1	956.1	22.2	A'	ν_g(CC)
ν_{21}	884.4, **883.5**	10.8	882, 880	881.4	19.2	884.5	19.2	A'	δ_a(ring)
ν_{22}	697.4, **695.6**	23.8	695	702.2	17.6	705.6	15.7	A'	ν_g(CC) + δ_b(ring)
ν_{23}	599.8	10.1	592	591.9	9.7	594.8	8.9	A'	ν(CS) $-\nu_g$(CC)
ν_{24}	**495.2**, 492.4	8.9	498, 491	495.9	7.3	498.1	6.4	A'	δ(CCO)
ν_{25}	-	-		417.0	1.3	420.6	1.5	A'	δ_c(ring)
ν_{26}	-	-		334.9	6.6	336.4	7.5	A'	δ_d(ring)
ν_{27}	-	-		308.8	1.7	311.2	1.7	A'	δ(CCS)

	A'' symmetry								
ν_{28}	-	-		1007.7	0.5	1015.5	0.3	A"	γ_a(CH)
ν_{29}	-	-		992.0	0.05	1001.5	0.2	A"	γ_b(CH)
ν_{30}	925.4, **923.1**	4.7	937	927.7	4.8	934.5	5.0	A"	γ_c(CH)
ν_{31}	**854.1**, 851.9	0.7	866, 864	856.2	0.2	874.8	6.4	A"	γ_d(CH)
ν_{32}	754.2, **751.0**	17.9	757	770.4	32.1	825.2	26.2	A"	τOH
ν_{33}	734.8, **732.6**	71.4	738, 723	734.2	71.8	748.2	12.5	A"	γ_e(CH)
ν_{34}	704.9	6.6	701	701.5	8.3	713.6	62.3	A"	τ_a(ring)
ν_{35}	-	-	577	582.9	0.2	617.3	0.1	A"	τ_b(ring)
ν_{36}	-	-		391.1	2.3	398.0	3.5	A"	τ_c(ring)
ν_{37}	-	-		339.2	0.8	347.9	1.9	A"	τ_d(ring)
ν_{38}	-	-		166.8	0.02	171.1	0.003	A"	γ(CO) − γ(CS)
ν_{39}	-	-		92.7	0.1	97.5	0.2	A"	γ(CS) + γ(CO)

[a] Experimental intensities (*I*) were normalized in such a way that the sum of integrated experimental intensities in the 1590-480 cm^{-1} frequency range would be equal to the sum of the corresponding harmonic infrared intensities (A^{th}, in km mol^{-1}) of the two arrays [$\Sigma(\nu_8{:}\nu_{24}) + \Sigma(\nu_{30}{:}\nu_{34})$] computed at the B3LYP/6-311+G(2d,p) level of theory. For the split bands observed experimentally, the wavenumbers corresponding to the more intense component are shown in bold. The bands of the polycrystalline sample are designated as "crystal", for brevity.

[b] Computed harmonic wavenumbers were multiplied by 0.950 (above 2800 cm^{-1}) or 0.980 (below 2000 cm^{-1}) and are expressed in cm^{-1}. Computed anharmonic wavenumbers and intensities are not scaled. The anharmonic section includes all fundamental modes, as well as the overtones and combination bands with computed anharmonic infrared intensities over 5 km mol^{-1}.

[c] Approximate descriptions are based on visualization of normal vibrations (using the Chemcraft software[S5]), and also on the Vibrational Mode Automatic Relevance Determination (VMARD) analysis using Bayesian regression, as defined by Teixeira and Cordeiro.[S4] The most prominent internal coordinates, obtained using the VMARD formalism, with weights above 5%, are listed in Table S2.

[d] The band ν_7 marked "ov." is predicted to appear near, and overlapped with the band due to monomeric H_2O in an Ar matrix.[S6]

Table S4. The molecular vibrations of **s-OH** computed at the B3LYP/6-311+G(2d,p) level in harmonic approximation subjected to the VMARD (Vibrational Mode Automatic Relevance Determination) analysis using Bayesian regression.

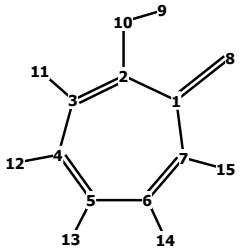	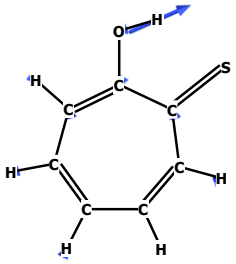
Structure of **s-OH** tautomer of **TT** and atom numbering: No. 1-7 - carbon, No. 8 - sulphur, No. 10 - oxygen, No. 9, 11-15 - hydrogen	Mode 6: (A') 2688.1 cm-1 (anharmonic) (IR: 200.3 km mol-1) **+1.0113 (64.9%) BOND H9 O10** +0.0885 (5.7%) BOND C2 O10 +0.1446 (9.3%) ANGLE C2 O10 H9
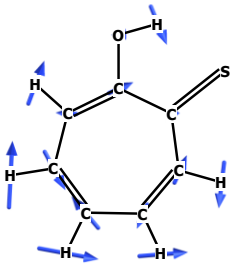	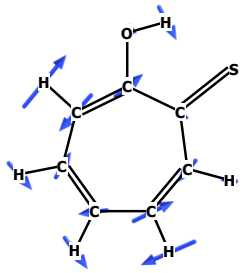
Mode 7: (A') 1600.38 cm-1 (IR: 7.9 km mol-1) -0.1227 (5.1%) BOND C1 C7 +0.2147 (9.0%) BOND C2 C3 +0.1401 (5.8%) BOND C3 C4 **-0.5138 (21.5%) BOND C4 C5** **+0.3150 (13.2%) BOND C6 C7** -0.1395 (5.8%) ANGLE C3 C4 H12 -0.1317 (5.5%) ANGLE C6 C5 H13	Mode 8: (A') 1586.43 cm-1 (IR: 32.3 km mol-1) **+0.3871 (17.5%) BOND C2 C3** -0.3111 (14.1%) BOND C3 C4 +0.3006 (13.6%) BOND C5 C6 **-0.3590 (16.2%) BOND C6 C7** -0.1155 (5.2%) ANGLE C2 C3 H11
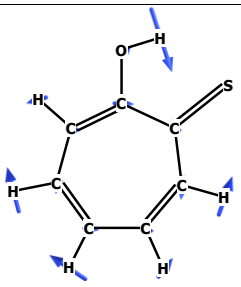	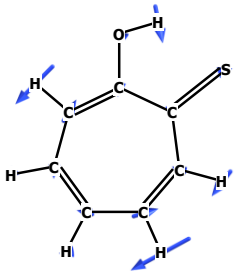
Mode 9: (A') 1515.85 cm-1 (IR: 28.3 km mol-1) **+0.3395 (11.9%) BOND C1 C7** -0.2372 (8.3%) BOND C1 C2 +0.1937 (6.8%) BOND C2 C3 +0.1998 (7.0%) BOND C3 C4 -0.1563 (5.5%) BOND C5 C6 -0.2087 (7.3%) BOND C6 C7 **-0.2938 (10.3%) ANGLE C2 O10 H9** -0.1985 (7.0%) ANGLE C4 C5 H13	Mode 10: (A') 1476.01 cm-1 (IR: 92.7 km mol-1) -0.1393 (5.3%) BOND C1 C7 -0.2506 (9.5%) BOND C2 C3 **+0.2941 (11.1%) BOND C3 C4** -0.2265 (8.5%) BOND C4 C5 **+0.3233 (12.2%) BOND C5 C6** -0.2200 (8.3%) BOND C6 C7 +0.2237 (8.4%) ANGLE C2 C3 H11 -0.1589 (6.0%) ANGLE C5 C6 H14 -0.1367 (5.2%) ANGLE C2 O10 H9

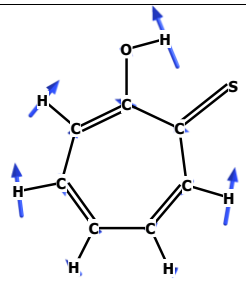

Mode 11: (A') 1450.31 cm-1
(IR: 232.1 km mol-1)
-0.1508 (5.6%) BOND C2 O10
+0.2712 (10.1%) BOND C1 C2
-0.1832 (6.8%) BOND C2 C3
-0.3332 (12.4%) BOND C4 C5
-0.3106 (11.6%) BOND C6 C7

+0.2937 (10.9%) ANGLE C2 O10 H9
+0.1640 (6.1%) ANGLE C4 C3 H11
+0.2208 (8.2%) ANGLE C5 C4 H12
-0.2284 (8.5%) ANGLE C1 C7 H15

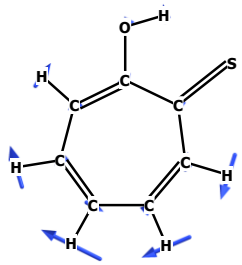

Mode 12: (A') 1428.84 cm-1
(IR: 85.3 km mol-1)
-0.2371 (8.4%) BOND C1 C7
+0.1747 (6.2%) BOND C2 C3
+0.2244 (7.9%) BOND C4 C5
+0.1869 (6.6%) BOND C6 C7

+0.1432 (5.1%) ANGLE C1 C2 O10
+0.1422 (5.0%) ANGLE C5 C4 H12
-0.3260 (11.5%) ANGLE C4 C5 H13
-0.3214 (11.4%) ANGLE C5 C6 H14
-0.2756 (9.8%) ANGLE C6 C7 H15

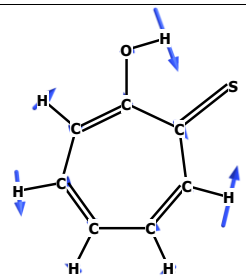

Mode 13: (A') 1324.28 cm-1
(IR: 2.2 km mol-1)
-0.4455 (12.9%) BOND C1 C7
+0.4463 (12.9%) BOND C1 C2
-0.3812 (11.0%) BOND C2 O10
+0.2027 (5.9%) BOND C3 C4
+0.3074 (8.9%) BOND C6 C7

-0.3635 (10.5%) ANGLE C2 O10 H9
-0.2332 (6.7%) ANGLE C1 C7 H15

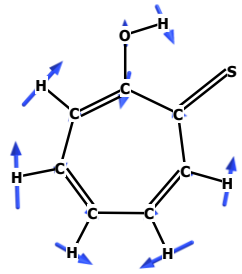

Mode 14: (A') 1309.35 cm-1
(IR: 138.7 km mol-1)
+0.7471 (24.1%) BOND C2 O10
-0.1846 (6.0%) BOND C1 C7
-0.2506 (8.1%) BOND C3 C4
+0.1870 (6.0%) BOND C6 C7

-0.1992 (6.4%) ANGLE C3 C4 H12
+0.1839 (5.9%) ANGLE C7 C6 H14

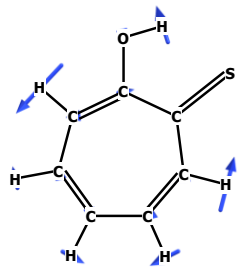

Mode 15: (A') 1270.31 cm-1
(IR: 96.5 km mol-1)
-0.4321 (10.2%) BOND C1 C7
+0.7058 (16.6%) BOND C2 C3
-0.2520 (5.9%) BOND C3 C4
+0.3841 (9.0%) BOND C6 C7

+0.2877 (6.8%) ANGLE C2 O10 H9
+0.2682 (6.3%) ANGLE C1 C2 O10
+0.4452 (10.5%) ANGLE C2 C3 H11
-0.2828 (6.6%) ANGLE C1 C7 H15

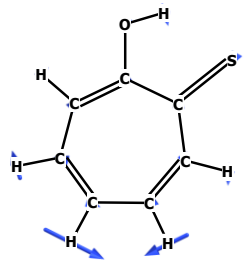

Mode 16: (A') 1229.03 cm-1
(IR: 49.2 km mol-1)
-0.7141 (16.3%) BOND C2 O10
+0.4780 (10.9%) BOND C1 C7
-0.2246 (5.1%) BOND C2 C3
+0.4298 (9.8%) BOND C4 C5
-0.5028 (11.5%) BOND C5 C6

+0.3021 (6.9%) ANGLE C4 C5 H13
+0.3175 (7.3%) ANGLE C7 C6 H14

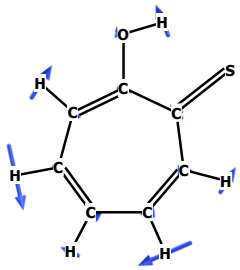

Mode 17: (A') 1215.89 cm-1
(IR: 2.2 km mol-1)
+0.3517 (7.6%) BOND C1 C7
-0.5618 (12.2%) BOND C1 C2
+0.4804 (10.4%) BOND C3 C4
-0.5070 (11.0%) BOND C4 C5
-0.2560 (5.6%) BOND C5 C6
+0.6198 (13.5%) BOND C6 C7

+0.2432 (5.3%) ANGLE C4 C3 H11
-0.2950 (6.4%) ANGLE C5 C4 H12
-0.3950 (8.6%) ANGLE C5 C6 H14

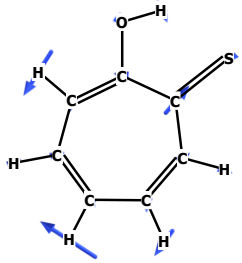

Mode 18: (A') 1095.84 cm-1
(IR: 112.6 km mol-1)
-0.4689 (12.1%) BOND C1 S8
+0.2058 (5.3%) BOND C1 C2
+0.3058 (7.9%) BOND C1 C7
-0.4698 (12.1%) BOND C3 C4
-0.4055 (10.4%) BOND C4 C5
+0.4995 (12.8%) BOND C6 C7

-0.2171 (5.6%) ANGLE C1 C2 O10
-0.2189 (5.6%) ANGLE C4 C5 H13

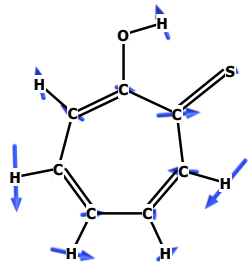

Mode 19: (A') 1011.98 cm-1
(IR: 42.0 km mol-1)
-0.4341 (10.7%) BOND C1 S8
+0.2445 (6.0%) BOND C2 O10
+0.2242 (5.5%) BOND C1 C2
+0.4624 (11.4%) BOND C2 C3
+0.3761 (9.3%) BOND C3 C4
-0.4191 (10.3%) BOND C5 C6
-0.2893 (7.1%) BOND C6 C7

+0.2882 (7.1%) ANGLE C1 C7 C6
-0.2200 (5.4%) ANGLE C2 C3 C4

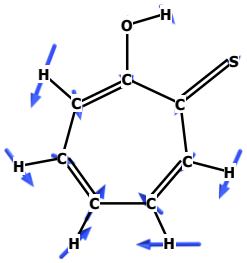

Mode 20: (A') 952.83 cm-1
(IR: 28.1 km mol-1)
+0.3410 (7.1%) BOND C1 S8
-0.4422 (9.2%) BOND C3 C4
-0.7757 (16.1%) BOND C4 C5
-0.8147 (16.9%) BOND C5 C6
-0.4828 (10.0%) BOND C6 C7

-0.2847 (5.9%) ANGLE C1 C2 C3

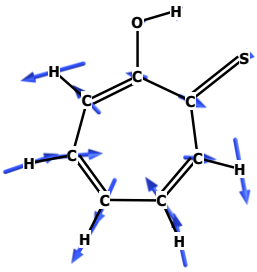

Mode 21: (A') 880.54 cm-1
(IR: 19.2 km mol-1)
+0.4724 (14.7%) BOND C1 C2
-0.1870 (5.8%) BOND C4 C5
-0.2308 (7.2%) BOND C5 C6

-0.3150 (9.8%) ANGLE C2 C3 C4
-0.6739 (21.0%) ANGLE C4 C5 C6
-0.2452 (7.6%) ANGLE C1 C7 C6

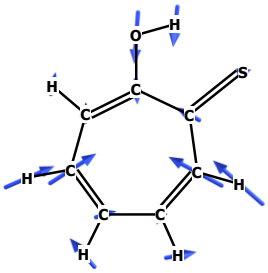

Mode 22: (A') 701.53 cm-1
(IR: 17.6 km mol-1)
-0.8648 (14.9%) BOND C2 O10
-0.3398 (5.9%) BOND C1 C7
-0.6997 (12.1%) BOND C1 C2
-0.7943 (13.7%) BOND C2 C3
-0.5817 (10.0%) BOND C3 C4

-0.6544 (11.3%) ANGLE C2 C3 C4
+0.3939 (6.8%) ANGLE C1 C7 C6
-0.2962 (5.1%) ANGLE C2 C1 C7

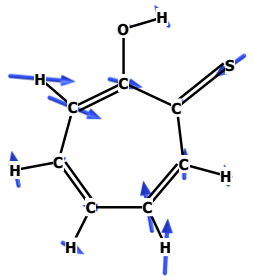

Mode 23: (A') 591.31 cm-1
(IR: 9.7 km mol-1)
-1.0188 (20.3%) BOND C1 S8
-0.8022 (16.0%) BOND C1 C2
-0.7051 (14.1%) BOND C1 C7
-0.4012 (8.0%) BOND C2 C3
-0.2650 (5.3%) BOND C4 C5
-0.2772 (5.5%) BOND C6 C7

+0.3510 (7.0%) ANGLE C2 C3 C4
+0.3184 (6.4%) ANGLE C5 C6 C7

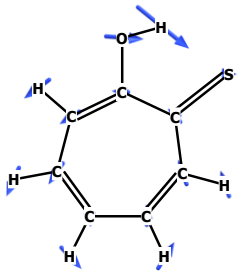

Mode 24: (A') 495.42 cm-1
(IR: 7.3 km mol-1)
-0.5734 (10.1%) BOND C1 C7
-0.4852 (8.5%) BOND C1 C2
+0.8129 (14.3%) BOND C2 C3
+0.4294 (7.5%) BOND C3 C4

-1.0448 (18.4%) ANGLE C1 C2 O10
+0.5755 (10.1%) ANGLE C3 C2 O10
+0.3362 (5.9%) ANGLE C1 C7 C6
+0.4391 (7.7%) ANGLE C5 C6 C7

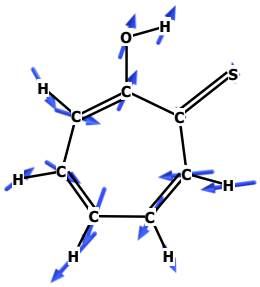

Mode 25: (A') 416.60 cm-1
(IR: 1.3 km mol-1)
+0.6807 (9.8%) BOND C1 C7
+0.5586 (8.1%) BOND C2 O10
+0.5529 (8.0%) BOND C3 C4
+0.5507 (8.0%) BOND C6 C7
-0.5394 (7.8%) BOND C1 C2
+0.7261 (10.5%) ANGLE C1 C7 C6
-0.5520 (8.0%) ANGLE C1 C2 C3
+0.3826 (5.5%) ANGLE C2 C3 C4
+0.4073 (5.9%) ANGLE C3 C4 C5
-0.4981 (7.2%) ANGLE C4 C5 C6
+0.3555 (5.1%) ANGLE C7 C1 S8

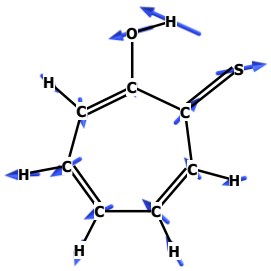

Mode 26: (A') 334.55 cm-1
(IR: 6.6 km mol-1)
+1.0125 (15.0%) BOND C1 S8
+0.6782 (10.1%) BOND C1 C2
+0.4254 (6.3%) BOND C2 C3

+0.8986 (13.3%) ANGLE C2 C1 S8
-0.8255 (12.2%) ANGLE C3 C2 O10
+0.7541 (11.2%) ANGLE C2 C3 C4
+0.6108 (9.1%) ANGLE C5 C6 C7
+0.4817 (7.1%) ANGLE C1 C7 C6

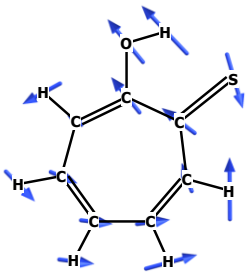

Mode 27: (A') 308.45 cm-1
(IR: 1.7 km mol-1)
+0.7606 (11.5%) BOND C1 C2
+0.4664 (7.1%) BOND C2 O10
-0.4131 (6.2%) BOND C1 S8
-0.3732 (5.6%) BOND C6 C7
-1.3480 (20.4%) ANGLE C7 C1 S8
+0.6011 (9.1%) ANGLE C1 C2 O10
+0.6507 (9.8%) ANGLE C1 C7 C6
-0.4597 (7.0%) ANGLE C1 C2 C3
+0.4592 (6.9%) ANGLE C2 C1 S8

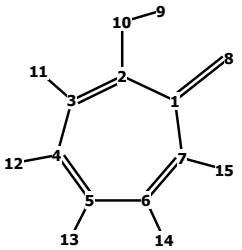

Structure of **s-OH** tautomer of **TT**
and atom numbering:
No. 1-7 - carbon, No. 8 - sulphur,
No. 10 - oxygen, No. 9, 11-15 - hydrogen

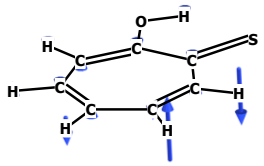

Mode 28: (A") 1006.69 cm-1
(IR: 0.5 km mol-1)
-0.6935 (24.7%) TORSION C7 C1 C2 C3
+0.1946 (6.9%) TORSION C2 C3 C4 C5
-0.7876 (28.0%) TORSION C3 C4 C5 C6
+0.1510 (5.4%) TORSION C4 C5 C6 C7
+0.4423 (15.7%) TORS. H14 C6 C7 H15

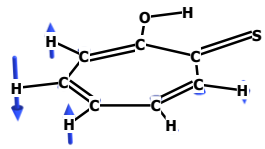

Mode 29: (A") 990.97 cm-1
(IR: 0.1 km mol-1)
-0.4905 (17.8%) TORSION C7 C1 C2 C3
+0.7651 (27.7%) TORSION C1 C2 C3 C4
-0.1688 (6.1%) TORSION C4 C5 C6 C7
+0.5301 (19.2%) TORSION C1 C7 C6 C5
-0.2203 (8.0%) TORSION C1 C2 C3 H11
-0.2705 (9.8%) TORS. H12 C4 C5 H13
-0.1585 (5.7%) TORS. H12 C4 C5 C6

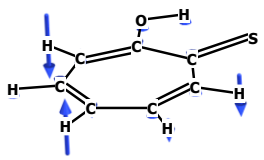

Mode 30: (A") 926.77 cm-1
(IR: 4.8 km mol-1)
+0.3333 (11.4%) TORSION S8 C1 C2 C3
-0.4534 (15.5%) TORSION C2 C1 C7 C6
-0.2543 (8.7%) TORSION C3 C4 C5 C6
+0.2530 (8.7%) TORSION C4 C5 C6 C7
-0.1754 (6.0%) TORSION C3 C4 C5 H13
+0.3539 (12.1%) TORSION C5 C6 C7 H15
-0.3626 (12.4%) TORS. H11 C3 C4 C5

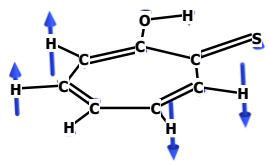

Mode 31: (A") 855.38 cm-1
(IR: 0.2 km mol-1)
-0.2216 (8.4%) TORSION C7 C1 C2 C3
-0.3103 (11.8%) TORSION C2 C3 C4 C5
+0.3104 (11.8%) TORSION C3 C4 C5 C6
+0.4049 (15.4%) TORSION C4 C5 C6 C7
-0.1806 (6.9%) TORSION C1 C7 C6 C5
-0.1357 (5.2%) TORSION S8 C1 C7 C6
-0.2252 (8.6%) TORSION C2 C3 C4 H12
-0.2905 (11.1%) TORSION C1 C7 C6 H14

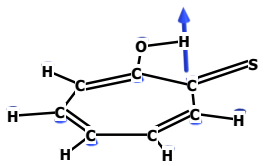

Mode 32: (A") 769.58 cm-1
(IR: 32.1 km mol-1)
+0.6077 (20.9%) OUT C1 C2 C3 O10
+0.4443 (15.3%) OUT C3 C4 C5 H12

-0.3475 (11.9%) TORSION C1 C2 O10 H9
-0.3196 (11.0%) TORSION C3 C2 O10 H9
-0.5706 (19.6%) TORSION C2 C3 C4 H12
-0.1952 (6.7%) TORSION C7 C1 C2 C3
+0.1763 (6.1%) TORSION C1 C2 C3 C4

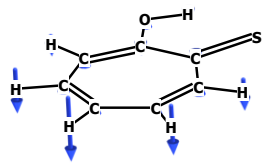

Mode 33: (A") 733.49 cm-1
(IR: 71.8 km mol-1)
+0.1998 (5.9%) OUT C3 C4 C5 H12
+0.6652 (19.7%) OUT C4 C5 C6 H13
+0.2265 (6.7%) OUT C5 C6 C7 H14

+0.2510 (7.4%) TORS. O10 C2 C3 C4
+0.1961 (5.8%) TORSION C1 C2 C3 C4
+0.5486 (16.3%) TORSION C2 C3 C4 C5
+0.3264 (9.7%) TORS. H13 C5 C6 C7
-0.2509 (7.4%) TORSION C2 C1 C7 C6

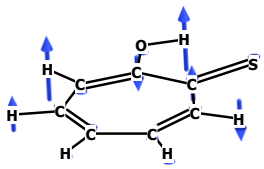

Mode 34: (A") 700.82 cm-1
(IR: 8.3 km mol-1)
+0.5889 (20.7%) TORSION C1 C7 C6 C5
-0.3423 (12.1%) TORSION C1 C2 C3 C4
+0.5403 (19.0%) TORSION C2 C3 C4 C5
-0.3714 (13.1%) TORSION C2 C1 C7 C6
-0.1933 (6.8%) TORSION C4 C5 C6 C7
+0.1484 (5.2%) TORSION S8 C1 C7 C6

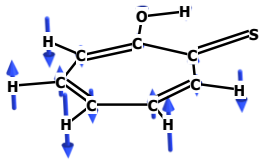

Mode 35: (A") 582.29 cm-1
(IR: 0.2 km mol-1)
+0.1959 (8.3%) TORSION C1 C2 C3 C4
-0.2887 (12.2%) TORSION C2 C3 C4 C5
+0.3941 (16.6%) TORSION C3 C4 C5 C6
-0.4107 (17.3%) TORSION C4 C5 C6 C7
+0.3483 (14.7%) TORSION C1 C7 C6 C5
-0.1479 (6.2%) TORSION S8 C1 C7 C6

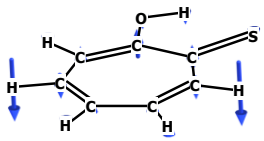

Mode 36: (A") 390.73 cm-1
(IR: 2.3 km mol-1)
+1.0057 (24.7%) OUT C3 C4 C5 H12
+0.2330 (5.7%) OUT C1 C2 C3 O10

-0.9045 (22.2%) TORSION C2 C3 C4 H12
-0.5689 (14.0%) TORSION C1 C2 C3 C4
+0.3674 (9.0%) TORSION C7 C1 C2 C3
+0.3152 (7.7%) TORS. H12 C4 C5 C6

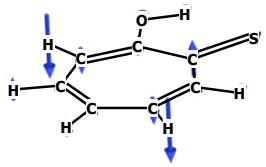

Mode 37: (A") 338.88 cm-1
(IR: 0.8 km mol-1)
+1.0919 (27.1%) OUT C5 C6 C7 H14

+1.0723 (26.6%) TORSION C1 C7 C6 H14
+0.3887 (9.7%) TORSION C2 C1 C7 C6
-0.2903 (7.2%) TORSION C7 C1 C2 C3
-0.2860 (7.1%) TORSION C4 C5 C6 H14
-0.2289 (5.7%) TORSION S8 C1 C2 C3

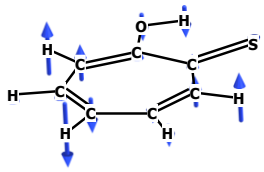

Mode 38: (A") 166.61 cm-1
(IR: 0.02 km mol-1)
+0.7064 (19.3%) OUT C1 C2 C3 O10
-0.4334 (11.8%) OUT C2 C1 C7 S8

-0.5801 (15.8%) TORSION C7 C1 C2 O10
+0.4644 (12.7%) TORSION S8 C1 C2 C3
+0.3661 (10.0%) TORSION C1 C7 C6 C5
-0.2045 (5.6%) TORSION C3 C4 C5 C6
-0.2795 (7.6%) TORS. O10 C2 C3 H11
-0.2033 (5.5%) TORS. H11 C3 C4 C5

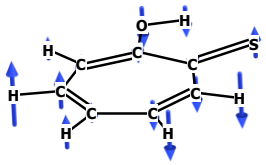

Mode 39: (A") 92.61 cm-1
(IR: 0.1 km mol-1)
+0.3965 (18.1%) OUT C2 C1 C7 S8

+0.5502 (25.2%) TORSION S8 C1 C2 O10
-0.3841 (17.6%) TORSION C4 C5 C6 C7
+0.1913 (8.8%) TORSION C2 C3 C4 C5
-0.1592 (7.3%) TORSION C3 C4 C5 C6

Table S5. Vibrational modes of the **a-SH** form of thiotropolone computed at the B3LYP/6-311+G(2d,p) level of theory in harmonic approximation, and vibrational assignment.

Mode	Weight distribution (%) of most prominent internal coordinates [a,b]	Total (%)	Total (%)	Approximate Description
	A' symmetry	**Bond**	**Angle**	
S_1	rC3H11 (14.8) + rC4H12 (14.4) + rC5H13 (**32.8**) + rC6H14 (19.2) + rC7H15 (6.6)	97.6	2.4	ν_a(CH)
S_2	rC3H11 (**42.9**) + rC4H12 (12.2) − rC5H13 (15.1) − rC6H14 (14.8) − rC7H15 (5.9)	96.4	3.6	ν_b(CH)
S_3	rC3H11 (8.1) − rC4H12 (10.1) − rC5H13 (**21.3**) + rC6H14 (**28.3**) + rC7H15 (**24.9**)	97.2	2.8	ν_c(CH)
S_4	rC3H11 (11.5) − rC4H12 (**29.5**) + rC6H14 (15.0) − rC7H15 (**28.3**)	100.0	0.0	ν_d(CH)
S_5	rC3H11 (9.0) − rC4H12 (**26.6**) + rC5H13 (15.1) − rC6H14 (**21.2**) + rC7H15 (**22.8**)	98.5	1.5	ν_e(CH)
S_6	rS8H9 (**78.0**) + βC2C1S8 (6.8)	88.3	11.7	ν(SH)
S_7	rC2C3 (6.5) – rC3C4 (**18.6**) + rC5C6 (**19.4**) – rC6C7 (7.1) – rC2O10 (14.7)	76.6	23.4	ν_a(CC)
S_8	− rC7C1 (7.0) − rC3C4 (10.4) + rC5C6 (7.1) + rC2O10 (**44.8**)	80.0	20.0	ν(C=O)
S_9	− rC7C1 (**20.3**) + rC3C4 (**16.1**) − rC4C5 (12.0) + rC5C6 (10.2) + rC6C7 (7.8)	76.2	23.8	ν_b(CC) − ν_c(CC)
S_{10}	+ rC7C1 (7.7) − rC2C3 (6.3) + rC3C4 (**15.1**) + rC5C6 (**17.2**) − rC6C7 (**13.9**) − − rC2O10 (5.8) + βC2C3H11 (5.5) − βC5C6H14 (7.4)	68.9	31.1	ν_c(CC) + ν_b(CC) − δ_a(CH)
S_{11}	− rC7C1 (**17.2**) + rC1C2 (5.8) − rC2C3 (6.4) + rC4C5 (**14.9**) − rC5C6 (8.6) − − rC2O10 (5.8) − βC1C2C3 (5.2) + βC3C4H12 (6.7) − βC5C6H14 (6.2)	64.4	35.6	δ_a(CH) − ν_d(CC)
S_{12}	− βC4C3H11 (**10.3**) + βC3C4H12 (9.8) − βC5C4H12 (7.4) + βC4C5H13 (6.1) – − βC6C5H13 (5.7) + βC5C6H14 (7.6) + rC2C3 (9.5) + rC3C4 (8.6) – rC2O10 (**11.8**)	44.0	56.0	δ_b(CH) (in-phase)
S_{13}	− rC7C1 (**18.3**) + rC1C2 (**15.4**) − rC2C3 (6.6) + rC2O10 (6.9) − − βC1C7H15 (**14.8**) − βC6C7H15 (6.8)	53.0	47.0	δ_c(CH) + ν_d(CC) (δsyn)
S_{14}	− rC7C1 (**10.5**) + rC2C3 (**14.5**) − rC3C4 (**10.1**) + βC2C3H11 (**13.4**) + + βC5C4H12 (7.1) + βC4C5H13 (5.4) + βC6C7H15 (6.9) + βC1C2O10 (6.8)	51.8	48.2	δ_d(CH) − ν_e(CC) (δanti)
S_{15}	rC7C1 (7.6) − rC2C3 (5.2) + rC3C4 (6.1) + rC4C5 (6.5) − rC5C6 (**18.1**) + + rC6C7 (6.5) + βC4C5H13 (7.8) − βC6C5H13 (5.7) + βC7C6H14 (9.2)	57.0	43.0	δ_e(CH) (δC5H − δC6H)
S_{16}	− rC1C2 (**10.6**) + rC2C3 (7.9) + rC3C4 (**13.8**) − rC4C5 (8.7) + rC6C7 (**11.1**) + + βC4C3H11 (5.9) − βC5C4H12 (8.7) − βC5C6H14 (6.2) + βC6C7H15 (5.9)	62.2	37.8	ν_e(CC) + δ_c(CH)
S_{17}	rC3C4 (**10.5**) + rC4C5 (**10.9**) − rC5C6 (7.7) − rC6C7 (**17.6**) + rC1S8 (5.2) + + βC1C2O10 (7.0) + βC4C5H13 (6.5)	59.4	40.6	ν_e(CC) + δ_d(CH)
S_{18}	rC2C3 (**11.0**) − rC4C5 (9.3) − rC5C6 (**11.1**) − rC1S8 (9.3) − βC1S8H9 (8.7) + + βC4C5C6 (6.4) − βC2C1C7 (6.1)	58.4	41.6	ν_f(CC) − δ(SH)
S_{19}	− rC7C1 (8.3) + rC2C3 (5.9) − rC4C5 (9.8) − rC5C6 (**14.1**) − rC6C7 (**13.9**) + + βC1S8H9 (**12.9**) + βC4C5C6 (5.9)	60.6	39.4	**δ(SH)** + ν_f(CC)
S_{20}	rC2C3 (5.1) + rC3C4 (9.1) + rC4C5 (**19.2**) + rC5C6 (**11.8**) + rC6C7 (9.5) − − rC1S8 (**11.2**) + βC1C7C6 (7.2)	73.1	26.9	ν_g(CC) − δ_a(ring)
S_{21}	βC1C2C3 (7.6) − βC3C4C5 (**10.4**) − βC4C5C6 (**16.6**) − βC1C7C6 (6.8) + + rC1C2 (**12.7**) − rC5C6 (6.2)	42.3	57.7	δ_b(ring)
S_{22}	− rC7C1 (6.6) − rC1C2 (**14.6**) − rC2C3 (**15.2**) − rC3C4 (9.6) − rC2O10 (**13.9**) + + βC1C7C6 (5.6) − βC2C3C4 (8.8)	73.1	26.9	ν_g(CC) + δ_b(ring)
S_{23}	− rC1S8 (**19.9**) − rC7C1 (12.8) − rC1C2 (13.2) − rC2C3 (9.2) − rC4C5 (6.6) + + βC2C3C4 (5.7) + βC5C6C7 (9.1) + βC1C2O10 (5.6)	74.5	25.5	ν(CS)
S_{24}	− βC1C2O10 (**16.7**) + βC3C2O10 (**9.4**) + βC5C6C7 (6.8) + βC1C7C6 (6.0) − − βC7C1S8 (5.8) − rC7C1 (10.5) − rC1C2 (10.0) + rC2C3 (15.4) + rC3C4 (7.8)	47.0	53.0	δ(CCO)
S_{25}	βC1C7C6 (**10.1**) − βC1C2C3 (9.6) + βC2C3C4 (6.1) + βC3C4C5 (6.6) − βC4C5C6 (6.8) + βC7C1S8 (6.0) + rC7C1 (8.9) − rC1C2 (7.8) + rC3C4 (7.9) + rC6C7 (8.0) + rC2O10 (7.9)	49.1	50.9	δ_c(ring)
S_{26}	rC1S8 (**18.5**) + rC2C3 (6.5) + rC6C7 (7.8) − rC2O10 (6.0) + − βC2C1C7 (**14.0**) + βC1C2C3 (8.7) + βC2C3C4 (10.3) + βC5C6C7 (6.1)	47.1	52.9	δ_d(ring)
S_{27}	− βC7C1S8 (5.2) + βC2C1S8 (**27.3**) + βC1C2O10 (16.7) − βC1C2C3 (5.5) + + rC1C2 (15.1) + rC1S8 (6.5)	37.3	62.7	δ(CCS)

	A'' symmetry	Tors.	Out	
S_{28}	τH11C3C4H12 (**13.8**) + τC1C2C3C4 (12.8) + τC1C7C6C5 (11.4) − − τC4C5C6C7 (**20.4**) − τC7C1C2C3 (**19.4**) − τS8C1C2C3 (6.4)	96.2	3.8	γ_a(CH)
S_{29}	τC6C7C1C2 (**29.5**) + τC2C3C4C5 (**24.3**) − τC7C1C2C3 (13.4) − − τC4C5C6H14 (6.2) − τH13C5C6H14 (11.1)	97.5	2.5	γ_b(CH)
S_{30}	− τC3C4C5C6 (**23.0**) + τH13C5C6C7 (10.0) − τC6C7C1C2 (**15.5**) + + τC5C6C7H15 (**13.2**) − τC7C1C2O10 (9.2) − τC7C1C2C3 (8.7) − − τH11C3C4C5 (6.6) + τC1C2C3C4 (5.7)	97.6	2.4	γ_c(CH)
S_{31}	− τC1C7C6C5 (**16.8**) − τC2C3C4C5 (13.3) + τC3C4C5C6 (8.6) − τO10C2C3C4 (8.6) − τC7C1C2C3 (**15.5**) − τC2C3C4H12 (8.4) − τS8C1C7H15(7.2) − γC2C3C4H11(6.3)	93.2	6.8	γ_d(CH)
S_{32}	τC6C7C1C2 (**15.9**) − τC2C3C4C5 (**20.5**) + τS8C1C2O10 (9.6) + + τC1C2C3C4 (9.0) − τS8C1C2C3 (9.0) − γC4C5C6H13 (6.9) − γC5C6C7H14 (10.1)	79.6	20.4	γ_e(CH) − τ_a(ring)
S_{33}	− γC3C4C5H12 (**23.5**) − τC1C2C3C4 (17.3) − τC1C2C3H11 (6.5) + + τC2C3C4H12 (**23.8**) − γC1C2C3O10 (5.5)	64.7	35.3	τ_a(ring) + γ_e(CH)
S_{34}	+ τC4C5C6C7 (**19.3**) − τC5C6C7C1 (**18.0**) + τC2C3C4C5 (10.7) − − τC3C4C5C6 (11.9) − τH12C4C5C6 (9.4) + τC2C1C7C6 (9.6)	99.1	0.9	τ_b(ring)
S_{35}	− τC7C1S8H9 (**21.0**) − γC2C1C7S8 (10.2) − τC7C1C2C3 (10.1) + τC1C2C3C4 (8.1) − τC7C1C2O10 (**18.5**) + τS8C1C7H15 (11.6) − τC2C1C7H15 (10.4)	88.7	11.3	τSH
S_{36}	+ γC5C6C7H14 (**27.7**) + τC1C7C6H14 (**23.6**) + τC6C7C1C2 (10.7) − − τC4C5C6H14 (10.5) − τS8C1C2C3 (8.8)	70.6	29.4	τ_c(ring)
S_{37}	+ τC7C1C2C3 (7.7) − τC1C2C3C4 (**14.0**) − τC2C3C4H12 (**14.4**) + + γC3C4C5H12 (**13.2**) + τC1C7C6H14 (5.7) − τS8C1C7C6 (5.5) − − γC1C7C6H15 (6.5) − γC2C1C7S8 (10.1) + τC7C1C2O10 (7.9)	64.8	35.2	τ_d(ring)
S_{38}	− γC2C1C7S8 (**19.5**) + γC1C2C3O10 (**15.8**) − τC7C1C2O10 (**15.8**) + + τS8C1C2C3 (**14.1**) + τS8C1C7H15 (6.1) − τC2C3C4C5 (5.6)	62.1	37.9	γ(CS) − γ(CO)
S_{39}	τS8C1C2O10 (**33.9**) + τC1C2C3C4 (10.3) + τC2C3C4C5 (5.2) − τC3C4C5C6 (17.1) − τC4C5C6C7 (6.3) + τC5C6C7C1 (6.9)	93.8	6.2	γ(CO) + γ(CS)

[a] See Scheme S2 for the atom numbering. Internal coordinates used in the analysis of vibrational modes are defomed automatically, as described in ref. S4.

[b] All contributions of most prominent internal coordinates, with weights of 5% or higher, are included. The top contributions are shown in bold. Abbreviations: ν = stretching, δ = in-plane bending, γ = out-of-plane bending, τ = torsion; $r_{i,j}$ is the distance between atoms A_i and A_j; $\beta_{i,j,k}$ is the angle between vectors A_kA_i and A_kA_j; $\tau_{i,j,k,l}$ is the dihedral angle between the plane defined by A_i, A_j, A_k and the plane defined by A_j, A_k and A_l atoms; $\gamma_{i,j,k,l}$ is the angle between the vector A_kA_i and the plane defined by atoms A_j, A_k, A_l. The symbols (+) and (−) denote in-phase and in-opposite-phase couplings between coordinates of different types.

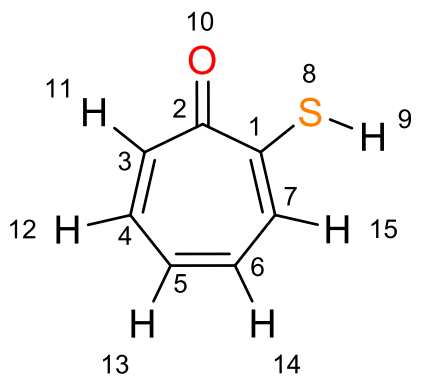

Scheme S2. Structure and the atom numbering of the **a-SH** form of thiotropolone.

Table S6. Experimental IR spectra of **a-SH** form of **TT** isolated in an Ar matrix at 15 K, and in neat solid **TT** crystals at 15 K, compared with harmonic and anharmonic wavenumbers ($\tilde{\nu}$ / cm^{-1}) and infrared intensities (I / km mol^{-1}) computed at the B3LYP/6-311+G(2d,p) level of theory, and vibrational assignment.

Mode	Ar matrix [a]		Crystal[a]	Calc.[b]				Sym.	Approximate
Nº.	$\tilde{\nu}_{exp}$	I_{exp}	$\tilde{\nu}_{exp}$	$\tilde{\nu}_{harm}$	I_{harm}	$\tilde{\nu}_{anhar}$	I_{anhar}		Description[c]
	A' symmetry								
$\nu_7+\nu_{10}$						3112.7	5.5	A'	
$\nu_9+\nu_{10}$						3041.9	6.4	A'	
ν_1	-	-		3014.8	11.1	3033.0	10.6	A'	ν_a(CH)
ν_2	-	-		3007.9	9.0	3052.4	10.2	A'	ν_b(CH)
ν_3	-	-		2997.6	8.2	3074.2	11.9	A'	ν_c(CH)
ν_4	-	-		2984.4	0.4	2997.9	4.8	A'	ν_d(CH)
ν_5	-	-		2981.2	10.1	2960.6	0.05	A'	ν_e(CH)
ν_6				2638.8	7.3	2530.6	7.7	A'	ν(SH)
$\nu_{28}+\nu_{34}$						1697.9	8.9	A'	
$\nu_{30}+\nu_{33}$			*1664*			1668.8	83.6	A'	
$\nu_{17}+\nu_{23}$			*1639*			1638.8	9.5	A'	
ν_7	1627.7	79.3	*1617*	1626.7	60.0	1620.2	55.2	A'	ν_a(C=C)
$2\times\nu_{32}$						1612.2	5.5	A'	
$\nu_{30}+\nu_{34}$						1607.4	6.8	A'	
$\nu_{14}+\nu_{26}$						1602.9	12.9	A'	
FR **(a)**	**1602.3**, 1600.5	**67.0**							FR[d] ν_8 with [$\nu_{30}+\nu_{33}$]
FR **(b)**	1593.6	**65.0**							FR[d] ν_8 with [$\nu_{21}+\nu_{22}$]
ν_8 (c)	1586.7	**134.1**	***1558***, *1552*	1587.8	**249.0**	1590.7	50.9	A'	ν(C=O)
$\nu_{17}+\nu_{24}$						1587.6	25.9	A'	
$\nu_{15}+\nu_{26}$						1585.8	9.8	A'	
$\nu_{21}+\nu_{22}$						1585.5	11.6	A'	
ν_9 **(d)**	1565.3 shoulder	**11.0**	*1581*	1586.1	**19.7**	1579.7	28.9	A'	ν_b(C=C)
	1540.1	5.1							
ν_{10}	**1490.2**, 1482.3	77.0	*1487 sh.*	1484.1	40.1	1478.7	21.7	A'	ν_c(C=C) − δ_a(CH)
ν_{11}	1470.5	37.9	*1467*	1473.9	67.6	1468.5	60.1	A'	δ_a(CH) − ν_d(CC)
ν_{12}	1413.1	1.6	1423	1416.3	3.0	1414.5	2.0	A'	δ_b(CH) (in-phase)
ν_{13}	1393.5	14.8	1409, 1390	1392.6	12.9	1388.4	10.9	A'	δ_c(CH) +ν_d(CC) (δsyn)
ν_{14}	1277.0	7.0	1290	1269.5	18.5	1274.4	13.5	A'	δ_d(CH) −ν_e(CC) (δanti)
ν_{15}	1255.8	1.0	1256	1255.3	1.3	1262.4	1.9	A'	δ_e(CH) (δC5H − δC6H)
$\nu_{22}+\nu_{24}$						1229.1	6.1	A'	
ν_{16}	1219.2	6.3	**1224**, 1218	1219.8	17.4	1213.4	7.4	A'	ν_e(CC) + δ_c(CH)
$\nu_{34}+\nu_{37}$			*1170*			1151.5	8.1	A'	
ν_{17}	1078.9	5.7	*1078*	1075.9	6.3	1079.3	0.9	A'	ν_e(CC) + δ_d(CH)
ν_{18}	1006.6	37.2	*1001*	1005.8	33.9	1004.7	29.7	A'	ν_f(CC) − δ(SH)
ν_{19}	**935.3**, 939.8	7.1	*927 broad*	940.4	7.5	940.4	4.2	A'	**δ(SH)** + ν_f(CC)
ν_{20}	**917.7**, 915.6	34.5	*915 ov.*	915.9	43.2	919.4	38.2	A'	ν_g(CC) − δ_a(ring)
ν_{21}	875.7	12.7	*872*	872.1	22.2	874.0	15.7	A'	**δ_b(ring)**
ν_{22}	717.6	6.2	*743*, ***730***	706.4	10.0	713.6	5.7	A'	**ν_g(CC)** + δ_a(ring)
ν_{23}	**563.5**, 561.8	26.3	*562*	556.3	20.2	558.2	18.0	A'	**ν(CS)**
ν_{24}	512.6	5.5	*510*	503.0	8.4	508.2	6.5	A'	δ(CCO)
ν_{25}	-	-		407.4	4.5	412.7	3.1	A'	δ_c(ring)
ν_{26}	-	-		320.2	0.8	323.8	0.9	A'	δ_d(ring)
ν_{27}	-	-		237.0	5.2	238.7	4.7	A'	δ(CCS)

	A'' symmetry								
ν_{28}	-	-		1008.0	0.2	1016.1	0.3	A"	γ_a(CH)
ν_{29}	-	-		983.1	0.03	1003.0	0.1	A"	γ_b(CH)
ν_{30}	**923.3**, 925.4 sh	14.7	*915 ov.*	920.4	6.5	928.2	4.4	A"	γ_c(CH) (mainly H15)
ν_{31}	**848.0**, 849.3	5.6	*857*	848.3	4.5	919.7	12.6	A"	γ_d(CH)
ν_{32}	770.2	37.8	*776*	765.9	43.5	820.6	3.7	A"	γ_e(CH) − τ_a(ring)
ν_{33}	673.0	19.2	*680*	671.8	18.8	696.5	44.4	A"	τ_a(ring) + γ_e(CH)
ν_{34}	-	-		568.0	0.0003	676.7	0.3	A"	τ_b(ring)
ν_{35}	-	-		405.7	7.2	403.0	4.5	A"	τSH
ν_{36}	-	-		347.6	3.2	358.6	6.5	A"	τ_c(ring)
ν_{37}	-	-		325.2	0.6	438.6	0.1	A"	τ_d(ring)
ν_{38}	-	-		154.4	0.2	163.8	0.1	A"	γ(CS) − γ(CO)
ν_{39}	-	-		66.3	4.5	77.3	3.8	A"	γ(CO) + γ(CS)

[a] Experimental intensities (*I*) were normalized in such a way that the sum of integrated experimental intensities in the 1630-480 cm^{-1} frequency range would be equal to the sum of the corresponding harmonic infrared intensities (A^{th}, in km mol^{-1}) of the two arrays [$\Sigma(\nu_7:\nu_{24})$ + $\Sigma(\nu_{30}:\nu_{33})$] computed at the B3LYP/6-311+G(2d,p) level of theory. For the split bands observed experimentally, the wavenumbers corresponding to the more intense component are shown in bold. For the polycrystalline sample (for brevity designated as "crystal"), the wavenumbers shown *in italic* correspond to the bands of the **a-SH** form of **TT**, that do not spectrally overlap with the bands of the **s-OH** form.

[b] Computed harmonic wavenumbers were multiplied by 0.950 (above 2800 cm^{-1}) or 0.980 (below 2000 cm^{-1}) and are expressed in cm^{-1}. Computed anharmonic wavenumbers and intensities are not scaled. The anharmonic section includes all fundamental modes, as well as the overtones and combination bands with computed anharmonic infrared intensities over 5 km mol^{-1}.

[c] Approximate descriptions are based on visualization of normal vibrations (using the Chemcraft software[S5]), and also on the Vibrational Mode Automatic Relevance Determination (VMARD) analysis using Bayesian regression, as defined by Teixeira and Cordeiro.[S4] The most prominent internal coordinates, obtained using the VMARD formalism, with weights above 5%, are listed in Table S5.

[d] FR stands for Fermi-resonance. The suggested FR combinations (tentative) are based on the experimentally observed wavenumbers of the respective fundamental modes (for **TT** in Ar matrix). The sum of intensities of the experimental multiplet band in the **1650-1550 cm^{-1}** frequency range (**TT** in Ar matrix), where ν(C=O) and ν(C=C) bands appear [marked as **(a)-(d)**], corresponds to the sum of theoretical intensities due to ν_8 and ν_9.

Table S7. The molecular vibrations of **a-SH** computed at the B3LYP/6-311+G(2d,p) level in harmonic approximation subjected to the VMARD (Vibrational Mode Automatic Relevance Determination) analysis using Bayesian regression

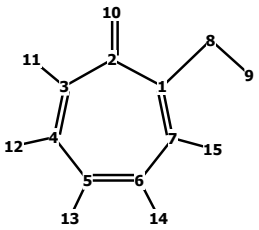	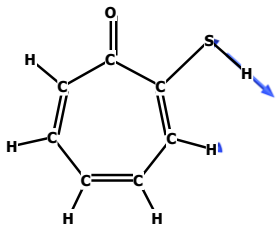
Structure of **a-SH** tautomer of **TT** and atom numbering: No. 1-7 - carbon, No. 8 - sulphur, No. 10 - oxygen, No. 9, 11-15 - hydrogen	Mode 6: (A') 2530.6 cm-1 (anharmonic) (IR: 7.3 km mol-1) **+0.9640 (78.0%) BOND S8 H9** -0.0845 (6.8%) ANGLE C2 C1 S8
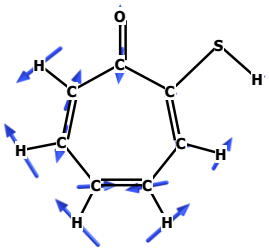	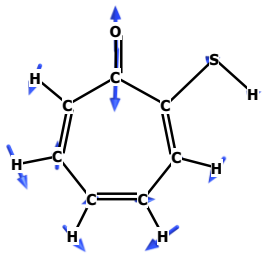
Mode 7: (A') 1625.05 cm-1 (IR: 60.0 km mol-1) +0.3304 (14.7%) BOND C2 O10 -0.1459 (6.5%) BOND C2 C3 **+0.4179 (18.6%) BOND C3 C4** **-0.4355 (19.4%) BOND C5 C6** +0.1591 (7.1%) BOND C6 C7	Mode 8: (A') 1586.21 cm-1 (IR: 249.0 km mol-1) **+0.8783 (44.8%) BOND C2 O10** -0.1364 (7.0%) BOND C1 C7 -0.2045 (10.4%) BOND C3 C4 +0.1385 (7.1%) BOND C5 C6
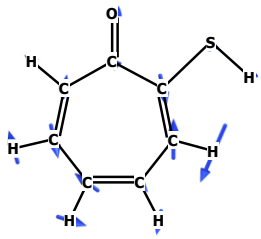	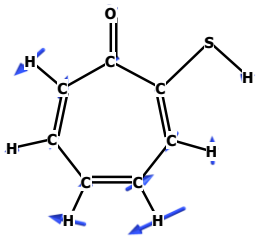
Mode 9: (A') 1584.47 cm-1 (IR: 19.7 km mol-1) **-0.4637 (20.3%) BOND C1 C7** **+0.3673 (16.1%) BOND C3 C4** **-0.2742 (12.0%) BOND C4 C5** +0.2325 (10.2%) BOND C5 C6 +0.1793 (7.8%) BOND C6 C7	Mode 10: (A') 1482.61 cm-1 (IR: 40.1 km mol-1) -0.1397 (5.8%) BOND C2 O10 +0.1850 (7.7%) BOND C1 C7 -0.1519 (6.3%) BOND C2 C3 **+0.3629 (15.1%) BOND C3 C4** **+0.4136 (17.2%) BOND C5 C6** **-0.3345 (13.9%) BOND C6 C7** +0.1322 (5.5%) ANGLE C2 C3 H11 -0.1786 (7.4%) ANGLE C5 C6 H14

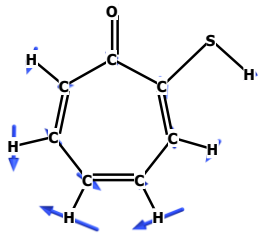

Mode 11: (A') 1472.44 cm-1
(IR: 67.6 km mol-1)
-0.1450 (5.8%) BOND C2 O10
-0.4283 (17.2%) BOND C1 C7
+0.1453 (5.8%) BOND C1 C2
-0.1589 (6.4%) BOND C2 C3
+0.3707 (14.9%) BOND C4 C5
-0.2131 (8.6%) BOND C5 C6

-0.1286 (5.2%) ANGLE C1 C2 C3
+0.1674 (6.7%) ANGLE C3 C4 H12
-0.1534 (6.2%) ANGLE C5 C6 H14

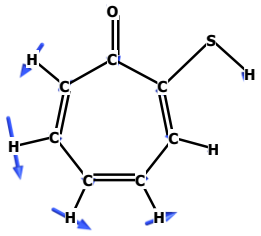

Mode 12: (A') 1414.89 cm-1
(IR: 3.0 km mol-1)
-0.3483 (11.8%) BOND C2 O10
-0.2814 (9.5%) BOND C2 C3
+0.2527 (8.6%) BOND C3 C4

-0.3039 (10.3%) ANGLE C4 C3 H11
+0.2898 (9.8%) ANGLE C3 C4 H12
-0.2194 (7.4%) ANGLE C5 C4 H12
+0.1786 (6.1%) ANGLE C4 C5 H13
-0.1667 (5.7%) ANGLE C6 C5 H13
+0.2239 (7.6%) ANGLE C5 C6 H14

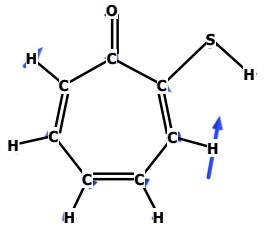

Mode 13: (A') 1391.13 cm-1
(IR: 12.9 km mol-1)
-0.4675 (18.3%) BOND C1 C7
+0.3936 (15.4%) BOND C1 C2
-0.1688 (6.6%) BOND C2 C3
+0.1758 (6.9%) BOND C2 O10

-0.3784 (14.8%) ANGLE C1 C7 H15
+0.1723 (6.8%) ANGLE C6 C7 H15

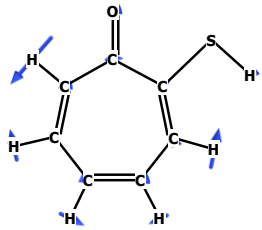

Mode 14: (A') 1268.24 cm-1
(IR: 18.5 km mol-1)
-0.4053 (10.5%) BOND C1 C7
+0.5618 (14.5%) BOND C2 C3
-0.3908 (10.1%) BOND C3 C4

+0.2623 (6.8%) ANGLE C1 C2 O10
+0.5192 (13.4%) ANGLE C2 C3 H11
+0.2757 (7.1%) ANGLE C5 C4 H12
+0.2108 (5.4%) ANGLE C4 C5 H13
+0.2656 (6.9%) ANGLE C6 C7 H15

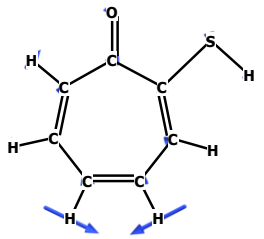

Mode 15: (A') 1254.06 cm-1
(IR: 1.3 km mol-1)
+0.3702 (7.6%) BOND C1 C7
-0.2528 (5.2%) BOND C2 C3
+0.2935 (6.1%) BOND C3 C4
+0.3127 (6.5%) BOND C4 C5
-0.8768 (18.1%) BOND C5 C6
+0.3142 (6.5%) BOND C6 C7

+0.3791 (7.8%) ANGLE C4 C5 H13
-0.2782 (5.7%) ANGLE C6 C5 H13
+0.4459 (9.2%) ANGLE C7 C6 H14

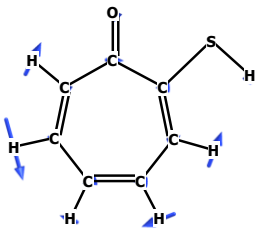

Mode 16: (A') 1218.59 cm-1
(IR: 17.4 km mol-1)
-0.4451 (10.6%) BOND C1 C2
+0.3340 (7.9%) BOND C2 C3
+0.5786 (13.8%) BOND C3 C4
-0.3666 (8.7%) BOND C4 C5
+0.4669 (11.1%) BOND C6 C7

+0.2490 (5.9%) ANGLE C4 C3 H11
-0.3674 (8.7%) ANGLE C5 C4 H12
+0.2487 (5.9%) ANGLE C6 C7 H15
-0.2623 (6.2%) ANGLE C5 C6 H14

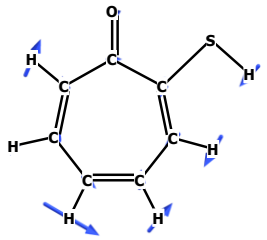

Mode 17: (A') 1074.81 cm-1
(IR: 6.3 km mol-1)
+0.2202 (5.2%) BOND C1 S8
+0.4414 (10.5%) BOND C3 C4
+0.4577 (10.9%) BOND C4 C5
-0.3221 (7.7%) BOND C5 C6
-0.7404 (17.6%) BOND C6 C7

+0.2949 (7.0%) ANGLE C1 C2 O10
+0.2718 (6.5%) ANGLE C4 C5 H13

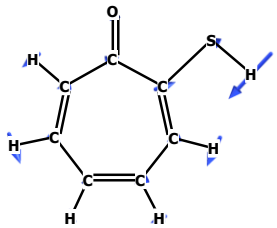

Mode 18: (A') 1004.73 cm-1
(IR: 33.9 km mol-1)
-0.3895 (9.3%) BOND C1 S8
+0.4614 (11.0%) BOND C2 C3
-0.3889 (9.3%) BOND C4 C5
-0.4635 (11.1%) BOND C5 C6

-0.3635 (8.7%) ANGLE C1 S8 H9
+0.2679 (6.4%) ANGLE C4 C5 C6
-0.2539 (6.1%) ANGLE C2 C1 C7

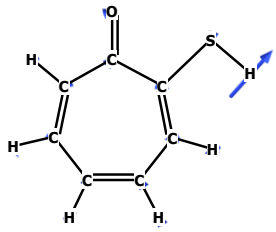

Mode 19: (A') 939.45 cm-1
(IR: 7.5 km mol-1)
-0.3685 (8.3%) BOND C1 C7
+0.2633 (5.9%) BOND C2 C3
-0.4357 (9.8%) BOND C4 C5
-0.6289 (14.1%) BOND C5 C6
-0.6216 (13.9%) BOND C6 C7

+0.5759 (12.9%) ANGLE C1 S8 H9
+0.2614 (5.9%) ANGLE C4 C5 C6

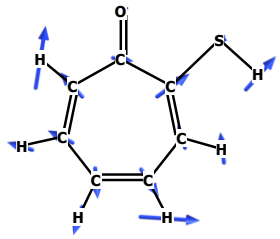

Mode 20: (A') 914.94 cm-1
(IR: 43.2 km mol-1)
-0.4400 (11.2%) BOND C1 S8
+0.2007 (5.1%) BOND C2 C3
+0.3602 (9.1%) BOND C3 C4
+0.7547 (19.2%) BOND C4 C5
+0.4634 (11.8%) BOND C5 C6
+0.3730 (9.5%) BOND C6 C7

+0.2818 (7.2%) ANGLE C1 C7 C6

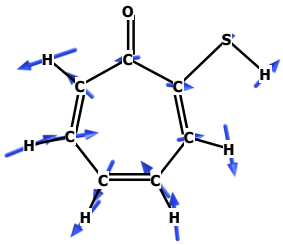

Mode 21: (A') 871.18 cm-1
(IR: 22.2 km mol-1)
+0.4170 (12.7%) BOND C1 C2
-0.2028 (6.2%) BOND C5 C6

+0.2494 (7.6%) ANGLE C1 C2 C3
+0.3419 (10.4%) ANGLE C3 C4 C5
-0.5449 (16.6%) ANGLE C4 C5 C6
-0.2247 (6.8%) ANGLE C1 C7 C6

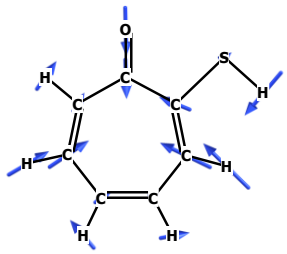

Mode 22: (A') 705.67 cm-1
(IR: 10.0 km mol-1)
-0.3695 (6.6%) BOND C1 C7
-0.8155 (14.6%) BOND C1 C2
-0.7792 (13.9%) BOND C2 O10
-0.8490 (15.2%) BOND C2 C3
-0.5359 (9.6%) BOND C3 C4

+0.3113 (5.6%) ANGLE C1 C7 C6
-0.4926 (8.8%) ANGLE C2 C3 C4

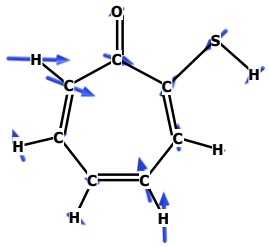

Mode 23: (A') 555.77 cm-1
(IR: 20.2 km mol-1)
-0.9653 (19.9%) BOND C1 S8
-0.6389 (13.2%) BOND C1 C2
-0.6205 (12.8%) BOND C1 C7
-0.4449 (9.2%) BOND C2 C3
-0.3227 (6.6%) BOND C4 C5

+0.2701 (5.6%) ANGLE C1 C2 O10
+0.2748 (5.7%) ANGLE C2 C3 C4
+0.4434 (9.1%) ANGLE C5 C6 C7

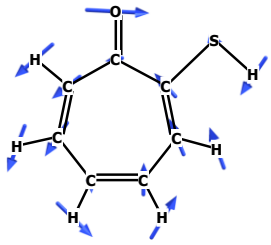

Mode 24: (A') 502.49 cm-1
(IR: 8.4 km mol-1)
-0.5899 (10.5%) BOND C1 C7
-0.5632 (10.0%) BOND C1 C2
+0.8682 (15.4%) BOND C2 C3
+0.4411 (7.8%) BOND C3 C4

-0.9430 (16.7%) ANGLE C1 C2 O10
+0.5305 (9.4%) ANGLE C3 C2 O10
+0.3397 (6.0%) ANGLE C1 C7 C6
+0.3807 (6.8%) ANGLE C5 C6 C7
-0.3247 (5.8%) ANGLE C7 C1 S8

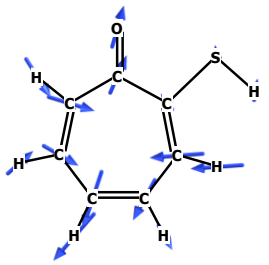

Mode 25: (A') 406.99 cm-1
(IR: 4.5 km mol-1)
+0.6188 (8.9%) BOND C1 C7
+0.5516 (8.0%) BOND C6 C7
+0.5494 (7.9%) BOND C3 C4
+0.5459 (7.9%) BOND C2 O10
-0.5418 (7.8%) BOND C1 C2

+0.7000 (10.1%) ANGLE C1 C7 C6
-0.6639 (9.6%) ANGLE C1 C2 C3
+0.4249 (6.1%) ANGLE C2 C3 C4
+0.4549 (6.6%) ANGLE C3 C4 C5
-0.4717 (6.8%) ANGLE C4 C5 C6
+0.4171 (6.0%) ANGLE C7 C1 S8

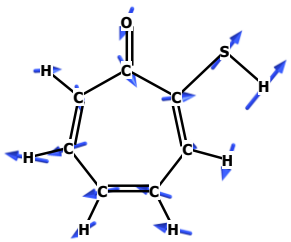

Mode 26: (A') 319.92 cm-1
(IR: 0.8 km mol-1)
+1.1240 (18.5%) BOND C1 S8
+0.3931 (6.5%) BOND C2 C3
-0.3652 (6.0%) BOND C2 O10
+0.4736 (7.8%) BOND C6 C7

-0.8529 (14.0%) ANGLE C7 C1 C2
+0.5259 (8.7%) ANGLE C1 C2 C3
+0.6281 (10.3%) ANGLE C2 C3 C4
+0.3696 (6.1%) ANGLE C5 C6 C7

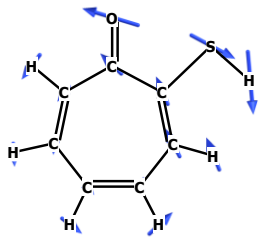

Mode 27: (A') 236.76 cm-1
(IR: 5.2 km mol-1)
+0.8537 (15.1%) BOND C1 C2
+0.3684 (6.5%) BOND C1 S8

+1.5462 (27.3%) ANGLE C2 C1 S8
+0.9452 (16.7%) ANGLE C1 C2 O10
-0.3100 (5.5%) ANGLE C1 C2 C3
-0.2938 (5.2%) ANGLE C7 C1 S8

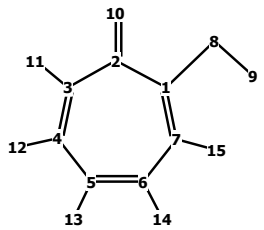

Structure of **a-SH** tautomer of **TT**
and atom numbering:
No. 1-7 - carbon, No. 8 - sulphur,
No. 10 - oxygen, No. 9, 11-15 - hydrogen

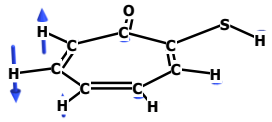

Mode 28: (A") 1006.98 cm-1
(IR: 0.2 km mol-1)
-0.5250 (19.4%) TORSION C7 C1 C2 C3
-0.1740 (6.4%) TORSION S8 C1 C2 C3
+0.3452 (12.8%) TORSION C1 C2 C3 C4
+0.3724 (13.8%) TORS. H11 C3 C4 H12
-0.5513 (20.4%) TORSION C4 C5 C6 C7
+0.3081 (11.4%) TORSION C1 C7 C6 C5

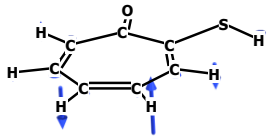

Mode 29: (A") 982.09 cm-1
(IR: 0.03 km mol-1)
+0.8048 (29.5%) TORSION C2 C1 C7 C6
-0.3647 (13.4%) TORSION C7 C1 C2 C3
+0.6614 (24.3%) TORSION C2 C3 C4 C5
-0.3037 (11.1%) TORS. H13 C5 C6 H14
-0.1683 (6.2%) TORSION C4 C5 C6 H14

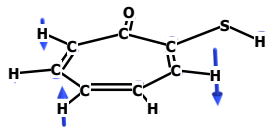

Mode 30: (A") 919.44 cm-1
(IR: 6.5 km mol-1)
-0.2781 (9.2%) TORSION C7 C1 C2 O10
-0.2625 (8.7%) TORSION C7 C1 C2 C3
+0.1715 (5.7%) TORSION C1 C2 C3 C4
-0.1987 (6.6%) TORS. H11 C3 C4 C5
-0.6928 (23.0%) TORSION C3 C4 C5 C6
+0.3015 (10.0%) TORS. H13 C5 C6 C7
+0.3978 (13.2%) TORSION C5 C6 C7 H15
-0.4673 (15.5%) TORSION C2 C1 C7 C6

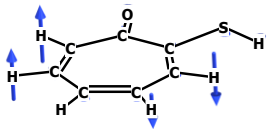

Mode 31: (A") 847.39 cm-1
(IR: 4.5 km mol-1)
-0.4633 (16.8%) TORSION C1 C7 C6 C5
-0.4281 (15.5%) TORSION C7 C1 C2 C3
-0.2387 (8.6%) TORS. O10 C2 C3 C4
-0.3677 (13.3%) TORSION C2 C3 C4 C5
-0.2329 (8.4%) TORSION C2 C3 C4 H12
+0.2376 (8.6%) TORSION C3 C4 C5 C6
-0.2000 (7.2%) TORSION S8 C1 C7 H15

-0.1753 (6.3%) OUT C2 C3 C4 H11

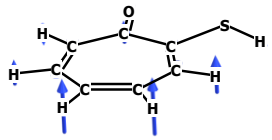

Mode 32: (A") 765.07 cm-1
(IR: 43.5 km mol-1)
-0.1730 (6.9%) OUT C4 C5 C6 H13
-0.2520 (10.1%) OUT C5 C6 C7 H14

+0.2406 (9.6%) TORSION S8 C1 C2 O10
-0.2237 (9.0%) TORSION S8 C1 C2 C3
+0.2256 (9.0%) TORSION C1 C2 C3 C4
-0.5116 (20.5%) TORSION C2 C3 C4 C5
+0.3978 (15.9%) TORSION C2 C1 C7 C6

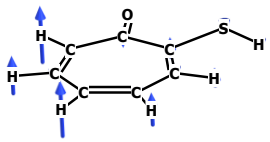

Mode 33: (A") 671.11 cm-1
(IR: 18.8 km mol-1)
-0.1896 (5.5%) OUT C1 C2 C3 O10
-0.8097 (23.5%) OUT C3 C4 C5 H12

-0.5949 (17.3%) TORSION C1 C2 C3 C4
-0.2232 (6.5%) TORSION C1 C2 C3 H11
+0.8194 (23.8%) TORSION C2 C3 C4 H12

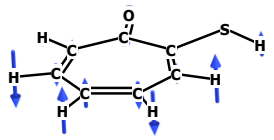

Mode 34: (A") 567.40 cm-1
(IR: 0.0003 km mol-1)
+0.2482 (10.7%) TORSION C2 C3 C4 C5
-0.2775 (11.9%) TORSION C3 C4 C5 C6
-0.2191 (9.4%) TORS. H12 C4 C5 C6
+0.4485 (19.3%) TORSION C4 C5 C6 C7
-0.4174 (18.0%) TORSION C1 C7 C6 C5
+0.2221 (9.6%) TORSION C2 C1 C7 C6

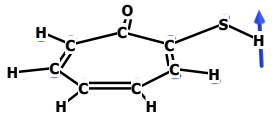

Mode 35: (A") 405.31 cm-1
(IR: 7.2 km mol-1)
-0.7133 (21.0%) TORSION C7 C1 S8 H9
-0.6291 (18.5%) TORSION C7 C1 C2 O10
+0.3940 (11.6%) TORSION S8 C1 C7 H15
-0.3522 (10.4%) TORSION C2 C1 C7 H15
-0.3439 (10.1%) TORSION C7 C1 C2 C3
+0.2741 (8.1%) TORSION C1 C2 C3 C4

-0.3455 (10.2%) OUT C2 C1 C7 S8

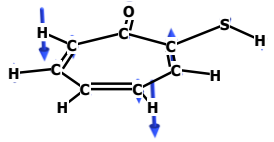

Mode 36: (A") 347.23 cm-1
(IR: 3.2 km mol-1)
+1.0958 (27.7%) OUT C5 C6 C7 H14

-0.3463 (8.8%) TORSION S8 C1 C2 C3
+0.4239 (10.7%) TORSION C2 C1 C7 C6
+0.9345 (23.6%) TORSION C1 C7 C6 H14
-0.4168 (10.5%) TORSION C4 C5 C6 H14

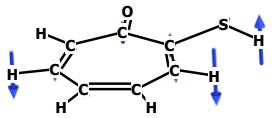

Mode 37: (A") 324.90 cm-1
(IR: 0.6 km mol-1)
-0.3678 (10.1%) OUT C2 C1 C7 S8
+0.4813 (13.2%) OUT C3 C4 C5 H12
-0.2356 (6.5%) OUT C1 C7 C6 H15

+0.2895 (7.9%) TORSION C7 C1 C2 O10
+0.2801 (7.7%) TORSION C7 C1 C2 C3
-0.5116 (14.0%) TORSION C1 C2 C3 C4
-0.5228 (14.4%) TORSION C2 C3 C4 H12
+0.2060 (5.7%) TORSION C1 C7 C6 H14
-0.1996 (5.5%) TORSION S8 C1 C7 C6

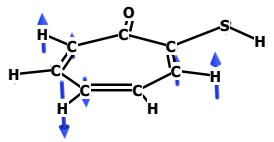

Mode 38: (A") 154.26 cm-1
(IR: 0.2 km mol-1)
-0.6653 (19.5%) OUT C2 C1 C7 S8
+0.5420 (15.8%) OUT C1 C2 C3 O10

-0.5399 (15.8%) TORSION C7 C1 C2 O10
+0.4826 (14.1%) TORSION S8 C1 C2 C3
-0.1917 (5.6%) TORSION C2 C3 C4 C5
+0.3336 (9.8%) TORSION C1 C7 C6 C5
+0.2081 (6.1%) TORSION S8 C1 C7 H15

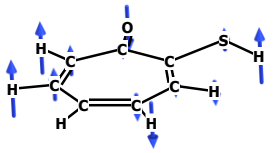

Mode 39: (A") 66.27 cm-1
(IR: 4.5 km mol-1)
+0.7893 (33.9%) TORSION S8 C1 C2 O10
+0.2389 (10.3%) TORSION C1 C2 C3 C4
+0.1218 (5.2%) TORSION C2 C3 C4 C5
-0.3969 (17.1%) TORSION C3 C4 C5 C6
-0.1476 (6.3%) TORSION C4 C5 C6 C7
+0.1607 (6.9%) TORSION C1 C7 C6 C5

Table S8. Electronic energies (E_{elec}, Hartree), zero-point energies (E_{ZPE}, Hartree), relative zero-point corrected energies (ΔE_0, kJ mol^{-1}) calculated at G4 level of theory for the most relevant isomers of thiotropolone and for the tautomerization (taut) and rotamerization (rot) transition states (TS) involving these isomers.

	s-OH	**a-OH**	**s-SH**	**a-SH**
E_{elec}	-743.535074	-743.515105	-743.528365	-743.524997
E_{ZPE}	0.111162	0.111158	0.10791	0.108231
ΔE_0	**0.0**	**52.4**	**9.1**	**18.8**

	TS-(taut)	**TS-OH(rot)**	**TS-SH(rot)**
E_{elec}	-743.521971	-743.508322	-743.514029
E_{ZPE}	0.106059	0.109745	0.106916
ΔE_0	**21.0**	**66.5**	**44.1**

Table S9. Optimized cartesian coordinates of the most relevant relevant isomers of thiotropolone calculated at G4 level of theory.

***s*-OH**			
	Coordinates (Angstroms)		
	x	y	z
C	-0.693361	-0.407379	-0.000086
C	-0.251035	0.989725	0.000005
C	1.043506	1.491263	0.000162
C	2.273707	0.827178	0.000275
C	2.530904	-0.527892	0.000261
C	1.583953	-1.562339	0.000125
C	0.205524	-1.504353	-0.000024
S	-2.367831	-0.660430	-0.000285
O	-1.212742	1.895886	-0.000070
H	-2.064106	1.367915	-0.000175
H	1.080567	2.576856	0.000200
H	3.143003	1.479633	0.000391
H	3.574132	-0.828298	0.000365
H	1.995803	-2.568728	0.000137
H	-0.301359	-2.464799	-0.000111

***a*-OH**			
	Coordinates (Angstroms)		
	x	y	z
C	-0.738122	-0.387091	-0.000003
C	-0.248209	0.995277	-0.000006
C	1.053709	1.453854	0.000051
C	2.288396	0.771828	0.000116
C	2.519540	-0.576333	0.000125
C	1.538335	-1.593158	0.000069
C	0.171190	-1.499533	0.000011
S	-2.383940	-0.686137	-0.000123
O	-1.240801	1.899823	-0.000070
H	-0.868890	2.790326	-0.000072
H	1.147179	2.540043	0.000048
H	3.162274	1.417614	0.000159
H	3.555126	-0.902121	0.000174
H	1.925603	-2.609224	0.000075
H	-0.360870	-2.446103	-0.000028

***s*-SH**			
	Coordinates (Angstroms)		
	x	y	z
C	-0.651375	-0.376444	-0.000001
C	-0.273292	1.066906	0.000003
C	1.111590	1.496465	0.000005
C	2.287870	0.805113	0.000004
C	2.522625	-0.590322	0.000000
C	1.580595	-1.583034	-0.000003
C	0.170899	-1.477635	-0.000004
S	-2.383007	-0.638775	-0.000003
O	-1.162985	1.925383	0.000004
H	-2.597706	0.707520	-0.000002
H	1.176571	2.581121	0.000008
H	3.184647	1.420842	0.000006
H	3.563567	-0.899202	0.000000
H	1.955159	-2.603379	-0.000006
H	-0.343725	-2.435848	-0.000007

***a*-SH**			
	Coordinates (Angstroms)		
	x	y	z
C	0.640746	-0.367799	-0.000033
C	0.257039	1.064783	-0.000005
C	-1.129605	1.500580	0.000062
C	-2.297795	0.800465	0.000111
C	-2.516893	-0.601953	0.000111
C	-1.572162	-1.589117	0.000061
C	-0.157896	-1.480592	-0.000004
S	2.401022	-0.459025	-0.000115
O	1.165691	1.896585	-0.000036
H	2.457320	-1.807913	-0.000111
H	-1.194843	2.585334	0.000074
H	-3.202836	1.403956	0.000157
H	-3.555584	-0.918814	0.000157
H	-1.942900	-2.610872	0.000071
H	0.356358	-2.438171	-0.000034

Table S10. Optimized cartesian coordinates calculated at G4 level of theory for the tautomerization (taut) and rotamerization (rot) transition states (TS) involving the most relevant isomers of thiotropolone (TT).

TS_{rot}-OH			
	Coordinates (Angstroms)		
	x	y	z
C	-0.728534	-0.389800	-0.032848
C	-0.251435	0.993671	-0.058499
C	1.035532	1.464882	0.013769
C	2.280681	0.792923	0.105085
C	2.519852	-0.549371	0.061367
C	1.552261	-1.579104	-0.071568
C	0.188880	-1.501267	-0.119401
S	-2.362733	-0.711982	0.103640
O	-1.229456	1.936013	-0.205246
H	-1.366620	2.425278	0.612210
H	1.097280	2.550297	-0.006632
H	3.146027	1.443657	0.195004
H	3.555496	-0.870835	0.121499
H	1.957543	-2.586512	-0.127588
H	-0.333764	-2.449878	-0.198206

TS_{rot}-SH			
	Coordinates (Angstroms)		
	x	y	z
C	0.665419	-0.303304	-0.011551
C	0.210854	1.115392	-0.017080
C	-1.221210	1.458753	0.029556
C	-2.348294	0.706790	0.036943
C	-2.493210	-0.713636	0.005287
C	-1.501995	-1.641944	-0.024481
C	-0.086056	-1.440367	-0.034864
S	2.459367	-0.517220	-0.049827
O	1.018890	2.032824	-0.050392
H	2.608083	-0.746147	1.269301
H	-1.342906	2.538468	0.060577
H	-3.284241	1.259873	0.071127
H	-3.515040	-1.082719	0.007828
H	-1.807578	-2.684378	-0.044892
H	0.487637	-2.362271	-0.066427

TS_{taut}-OH-SH			
	Coordinates (Angstroms)		
	x	y	Z
C	-0.643785	-0.434166	-0.000097
C	-0.289230	1.007964	0.000110
C	1.037801	1.519326	0.000261
C	2.250316	0.868708	0.000256
C	2.536713	-0.504237	0.000099
C	1.630212	-1.545126	-0.000092
C	0.229248	-1.510631	-0.000178
S	-2.358286	-0.633892	-0.000233
O	-1.260063	1.816785	0.000150
H	-2.269264	0.873307	-0.000035
H	1.061107	2.605176	0.000401
H	3.119459	1.522546	0.000396
H	3.588320	-0.773984	0.000133
H	2.057153	-2.545039	-0.000192
H	-0.251346	-2.485046	-0.000333

4. References

S1. Giuliano, B. M.; Reva, I.; Lapinski, L.; Fausto, R. Infrared Spectra and Ultraviolet-Tunable Laser Induced Photochemistry of Matrix-Isolated Phenol and Phenol-d_5. *Journal of Chemical Physics*, **2012**, *136*, 024505.

S2. Duarte, L.; Khriachtchev, L.; Fausto, R.; Reva, I. Photoisomerization of Azobenzenes Isolated in Cryogenic Matrices. *Phys. Chem. Chem. Phys.*, **2016,** *18***,** 16802-16811.

S3. Duarte, L.; Giuliano, B. M.; Reva, I.; Fausto, R. Tautomers and UV-Induced Photoisomerization of a Strongly Intramolecularly H-Bonded Aromatic Azo-Dye: 1-(Cyclopropyl)diazo-2-Naphthol. *J. Phys. Chem. A*, **2013**, *117*, 10671-10680.

S4. Teixeira, F.; Cordeiro, M. N. D. S. Improving vibrational mode interpretation using Bayesian regression. *J. Chem. Theory Comput.* **2019**, *15*, 456-470.

S5. Zhurko, G. A. Chemcraft – Graphical Program for Visualization of Quantum Chemistry Computations, Version 1.8; http://www.chemcraftprog.com, 2016.

S6. Michaut, X.; Vasserot, A.-M.; Abouaf-Marguin, L. Temperature and Time Effects on the Rovibrational Structure of Fundamentals of H_2O Trapped in Solid Argon: Hindered Rotation and RTC Satellite. *Vib. Spectrosc.* **2004**, *34*, 83-93.